Department of Mechanical Engineering
The University of Sheffield

3D CAFE modelling of transitional ductile – brittle fracture in steels

A thesis submitted for the degree of Doctor of Philosophy

by

Anton Shterenlikht

September 2003

"Ingenious modifications... cannot change the basic error of the Berg-Gurson approach..."

P F Thomason. *Ductile Fracture of Metals*, Pergamon Press, 1990

Contents

Acknowledgements

I would like to acknowledge my academic advisor Professor Ian C Howard for encouragement, support and mind-stimulating discussions.

I would also like to acknowledge Dr C Davis and Dr D Bhattacharjee, both from The University of Birmingham, Metallurgy and Materials for the permission to use their unpublished data (Dr D Bhattacharjee is now with Tata Iron & Steel Co., Jamshedpur, India).

I would also like to acknowledge Corus UK Ltd for the provision of broken Charpy samples and corresponding test data.

Summary

A coupled Cellular Automata – Finite Element (CAFE) three-dimensional multi-scale model was applied in this work to the simulation of transitional ductile-brittle fracture in steels. In this model material behaviour is separated from the representation of structural response and material data is stored in an appropriate number of cellular automata (CA). Two CA arrays, the "ductile" and the "brittle", are created, one is to represent material ductile properties, another is to account for the brittle fracture. The cell sizes in both arrays are independent of each other and of the finite element (FE) size. The latter is chosen only to represent accurately the macro strain gradients. The cell sizes in each CA array are linked to a microstructural feature relevant to each of the two fracture mechanisms. Such structure of the CAFE model results in a dramatic decrease of the number of finite elements required to simulated the damage zone. Accordingly the running times are cut down significantly compared with the conventional FE modelling of fracture for similar representation of microstructure. The Rousselier continuing damage model was applied to each cell in the ductile CA array. The critical value of the maximum principal stress was used to assess the failure of each cell in the brittle CA array. The model was implemented through a user material subroutine for the Abaqus finite element code. Several examples of model performance are given. Among them are the results of the modelling of the Charpy test at transitional temperatures. For a laboratory rolled TMCR steel the model was able to predict the transitional curve in terms of the Charpy energy and the percentage of brittle phase, including realistic levels of scatter, and the appearance of the Charpy fracture surface. The ways in which material data can be fitted into the model are discussed and particular attention is drawn upon the significance of the fracture stress distribution.

Nomenclature

In this work tensor analysis is used whenever possible. The tensor quantities are given as in Kachanov (1971).

Many symbols might have various sub- and superscripts. These are described in the text.

α – grain orientation angle

β – damage variable (Rousselier model)

Γ – cell solution-dependent variable

$\Delta_{\sqcup}$ – change in variable $\sqcup$ during one time increment

δ_{ij} – Kronecker delta

ϵ_{ij} – strain tensor

ϵ^e_{ij} – elastic strain tensor

ϵ^p_{ij} – plastic strain tensor, $\epsilon^p_{ij} = e^p_{ij} + \epsilon^p_m \delta_{ij}$

e^p_{ij} – plastic strain deviator

ϵ^p_m – mean plastic strain, $\epsilon^p_m = \frac{1}{3}\epsilon_{ii}$

ϵ^p_{eq} – equivalent plastic strain, $\epsilon^p_{eq} = \sqrt{\frac{2}{3} e^p_{ij} e^p_{ij}}$

η – the fraction of the brittle CA cells which have a grain boundary carbide

θ_{F} – misorientation threshold

Λ – cell property

ν – Poisson's ratio

Ξ – CA to FE transition function

σ_{ij} – stress tensor, $\sigma_{ij} = S_{ij} + \sigma_m \delta_{ij}$

σ_m – mean stress, $\sigma_m = \frac{1}{3}\sigma_{ii}$

σ_{eq} – equivalent stress, $\sigma_{eq} = \sqrt{\frac{3}{2} S_{ij} S_{ij}}$

σ_{I} – maximum principal stress

σ_{F} – fracture stress

σ_{Y} – yield stress

σ_{Y0} – first yield stress

Υ – cell state

Ω – cell transitional rule

A – total number of state variables per FE integration point

C_v – the total energy absorbed in the Charpy V-notch impact test

c – concentration factor for a CA array

d_g – grain size

d_k – direction cosines

E – Young's modulus

E_{ijkl} – isotropic elastic modulus tensor, $E_{ijkl} = 2G\delta_{ik}\delta_{jl} + \left(K - \frac{2}{3}G\right)\delta_{ij}\delta_{kl}$

f – a probability density function

f_0 – initial void volume fraction (Rousselier model)

G – shear modulus, $G = \frac{E}{2(1+\nu)}$

K – compression modulus, $K = \frac{E}{3(1-2\nu)}$

L – damage cell size

L_{FE} – finite element size

$\mathbb{M}$ – mapping finction

M – total number of cells per CA

$\mathbb{N}$ – the set of natural numbers

N – total number of cell properties

n – hardening exponent

Q – total number of cell state variables

R – total number of integration points per finite element

S_{ij} – stress deviator

t – time

T – temperature, in °C

W_β – shape parameter of Weibull dustribution

W_γ – location parameter of Weibull dustribution

W_η – scale parameter of Weibull dustribution

X^{max} – the maximum number of dead cells allowed per CA

Y – finite element solution-dependent variable

Chapter 1

The problem

There are two fundamental problems in modelling transitional ductile-brittle fracture with finite element analysis. Both problems have their roots in the complex inhomogeneous nature of materials such as steels and in the limitations of the finite element approach. The first problem is the high computational cost due to large numbers of small finite elements. Conflicting demands for the mesh size due to the different physical nature of ductile and brittle fracture is the second.

The local approach to fracture is a technique suitable for fracture propagation modelling because it takes into account only a small area ahead of the crack tip. Therefore this approach is geometry-independent as opposed to single- and two-parameter methods of fracture mechanics.

Exactly how small this area should be is determined by the need to correctly represent the stress and strain gradients ahead of the notch tip. The stress and strain fields there are the result of a complex interaction of different microstructural features. These can be grains, grain clusters, lath packets (in martensitic and bainitic steels), large and small inclusions, grain boundary carbides, larger precipitates, microcracks and microvoids etc. One common feature of all entries in the above list is their size – they are all small compared to any structure of engineering interest. Thus a finite element mesh of a structure with a crack must have a highly refined region extending long enough ahead of the crack tip to allow for modelling of the desired crack advance. In practice meshes

with tens of thousands of finite elements are not uncommon. The analysis of such meshes takes weeks or months and is very unstable due to ill-conditioned stiffness matrices.

At the same time the microstructural objects themselves can differ in size, e.g. a grain is typically tens of times larger than a grain boundary carbide and tens of times smaller than a lath packet. This has a profound influence on the ruling mesh size designed for the analysis of brittle or ductile fracture because the fracture progresses in microstructurally sensitive steps. In the case of ductile fracture these steps will usually be of the order of spacing between the microvoids or large inclusions. Grains, lath packet or a group of grains with small misorientation angles are the objects whose sizes are usually taken as a basis for the steps of brittle fracture advance. As the above step sizes might differ tens of times so do the mesh sizes required to simulate the propagation of brittle or ductile fracture. The only way these conflicting requirements can be satisfied within a single finite element mesh is by choosing a compromise mesh size. The accuracy of the solution is then a question.

The above two fundamental problems exist because in conventional finite element analysis a finite element is a material and a structural unit simultaneously. The structure and material are thus merged into an inseparable entity. This approach can be very ineffective.

The Cellular Automata – Finite Element (CAFE) approach used in this work offers solution to both problems mentioned above. In this approach material properties are moved away from the finite element mesh and distributed across the appropriate number of cellular automata arrays. Thus a finite element mesh is designed only to represent the macro strain gradients adequately. This is now a solely structural entity. A number of cellular automata arrays, in which cell sizes can be chosen independently, provide the means to analyse material properties at each size scale separately. So a CAFE model can accommodate as many size scales as necessary to address all material properties of interest. However only two cellular automata arrays are required to model the transitional ductile-brittle fracture.

The following chapter leads to the formulation of the CAFE model starting with a review of major models for ductile, brittle and ductile-brittle fracture proposed during the last half-century or so.

Chapter 2

Solutions

The fact that materials have a complex microstructure has long been recognised by materials engineers and scientists (Czochralski, 1924; Nadai, 1950; Cottrell, 1967; Gilman, 1969). In fact, had a material been homogeneous, it would be perfectly elastic until the final rupture by the separation of atoms (Knott, 1973; Thompson and Knott, 1993; Hertzberg, 1996). This case would be perfectly described by a single critical parameter, fracture toughness. It is the existence of grains, grain boundaries, inclusions or, on even lower level, dislocations, that demands the use of more complicated approaches to fracture analysis.

Extensive experimental studies of macro and micro fracture mechanisms resulted in understanding of two distinctive failure physical processes. The first is broadly called *ductile* and is characterised by relatively high energy needed for fracture to take place, high level of macro plasticity and dull appearance of the fracture surface. The fracture process that requires much less energy, produces bright, light-reflective fracture surfaces and accompanied by little or no plasticity is commonly called *brittle*. This is the second type of fracture.

Exactly how these two processes take place on a micro scale has been one of the main issues of experimental research in fracture mechanics for the last three decades. Simultaneously a number of material models describing the experimental findings have been developed.

2.1 Microanalysis of ductile fracture

A number of authors have observed regions of increased porosity next to the fracture surfaces in ductile metals (Tipper, 1949; Puttick, 1959; Rogers, 1960; Beachem, 1963; Gurland and Plateau, 1963; Bluhm and Morrissey, 1966; Liu and Gurland, 1968; Hayden and Floreen, 1969; Gladman et al., 1970, 1971; Gurland, 1972; Goods and Brown, 1979). Rhines (1961) was able to reproduce the observed porosity in plasticine using polystyrene spheres as inclusions.

Therefore it was proposed that ductile fracture in steels is "fracture by the growth of holes" (McClintock, 1968), "ductile fracture by internal necking of cavities" (Thomason, 1968), is caused by "the large growth and coalescence of microscopic voids" (Rice and Tracey, 1969) and is "via the nucleation and growth of voids" (Gurson, 1977*a*). Long before, Bridgman (1952) came to similar conclusions analysing the influence of hydrostatic pressure on the necking behaviour in tensile tests. He found that ductility is increasing with increased pressure up to a point where no cup-and-cone fracture can be observed and the diameter of the neck is approaching zero. Bridgman explained this by the closure of voids under very high pressure. Beachem (1975) reported eight (and predicted another possible six) types of dimple shapes tied to a fracture mode.

Ductile fracture by void growth and coalescence involves three stages: microvoid nucleation, void growth and void coalescence (Bates, 1984; Thomason, 1990; Gladman, 1997; Thomason, 1998).

Voids might nucleate at cleaved particles (Gladman et al., 1971; Cox and Low, 1974) or by decohesion of the interfaces of the second phase particles (Beachem, 1975; Argon et al., 1975; Argon and Im, 1975). Smaller particles require higher applied stresses for decohesion than larger ones. Based on this Bates (1984) showed that although carbides play secondary role in tensile test fracture, they might dominate the fracture process in fracture toughness test.

Void growth can be dilatational (volumetric) or by shape change. Stress triaxiality has a dramatic effect on void growth type and therefore on strain to fracture. In a tensile test voids grow in the direction of tensile stress prior necking. The onset of necking changes the uniaxial stress state to triaxial (Bridgman, 1952) which causes some volumetric growth (Gladman, 1997; Thomason, 1998) and therefore significantly lowers the strain to rupture.

Void coalescence is a process involving a localised internal necking of the intervoid material (Thomason, 1981) and was observed in different materials by Puttick (1959); Rhines (1961); Bluhm and Morrissey (1964) (very impressive photographs from these works were reprinted by McClintock (1968) and Thomason (1990, 1998)). The final stages of this process are associated with the failure of the submicron intervoid ligament by shearing along crystallographic planes or by microcleavage (Rogers, 1960; Cox and Low, 1974).

Development of theoretical models was slow due to the complex nature of ductile fracture phenomena. Three stages (nucleation, growth and coalescence of voids) have different nature and require separate physical models. As noted by McClintock (1968), contrary to the initial yielding or brittle fracture, where only the present stress state is needed for analysis, the size, shape and spacing of holes are a result of the whole history of straining. Some of the major models for ductile fracture are described below.

2.1.1 McClintock model

McClintock (1968) proposed a model for void growth and derived a criterion for ductile fracture. He assumed a material containing a regular three-dimensional array of cylindrical voids of elliptical section. The main axes of this array are parallel to the principal stress axes. The condition for fracture was that each void touches the neighbouring one. If the voids have the cylindrical axes parallel to the z direction and two semi axes are designated as a and b, and if the voids grow in the b direction then the approximate expression for the onset of fracture takes the form:

$$\frac{d\eta_{zb}}{d\epsilon_{eq}} = \frac{1}{lnF^f_{zb}} \left[\frac{\sqrt{3}}{2(1-n)} sinh \left(\frac{\sqrt{3}(1-n)}{2} \frac{\sigma_a + \sigma_b}{\sigma_{eq}} \right) + \frac{3}{4} \frac{\sigma_a - \sigma_b}{\sigma_{eq}} \right] \qquad (2.1)$$

where $\frac{d\eta_{zb}}{d\epsilon_{eq}}$ is a damage rate (ϵ_{eq} - equivalent strain, $d\eta_{zb}$ - damage increment), F^f_{zb} is a critical value of the relative growth factor, n is a hardening exponent, σ_a and σ_b are two of the principal stresses at infinity and σ_{eq} is the equivalent stress.

The over-simplified nature of this model leads to unrealistic results. Most important is that according to this model void growth is a smooth process until the final rupture, whereas, as argued by Thomason (1968, 1981, 1998) and

observed by Liu and Gurland (1968) and Hayden and Floreen (1969), the onset of failure by void coalescence is essentially due to a loss of stability.

Nevertheless even this simple model demonstrates some fundamental features of ductile fracture, e. g. very strong decrease of failure strain with increase of stress triaxiality and a "size effect", the need to know the stress history over a region of the order of the void spacing.

2.1.2 Rice-Tracey model

The approach undertaken by Rice and Tracey (1969) is based on variational analysis and the principle of maximum plastic work (Hill, 1983; Prager, 1959) or Drucker's stability postulate (Drucker, 1951, 1959; Khan and Huang, 1995). The authors analysed a case of dilatational growth of a single spherical void in a material under uniform stress state applied at infinity. They derived a classical equation for void enlargement under a high triaxiality stress state:

$$D = 0.283 \cdot exp\left(1.5\frac{\sigma_m}{\sigma_{eq}}\right) \tag{2.2}$$

where D is the ratio of the strain rate on the surface of a void to the strain rate at infinity, σ_m is the mean stress and σ_{eq} is the equivalent stress.

The simplicity of the resulting equation is the major advantage of this model. Probably it is for simplicity that it is by far the most famous void growth related equation.

The practical use of this equation however is quite limited because the model does not address void interaction, it cannot predict the fracture strain and cannot explain ductile failure in pure shear. Indeed according to the equation (2.2) if $\sigma_m = 0$ then the void acts merely as a stress concentrator with a constant concentration factor.

Finally as pointed out by Thomason (1990) and Gladman (1997) void extension can be found only at very high levels of negative hydrostatic pressure. Void shape distortion has a much bigger contribution in the process of void growth (Liu and Gurland, 1968; Hayden and Floreen, 1969).

Needleman (1972) applied similar variational analysis to a doubly periodic square array of circular cylindrical voids under plain strain conditions. He used FEA to minimise the resulting functional. This model is not particularly famous,

however, it inspired Gurson, section 2.1.4.

2.1.3 Argon-Im-Safoglu model

The authors analysed only the first stage of the process, i.e. void nucleation. They proposed that the criterion for separation of large particles is reaching locally of a critical interfacial tensile strength. For the case of spherical inclusions they derived the following equations for the radial stresses on the inclusion-matrix interface (Argon et al., 1975).

For non-interacting inclusions:

$$\sigma_{rr} = k_0 \left[\left(\frac{\gamma}{\gamma_y} \right)^{\frac{1}{n}} + \sqrt{3} \left(\frac{\sqrt{6}\,(n+1)}{m} \frac{\gamma}{\gamma_y} \right)^{\frac{1}{n+1}} \right] \tag{2.3}$$

For interacting inclusions:

$$\sigma_{rr} = k_0 \left[\sqrt{3} \left(\frac{\sqrt{3}}{\frac{\lambda}{\rho}} \frac{\gamma}{\gamma_y} \right)^{\frac{1}{n}} + \frac{\sqrt{6}}{m} \frac{\lambda}{\rho} + \left(\frac{\gamma}{\gamma_y} \right)^{\frac{1}{n}} \right] \tag{2.4}$$

where k_0 is the yield stress in shear, γ and γ_y are the present and yield shear strains, n is a hardening exponent, m is the Taylor factor, generally taken as 3.1, λ is the inter-particle spacing and ρ is the particle radius.

According to this approach decohesion occurs when

$$\sigma_{rr} \geq \sigma_c \tag{2.5}$$

In a companion paper (Argon and Im, 1975) the authors obtained σ_c experimentally for several materials and found values from $\sigma_c = 990$ MPa (Cu-0.6Cr alloy) to $\sigma_c = 1820$ MPa (martensitic steel).

2.1.4 Berg-Gurson-Tvergaard-Needleman model

Berg (1970) suggested that localisation occurs when the hardening behaviour of the matrix material is overweighed by softening due to the dilation of voids.

Inspired by the works of Berg (1970), McClintock (1968), Rice and Tracey (1969) and Needleman (1972), Gurson (1977*a*) proposed a methodology for obtaining an approximate yield surface for a material containing voids. He applied a maximum plastic work principle to kinematically admissible velocity

fields (Nadai, 1950; Drucker, 1959; Prager, 1959; Hill, 1983; Kachanov, 1971) for long circular cylindrical and spherical voids. For the latter case the yield function had the form:

$$\Phi = \left(\frac{\sigma_{eq}}{\sigma_y}\right)^2 + 2f \cdot \cosh\left(\frac{3\sigma_m}{2\sigma_y}\right) - 1 - f^2 = 0 \tag{2.6}$$

where f is a void volume fraction. This condition is reduced to the classical Mises yield criterion if $f = 0$.

The change in void volume fraction was described as:

$$\dot{f} = \dot{f}_g + \dot{f}_n \tag{2.7}$$

where $\dot{f}$ is the void volume fraction rate, $\dot{f}_g$ is the rate of growth of existing voids and $\dot{f}_n$ is the void nucleation rate. For the growth of existing voids Gurson (1977*b*) proposed only dilation:

$$\dot{f}_g = (1 - f)\dot{\epsilon}^p_{ij} I_{ij} \tag{2.8}$$

where $\dot{\epsilon}^p_{ij}$ is a plastic strain rate and I_{ij} is the second-order unit tensor.

Various nucleation models have been proposed by Gurson (1977*b*), e.g.:

$$\dot{f}_n = f_\epsilon(\epsilon^p_{eq})\dot{\epsilon}^p_{eq} \tag{2.9}$$

where f_ϵ - is the void nucleation intensity and ϵ^p_{eq} - is equivalent plastic strain.

Different aspects of void nucleation are discussed in Zhang et al. (2000); Tvergaard (1990). In materials containing large inclusions, e.g. MnS particles, voids would typically nucleate from these particles at the beginning of the plastic deformation. For modelling purposes it is reasonable to assume that all voids are nucleated at the beginning of the simulation and their amount is described by a single parameter – the initial void volume fraction, f_0, (Zhang et al., 2000). If, however, the material is such that voids are mostly nucleated from small particles, typically carbides, than a continuous nucleation mechanism is more appropriate (HKS, 2001).

When Yamamoto (1978) applied the yield function of equation (2.6) to the analysis of a shear band following a localisation theory of Rice (1977), he found that for a body without imperfection this yield condition predicts unrealistically large strain at localisation. He concluded that initial imperfections are necessary in order to achieve localisation at reasonable strain.

In an attempt to reduce the above discrepancy Tvergaard (1981, 1982*a*,*b*) introduced two adjustable parameters, q_1 and q_2 in Gurson's yield function (2.6):

$$\Phi = \left(\frac{\sigma_{eq}}{\sigma_y}\right)^2 + 2q_1 f \cdot \cosh\left(\frac{3q_2\sigma_m}{2\sigma_y}\right) - \left[1 + \left(q_1 f^2\right)\right] = 0 \qquad (2.10)$$

If $q_1 = q_2 = 1$ then (2.10) is reduced to (2.6). After comparison of modelling results with those obtained experimentally by Gladman et al. (1970) and Gladman et al. (1971), Tvergaard (1981, 1982*b*) concluded that $q_1 = 1.5$ and $q_2 = 1$ improve the performance of the yield condition (2.6) by approximately 50%.

Some authors went further and introduced the q_3 parameter (HKS, 2001):

$$\Phi = \left(\frac{\sigma_{eq}}{\sigma_y}\right)^2 + 2q_1 f \cdot \cosh\left(\frac{3q_2\sigma_m}{2\sigma_y}\right) - \left[1 + q_3\left(f^2\right)\right] = 0 \qquad (2.11)$$

Although some authors argued that q_1, q_2 and q_3 are true material constants (Tvergaard, 1982*b*, 1990; HKS, 2001), there is a growing experimental evidence that they depend on the triaxiality level (Pardoen and Hutchinson, 2000; Andrews et al., 2002).

The initial Gurson model can only simulate void nucleation and dilation. However it does not account for void coalescence in any way. Tvergaard and Needleman (1984) introduced the function $f^*(f)$ to model the rapid loss of stress-carrying capacity. This was an attempt to account for void coalescence. The function $f^*(f)$ was chosen as:

$$f^*(f) = \begin{cases} f & \text{for } f \le f_{\mathrm{c}} \\ f_{\mathrm{c}} - \dfrac{f_{\mathrm{u}}^* - f_{\mathrm{c}}}{f_{\mathrm{f}} - f_{\mathrm{c}}}\left(f - f_{\mathrm{c}}\right) & \text{for } f > f_{\mathrm{c}} \end{cases}$$

where f_{c} is a critical value of void volume fraction, the value at which a rapid loss of load-bearing capacity begins; f_{f} is void volume fraction at final fracture and $f_{\mathrm{u}}^* = 1/q_1$.

Based on experimental (Brown and Embury, 1973; Goods and Brown, 1979) and numerical (Andersson, 1977) results Tvergaard and Needleman (1984) have chosen the values $f_{\mathrm{c}} = 0.15$ and $f_{\mathrm{f}} = 0.25$.

This model, which is usually called 'Gurson-Tvergaard-Needleman' or simply GTN, is probably used most frequently in engineering applications. It is included in commercial finite element packages (HKS, 2001). However the nature of the model still makes it difficult to achieve a good correlation with

experiment. The main problem is that the model predicts strain to fracture that is much higher than that observed in experiments.

Thomason (1981, 1985*b*); Zhang et al. (2000) and others argued that the excessive high strain to fracture is a direct consequence of the model taking into account only the homogeneous deformation. In fact the voids were effectively substituted by a continuous porosity field. The only effect of voids in this model is through the pressure-dependent yield surface.

There are other attempts, apart from the modifications introduced by Tvergaard and Needleman, to extend the validity of the Gurson (1977*a*) model. A model dealing with prolate and oblate ellipsoidal cavities was proposed (Gologanu et al., 1993, 1994). Based on this model and ideas of Thomason (section 2.1.7) Pardoen and Hutchinson (2000) introduced an 'extended' model. Another combination of Gurson's and Thomason's approaches produced a 'complete' Gurson model (Zhang et al., 2000). These modified Gurson models produce more realistic results than the GTN model. However they are significantly more complex.

2.1.5 Lemaitre model

Based on concepts of a damage variable, D, and effective stress, $\tilde{\sigma} = \frac{\sigma}{1-D}$, (Kachanov, 1971; Rabotnov, 1969), Lemaitre (1985, 1996) proposed a thermodynamically consistent (Ziegler, 1977; Germain et al., 1983) theory of damage.

The model assumes a representative volume of material containing defects (microcracks or microvoids). If the intersection of this volume with a plane defined by a normal vector $\vec{n}$ is S and the area of intersection of voids and cracks of the volume by this plane is $S_D(\vec{n})$, then the damage variable is defined as $D(\vec{n}) = \frac{S_D(\vec{n})}{S}$. Since $0 \leq S_D(\vec{n}) \leq S$ then $0 \leq D(\vec{n}) \leq 1$. $D = 0$ means undamaged material whereas $D = 1$ means that material has no load-bearing capacity.

If D does not depend on $\vec{n}$ that the damage is considered isotropic and $D = \frac{S_D}{S}$. In this case the damage variable has the meaning of effective density of microdefects.

The major principle of Lemaitre's work is that "any strain constitutive equation for a damaged material may be derived in the same way as for a virgin ma-

terial except that the usual stress is replaced by the effective stress" (Lemaitre, 1996). Based on this principle he derived the constitutive equation for ductile damage. For the case of isotropic damage this condition has the form:

$$\dot{D} = \left[\frac{A^2}{2ES_0} \left(\frac{2}{3}(1+\nu) + 3(1-2\nu) \left(\frac{\sigma_m}{\sigma_{eq}} \right)^2 \right) \left(\epsilon_{eq}^p \right)^{\frac{2}{n}} \right]^{s_0} \dot{\epsilon}_{eq}^p \tag{2.12}$$

where A and n are material properties in the Ramberg-Osgood hardening law:

$$\epsilon^p = \left(\frac{\tilde{\sigma}}{A} \right)^n, \tag{2.13}$$

S_0 and s_0 are parameters in the damage evolution law:

$$\dot{D} = \left(\frac{-y}{S_0} \right)^{s_0+1} \dot{\epsilon}_{eq}^p, \tag{2.14}$$

which is based on the normality rule of potential of dissipation, φ:

$$\dot{D} = -\frac{\partial \varphi}{\partial y}. \tag{2.15}$$

In the last two equations $-y$ is called "the damage strain energy release rate" (Lemaitre, 1985).

The Lemaitre model is very powerful in the sense that it can be applied to any damage process, not just ductile damage. Its weak side, however, is that by the very nature of thermodynamically consistent theory it is a continuum theory. Therefore the Lemaitre ductile damage model is essentially a continuum softening one where the presence of voids or cracks is introduced via damage variable, D.

Other models based on Continuum Damage Mechanics (CDM) have been formulated over the years (McDowell, 1997).

2.1.6 Rousselier model

Another thermodynamically consistent ductile damage theory was introduced by Rousselier (1981). The plastic potential in this model has the form:

$$\frac{\sigma_{eq}}{\rho} - H\left(\epsilon_{eq}^p\right) + B\left(\beta\right) Dexp\left(\frac{\sigma_m}{\rho\sigma_1}\right) = 0 \tag{2.16}$$

where:

$$\dot{\beta} = \dot{\epsilon}_{eq}^p Dexp\left(\frac{\sigma_m}{\rho\sigma_1}\right) \tag{2.17}$$

$$\rho(\beta) = \frac{1}{1 - f_0 + f_0 exp\beta} \tag{2.18}$$

$$B(\beta) = \frac{\sigma_1 f_0 exp\beta}{1 - f_0 + f_0 exp\beta}, \tag{2.19}$$

β is a scalar damage variable. Its evolution is determined by equation 2.17. While material is within elasticity limits $\beta = 0$,

B is the damage function,

ρ is a dimensionless density. From equation 2.18 it follows that ρ decreases with increasing β,

D and σ_1 are material constants,

f_0 is the initial void volume fraction and

$H\left(\epsilon^p_{eq}\right)$ is a term describing the hardening properties of material. Usually this is equal to the yield stress of the undamaged material, $H\left(\epsilon^p_{eq}\right) = \sigma_{\mathrm{Y}}\left(\epsilon^p_{eq}\right)$.

The Rousselier model has the same strong and weak sides as the previous two, GTN and Lemaitre (Rousselier, 1987). All three are continuum damage models and can therefore be used as constitutive models for material with microcavities. The models can be used for numerical simulation of fracture propagation. Their weak side, however, is the inability to model shear fractures since only a volumetric void growth is allowed.

2.1.7 Thomason model

Thomason (1968, 1981, 1982, 1985*a*,*b*, 1993) studied the details of the coalescence phenomenon. He formulated a sufficient condition for the stability of incompressible plastic flow in the presence of microvoids for two- and three-dimensional cases. His models based on plasticity theory (Hill, 1983; Kachanov, 1971) and theorems of limit analysis (Prager, 1959) were summarised in a book (Thomason, 1990). He later criticised the models proposed by Gurson and Rousselier as being based on an "erroneous criterion of microvoid coalescence" (Thomason, 1998). Indeed Yamamoto (1978) has shown that Berg-Gurson model gives realistic critical strains only after significant changes in void volume fractions.

Thomason's analysis resulted in the concept of incipient void coalescence leading to an instantaneous change from incompressible to dilational plasticity (Thomason, 1981). The condition for the onset of coalescence in a plane strain

case has the following form:

$$(\sigma_{\mathrm{Ic}} - \sigma_{\mathrm{I}})\,\dot{\epsilon}_{\mathrm{Ic}} = 0 \tag{2.20}$$

where σ_{Ic} is the plastic limit-load stress, σ_{I} is the maximum principal stress and $\dot{\epsilon}_{\mathrm{Ic}}$ is the maximum principal strain rate across an intervoid matrix neck.

If only cylindrical voids are assumed then σ_{Ic} can be represented by the following empirical equation (Thomason, 1998):

$$\frac{\sigma_{\mathrm{Ic}}}{2k} = 1.43 \cdot f^{-1/6} - 0.91 \tag{2.21}$$

where k is the maximum shear stress, $k = \sigma_{\mathrm{I}} - \sigma_m$, and f is a void volume fraction.

The Thomason model for void coalescence is probably the most physically based and accurate to the present day. A strain to failure in a uniaxial test predicted with this model is in a good agreement with the experimental results (Thomason, 1982). However it can hardly be used for numerical modelling because of two fundamental problems.

The limit-load model is not a constitutive one. It can only predict the onset of void coalescence as a start of material and, what is more important, structural instability. Thus a structure is considered instantly failed when the condition of equation (2.20) is met.

The material rate of hardening in the intervoid matrix approaching ductile fracture is reduced to a very low level. Plastic solids with low work-hardening rate are described by second-order hyperbolic partial differential equations (Thomason, 1998). These equations cannot at present be solved with finite element methods (Johnson, 1987; Belytschko et al., 2000) but with what mathematicians call the method of characteristics (Smith, 1965; Johnson, 1987) and engineers – the slip-line technique (Hill, 1983).

A similar approach to void coalescence problem was explored by Szczepiński (1982) who argued that a theoretical analysis of a plane strain rigid-plastic material model with cylindrical holes is very complicated because there exists strong stress concentration at the edges of the holes even during purely elastic response. He proposed an idealised configuration where voids are initially introduced as slits. The theoretical analysis can be then performed based on slip-line technique.

2.1.8 Cavitation models

In most cases microvoids do not show significant growth before the onset of coalescence (Thomason, 1998). However if constraint is very high and if very few void nucleation cites are present then volumetric void growth can be very strong.

Ashby et al. (1989) observed the enlargement of a single void by a factor of more than 10^6 in tensile tests of highly constrained lead wires.

Huang et al. (1991) analysed a single spherical void in elastic-plastic materials under a remote stress field. They showed that a complex interaction of elasticity and plastic yielding can lead to a "cavitation instability", if the stresses in the material surrounding the void are sufficiently high so that the work produced by these stresses to expand the void is less than the energy released by such expansion.

It is easy to draw an analogy between the above analysis of the cavitation instability and the energy condition of Griffith (1924) for an unstable crack growth.

Faleskog and Shih (1997) conducted a two-dimensional plane strain finite element analysis of a square material cell containing a single cylindrical void in its centre. Their results were very similar to those reported by Huang et al. (1991), that the stored elastic energy can cause void expansion by several orders of magnitude over a negligible macroscopic strain increment.

2.2 Microanalysis of brittle fracture

Significant advance has been made in understanding of the brittle fracture phenomenon since Griffith's days (Griffith, 1921, 1924). At present there is a vast amount of literature on the subject. A number of review books and papers have been published (e.g. Averbach et al., 1959; Knott, 1973; Hahn, 1984; Thompson and Knott, 1993).

2.2.1 Crack initiation models

It is generally agreed that a dislocation pile-up at an obstacle, such as a grain – carbide interface, can cleave a grain boundary carbide and thus initiate a

microcrack (McMahon and Cohen, 1965; Lin et al., 1987; Thompson and Knott, 1993). Thus some degree of plastic deformation in a ferrite grain is always necessary to fracture a neighbouring carbide (Lin et al., 1987).

The stresses required to generate a microcrack can be written as follows:

$$\tau = 4.4 \cdot \frac{\gamma}{na}, \tag{2.22}$$

$$\sigma = K \cdot \frac{\gamma}{na}, \tag{2.23}$$

where τ and σ are shear and normal stresses accordingly, γ is an effective surface energy, n is the number of dislocations piled up against a grain boundary, a is the atomic spacing and K is a coefficient depending on the arrangement of the dislocation pile-up.

Equation (2.22) was obtained by Zener in 1948 (Hahn et al., 1959). The coefficient K in equation (2.23) can be $K = 2.7$ (Orowan model, 1954), $K = 5.3$ (Bullough model, 1956) or $K = 2$ (Cottrell, 1959). The first two values are taken from Hahn et al. (1959). The exact value of K depends on the assumed dislocation model. Zener analysed a crack forming on a plane normal to the operative slip plane. Orowan suggested that a polygonised array of dislocations can generate a crack in the slip plane. In the Bullough model the crack occurs in the slip plane. Cottrell assumed that two intersecting (110) slip planes in b.c.c. materials produce a microcrack on the common (100) plane (Hahn et al., 1959).

The shape of equations (2.22) and (2.23) suggests that the number of cracked carbides increases with applied strain. Indeed the number and intensity of dislocation pile-ups increases with plastic straining and hence the stresses required to generate a microcrack decrease. This point is supported by experimental observations (Gurland, 1972).

A microcrack in a cleaved carbide can advance if the following condition is met:

$$\sigma_n \geq \sigma_F \tag{2.24}$$

where σ_n is a normal stress acting across the grain-carbide interface and σ_F is a fracture or cleavage stress.

Smith (1966*a*,*b*) derived an equation for the fracture stress of a carbide – ferrite interface. Based on Smith's analysis Lin et al. (1987) obtained a similar

equation for the fracture stress of a ferrite – ferrite interface. Both equations are shown below.

$$\sigma_F^{cf} = \sqrt{\frac{\pi E \gamma_{cf}}{(1-\nu^2)\, d_c}}, \tag{2.25}$$

$$\sigma_F^{ff} = \sqrt{\frac{\pi E \gamma_{ff}}{(1-\nu^2)\, d_g}}, \tag{2.26}$$

where σ_F^{cf} and σ_F^{ff} are the fracture stresses of a carbide – ferrite and a ferrite – ferrite interfaces accordingly, γ_{cf} and γ_{ff} are the effective surface energies of a carbide – ferrite and a ferrite – ferrite interfaces accordingly, d_c and d_g are carbide and ferrite grain sizes accordingly, E is the elasticity modulus and ν is the Poisson's ratio.

Ritchie et al. (1973) postulated that the condition of equation (2.24) has to be satisfied over a distance of two grain sizes ahead of the crack tip for the fracture advance to take place. This is commonly called the "critical distance" idea (Thompson and Knott, 1993).

Later Curry and Knott (1978) proposed a statistical analysis of "eligible" particles that can be found within the critical distance. An eligible particle is a cracked particle with the crack length equal or greater than the critical one. Their conclusion was that a very small percentage of large particles have a disproportionate influence on the fracture resistance.

2.2.2 Weakest link models

Beremin (1983) developed the idea of eligible particles into a "weakest link" statistical model. According to this model a certain volume, V, of material ahead of the crack tip (usually the volume of the plastic zone) is assumed to have a distribution of microcracks of different lengths. Catastrophic failure is assumed to take place if a crack of critical length is found in this volume. This microcrack is a weakest link, hence the name of the model. The probability of failure is the probability of finding such microcrack.

It is further assumed that the volume V can be divided into smaller volumes V_0, which must be big enough so that the probability of finding a microcrack of critical length is not negligible. At the same time V_0 must not be too big so that one can assume that the stress state is homogeneous over V_0. Thus usually

V_0 is chosen to include several grains.

The failure probability takes the following form (Beremin, 1983; Lin et al., 1987; Ruggieri, 1998):

$$\Phi = 1 - \exp\left[-\int_0^V \frac{1}{V_0}\int_0^\sigma g(S)dS\right], \tag{2.27}$$

where $g(S)dS$ is the number of microcracks per V_0 with stresses required to propagate them between S and $S + dS$.

Usually a three-parameter Weibull probability distribution function (Weibull, 1951) is used to express $g(S)dS$:

$$\int_0^\sigma g(S)dS = \left(\frac{\sigma_{\mathrm{I}} - \sigma_{th}}{\sigma_u}\right)^m, \tag{2.28}$$

where σ_{I} is a maximum principal stress in V_0, m is a shape parameter, σ_u is a scale parameter and σ_{th} is an offset parameter, a threshold stress, required to propagate the largest feasible microcrack.

By substituting equation (2.28) into (2.27) one can obtain:

$$\Phi = 1 - \exp\left[-\left(\frac{\sigma_w}{\sigma_u}\right)^m\right], \tag{2.29}$$

where

$$\sigma_w = \left[\frac{1}{V_0}\int_0^V (\sigma_{\mathrm{I}} - \sigma_{th})\, dV\right]^{1/m} \tag{2.30}$$

is called "Weibull stress" (Beremin, 1983).

A progressive brittle fracture statistical model based on "chain-of-bundles" statistics (Gücer and Gurland, 1962) was proposed by Ruggieri et al. (1995). In this model several critical events are allowed before the catastrophic failure takes place. The analysis leads to Weibull statistics and effectively to the same relations as expressed by equations (2.29) and (2.30) (Ruggieri, 1998).

Other forms of equation (2.28) can be used. Kroon and Faleskog (2002) introduced the influence of applied strain on $g(S)dS$ and used an exponential distribution instead of Weibull:

$$\int_0^\sigma g(S)dS = c \cdot \epsilon_{eq}^p \cdot \left(\exp\left[-\left(\frac{\sigma_{\mathrm{m}}}{\sigma_{\mathrm{I}}}\right)^2\right] - \exp\left[-\left(\frac{\sigma_{\mathrm{m}}}{\sigma_{th}}\right)^2\right]\right), \tag{2.31}$$

where σ_{m} and c are material parameters; σ_{m} corresponds to the stress needed to propagate a mean size microcrack.

The authors claim that their model predicts the influence of constraint on the failure probability better than the model based on the three-parameter Weibull distribution.

However, as pointed out by Wallin (1991), "even though the models may differ considerably in their basic assumptions of the microscopic fracture mechanism, macroscopically most of them still yield an identical result".

2.2.3 Crack arrest

The problem of crack arrest received somewhat less attention than the issue of crack nucleation and growth. Perhaps this is due to fact that in many applications crack arrest does not happen, i.e. a brittle crack would not stop until the end of a specimen or a structure component is reached. This situation is described perfectly well by the critical event analysis.

Generally a running brittle crack can arrest if the applied stresses decrease with increasing crack length (e.g. if the test is performed under displacement control) or if a crack hits an area of fine grains. According to equation (2.26) the fracture stress of a ferrite – ferrite interface is inversely related to the grain size, so the fine grain region will represent a significant obstacle to an advancing crack. There is some experimental evidence in support of this idea (Malik et al., 1996; Jang et al., 2003).

There is also some experimental evidence that a high-angle misorientation boundary can act as a crack arrester or at least retard or inhibit the crack propagation (Zikry and Kao, 1996). Nohava et al. (2002) reported crack arrest in A508 Class 3 steels at grain boundaries with 55° – 60° misorientation angles.

2.3 Coupled ductile-brittle fracture modelling

The main two problems of coupled ductile-brittle fracture modelling were discussed briefly in Chapter 1. These are high computational costs and conflicting demands for the finite element mesh size.

2.3.1 Size scales

Rousselier et al. (1989) proposed an inter-inclusion spacing, l_c, as a ductile fracture propagation step. Their metallographic examinations resulted in the value $l_c = 0.55$ mm for A508 steel.

Tvergaard and Needleman (1984) introduced D_0, the initial spacing between particle centres. They reported $D_0 \sim 0.1 - 0.14$ mm for an unspecified high strength steel.

Some modern steels contain very few or indeed no detectable larger inclusions (typically MnS). Some authors suggested a spacing between larger precipitates as a suitable measure of a ductile fracture advance step. For a high purity laboratory rolled thermo mechanically controlled rolled (TMCR) steels Davis (2003) suggested the values of around 0.01 mm.

A ferritic grain size for tempered bainitic microstructures and a lath packet size for microstructures related to segregated bands were linked to brittle fracture propagation step by Beremin (1983). The values reported for A508 steel were 0.011 mm for a ferritic grain size and 0.067 mm for a lath packet size. These values led to the choice of the appropriate reference material volume, V_0, (section 2.2.2). V_0 was taken as a cube with side 0.05 mm, which for A508 includes about 8 grains.

The concept of a *damage cell* or a *computational cell* (Xia and Shih, 1996; Faleskog and Shih, 1997) is used to introduce the above microstructurally significant size scales into the local approach to fracture mechanics methods.

Two ways of implementing the damage cell concept via FE methods have been explored over the years.

The easiest approach is to associate a damage cell with each FE in or near the damage zone. This assumes constructing the mesh of the damage zone with damage cell sized FEs (Tvergaard and Needleman, 1984; Rousselier et al., 1989; Howard et al., 1996; Xia and Shih, 1996; Koppenhoefer and Dodds, 1998).

In the other method FE sizes are not fixed to that of the damage cell. Instead an additional size parameter is introduced into the model. This results in a mesh-independent, *non-local* use of the theory (Bilby, Howard and Li, 1994; Howard et al., 2000).

The damage cell sizes reported in the literature are 0.1 – 0.5 mm for ductile

damage and 0.005 – 0.05 mm for brittle fracture. Whatever the exact values for the ductile and brittle cell sizes are, they are substantially different. It is therefore difficult to accommodate both damage cell sizes within one FE mesh.

The compromise approach is to use a unified damage cell for both types of fracture. A damage cell of 0.125 mm was used by Sherry et al. (1998); Burstow (1998); Howard et al. (2000) as a reasonable compromise between 0.05 mm brittle and 0.25 – 0.5 mm ductile damage cells. Howard et al. (2000) reported that performance of such a compromise model is virtually indistinguishable from that of a more complicated mesh-independent model (Bilby, Howard and Li, 1994).

2.3.2 Brittle fracture as a postprocessing operation

This approach involves two stages.

At the first stage a finite element solution is obtained using the local approach model for ductile damage. The stress history of all FEs in the plastic zone is saved during the analysis.

The second stage consists of applying the weakest link statistical model to the stress evolution data. The result is a probability of brittle failure as a function of crack advance or time.

Various combinations of ductile and brittle models described in sections 2.1 and 2.2 can be used. The most popular are the GTN + Beremin (sections 2.1.4 and 2.2.2) (Xia and Shih, 1996; Xia and Cheng, 1997; Koppenhoefer and Dodds, 1998) and Rousselier + Beremin (section 2.1.6 and 2.2.2) (Eripret et al., 1996; Sherry et al., 1998; Burstow, 1998; Howard et al., 2000).

This approach assumes a loss of stability associated with rapid loss of stiffness somewhere in the damage zone as the onset of the catastrophic brittle fracture. So this model can only predict the time of the critical event. Neither the cleavage initiation site nor the shape of the crack can be predicted.

2.3.3 Folch model

In the model introduced by Folch the onset of cleavage of each damage cell is assessed individually (Folch, 1997; Folch and Burdekin, 1999). In other words the integration in equation (2.30) is performed over a volume of material within

individual cell. It is easy to see that if the reference volume, V_0, is equal to the cell volume and the threshold stress, σ_{th}, is zero then the Weibull stress, σ_w, is just the maximum principal stress. Therefore the equation 2.29 will have the following form:

$$\Phi = 1 - \exp\left[-\left(\frac{\sigma_{\mathrm{I}}}{\sigma_u}\right)^m\right], \tag{2.32}$$

so that the probability of cleavage is based only on the ratio of the maximum principal stress to the scale parameter of a Weibull distribution. Such a condition is very similar to the criterion for the onset of cleavage expressed by equation 2.24.

In this approach the probability of cleavage of each cell is calculated at the same time as its constitutive response. So both ductile and brittle fractures can be modelled simultaneously. What is more important is that the progressive element to element brittle fracture propagation can be simulated. The cleavage initiation sites can now be identified and the brittle crack front can be obtained explicitly. The authors reported good agreement with the results of Charpy and the fracture toughness tests (Folch, 1997; Folch and Burdekin, 1999).

However the model is still limited by the compromise cell size.

2.4 Model calibration

Any continuous ductile damage or a statistical cleavage model has to be calibrated for a particular material, so that model parameters can be considered true material properties.

A three-stage calibration of a GTN model was proposed by Faleskog et al. (1998). In the first stage the parameters of the constitutive equation of the model, q_1, q_2 and q_3, are tuned so that GTN model predicts the same void growth as the model of a discrete spherical cavity. The second stage consists of tuning the critical and final fracture values of void volume fraction, f_c and f_f, using a coalescence mechanics (Faleskog and Shih, 1997). The last stage is the fracture process calibration in which a ductile cell size, L_D, and an initial void volume fraction, f_0, are tuned by reproducing the behaviour of a fracture test. This can be a fracture toughness, a single-edge-notched (SEN) bending or a SEN tensile test (Gao et al., 1998).

The above analysis is equally applicable to any other continuous ductile damage model.

In practice however many people use a simplified calibration procedures. In many cases L_D is calculated with an empirical relationship, e.g. $L_D = 2N_v^{-1/3}$ (Rousselier, 1987) or $L_D = 5N_v^{-1/3}$ (Rousselier et al., 1989), where N_v is the average number of inclusions per unit volume. Empirical relationships are also used for f_0. Of these the most popular is Franklin's formula based on the Mn and S contents in a steel (Franklin, 1969). However other estimates are also used, e.g. $f_0 = \frac{\pi}{6} d_x d_y d_z N_v$, where d_x, d_y and d_z are the average inclusion sizes in three perpendicular dimensions (Batisse et al., 1987). The rest of the model parameters are tuned to reproduce the results of a fracture test.

To tune the shape, m, and the scale, σ_u, parameters of a Weibull distribution for the weakest-link statistical model the maximum likelihood method is usually used (Khalili and Kromp, 1991; Burstow, 1998; Gao et al., 1999).

2.5 Conclusion

Although considerable success in the prediction of failure of engineering structures has been achieved over the last twenty years with the use of the local approach to fracture, there are several important problems that demand further investigation.

Among significant achievements of the coupled ductile-brittle fracture modelling and the local approach to fracture in general one can list successful predictions of all four spinning cylinder tests designed by AEA Technology, Risley, UK (Lidbury et al., 1994; Bilby, Howard, Othman, Lidbury and Sherry, 1994; Howard et al., 1996) and of the NESC (Network for Evaluating Steel Components) experiment (Sherry et al., 1998).

However all attempts to date to transfer cleavage results from notched tensile tests to precracked specimens failed (Howard et al., 2000).

The other two problems are long computational times and the conflicting demands of the FE mesh size.

The author believes that the last two problems are rooted in the fact that the local approach to fracture utilises finite element methods as its vehicle. This

vehicle might not be fully appropriate for use in microstructure-related fracture analysis.

The author's thesis is that a combination of cellular automata and finite element methods is more suitable for this task. The next chapter gives the presentation of the proposed approach.

Chapter 3

The CAFE solution

3.1 A CAFE model

A combination of cellular automata and finite elements (CAFE) has been used successfully for solidification (Gandin et al., 1999; Vandyoussefi and Greer, 2002), static recrystallisation (Raabe and Becker, 2000) or oxide scale failure (Das et al., 2001; Das, 2002; Das et al., 2003) modelling.

The CAFE model proposed here is a logical continuation of works by Bilby, Howard and Li (1994), Folch (1997), Folch and Burdekin (1999), Raabe and Becker (2000) and Das (2002). The structure of this model was first presented by Beynon et al. (2002).

As opposed to pure finite element fracture modelling, where a finite element is a structural and material unit simultaneously, the present model, as indeed all CAFE models, separates the structure from the material. Separate independent entities are used to carry structural and material information.

A finite element is completely defined by its stiffness matrix, D_{ijkl}, and by the interpolation functions, $N^p(\xi_k)$:

$$D_{ijkl} = \frac{\partial \sigma_{ij}}{\partial \epsilon_{kl}} \tag{3.1}$$

$$u_{ij}(\xi_k) = N^p(\xi_k) u_{ij}^p \tag{3.2}$$

where σ_{ij} is the Cauchy (or true) stress tensor, ϵ_{kl} is the logarithmic (or true) strain tensor, u_{ij}^p is the displacement tensor at the finite element node p, $p = 1 \dots P$, P is the total number of nodes in a finite element and ξ_k is the finite

element parametric coordinates tensor, $k = 1, 2, 3$ and $\xi_k = [-1 \ldots + 1]$; $u_{ij}(\xi_k)$ is the displacement tensor at point ξ_k of a finite element (HKS, 2001).

If heat transfer is not taken into account then material behaviour at an integration (or Gaussian or material) point r is described by a constitutive equation of the form

$$\dot{\sigma}_{ij}^r = f(\dot{\epsilon}_{ij}^r) \tag{3.3}$$

where $\dot{\sigma}_{ij}^r$ and $\dot{\epsilon}_{ij}^r$ are stress and strain rate tensors respectively at an integration point r, $r = 1 \ldots R$, R is the total number of integration points per finite element.

The separation of a conventional material finite element into a structural and a material units is shown schematically in Figure 3.1.

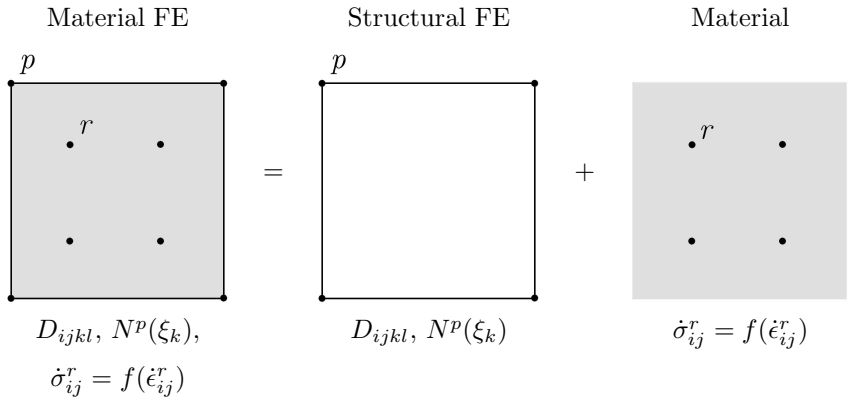

Figure 3.1: A finite element as a structural and a material unit.

In a CAFE model the role of material unit is given to an appropriate number of arrays of cellular automata (CA).

A CA is a discrete time entity composed of a finite number of cells. The space of cell states is also discrete. In a classical CA formulation (Von Neumann, 1966) the state of each cell Υ_m at time t_{i+1} is completely defined by the state of this and the neighbouring cells at time t_i:

$$\Upsilon_m(t_{i+1}) = \Omega\left(\Upsilon_m(t_i), \Upsilon_l^m(t_i)\right) \tag{3.4}$$

where $\Upsilon_l^m(t_i)$ is the state of cell l from the neighbourhood of cell m at t_i, $l = 1 \ldots L$ and L is the number of cells in the neighbourhood of cell m, $m = 1 \ldots M$, M is the total number of cells in the CA; Ω is the transition rule and $i \in \mathbb{N}$.

Thus a CA is completely defined by the initial state of each cell, by the transition rules for each cell and by the neighbourhood of each cell. Usually the same transition rules and neighbourhood are applied to all cells in a CA.

One important property of the CA defined above is that in itself it is a non-spatial entity. This means that cells do not need to have any size, shape or location in physical space for the successful functioning of a CA. Moreover whatever the spatial meaning given to cells there will be no effect on the CA functioning. This property makes CA a very general tool suitable for numerous applications in mathematics and engineering.

A clear spatial meaning has to be given to cells in the present CAFE model since the purpose of a CA is a representation of material behavior where size scale is important. We shall relate a CA cell to a damage cell.

A damage cell or a computational cell concept was described in section 2.3.1. It was shown there that the microstructurally significant size scales related to ductile and brittle fractures are different. Therefore a material has to be modelled with damage cells of two distinctly different sizes. This can be done easily if a CA is chosen to represent material behaviour.

Two independent CAs, called hereafter *the brittle CA array* and *the ductile CA array*, are created. The cell size in the brittle CA array is related to the brittle damage cell size. Accordingly the ductile CA array cell size is related to the ductile damage cell size.

The cubic shape of CA cells is adopted by analogy with the square (in two dimensions) or cubic (in three dimensions) damage cells routinely used in pure finite element fracture modelling (Xia and Shih, 1996; Howard et al., 2000). Cubic CA cells are also the easiest for visualisation which is a problem for three-dimensional structures. Finally the CA cell neighbourhood can be defined very easily for a cubic cell.

A 26-cell neighbourhood is adopted in the present model for each cell. If one imagines a $3 \times 3 \times 3 = 27$ cell cube then the 26 cells lying around the central one are its neighbourhood. Six cells of this neighbourhood have a common side with the central cell; 12 cells have a common edge and 8 – a common corner. Such a neighbourhood is a three-dimensional analogy of Moore's two-dimensional 8-cell neighbourhood (Hesselbarth and Göbel, 1991; Das, 2002). The properties

of this 26-cell neighbourhood are given in Appendix A.

A CA must have self-closing boundary conditions if each cell is to have the same 26-cell neighbourhood. Self-closing means that for a cell lying at the edge of a CA the corresponding cells of the opposite edge are considered adjacent. So a 26-cell neighbourhood of an edge cell consists of cells located at opposite CA edges.

The 26-cell neighbourhood of a corner cell is shown in Figure 3.2.

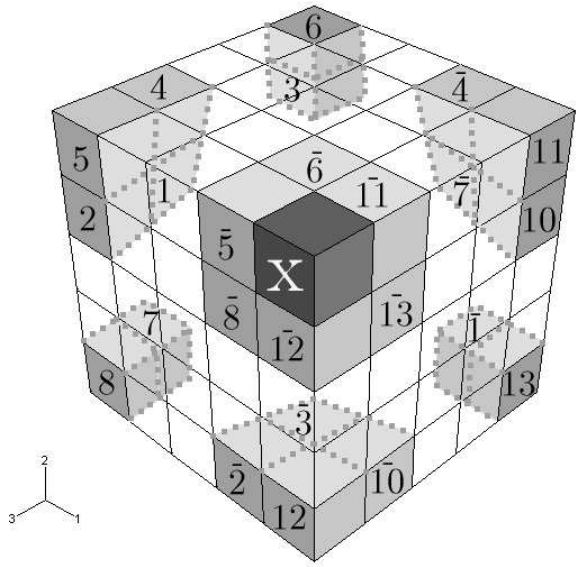

Figure 3.2: A 26-cell neighbourhood of a corner cell in a CA with self-closing boundary conditions.

A corner cell, x, is located at a "corner" of a three-dimensional cubic CA. This corner is an intersection of three CA edges. The numbers of the neighbouring cells are shown according to the convention given in Appendix A. In the projection shown in Figure 3.2 the neighbouring cells 9 and $\bar{9}$ are located exactly behind cell x and are therefore not visible. Cell $\bar{9}$ is situated immediately behind cell x, and cell 9 occupies the corner of CA opposite to cell x.

The CA structure described above is a classical CA formulation (Von Neumann, 1966). We shall now depart from the classical CA model by assigning a set of properties to each cell of a CA. These are the properties which are set at the beginning of the simulation and remain constant throughout the analysis.

We shall also characterise a cell by a set of time-dependent state variables.

By adding the cell properties and state variables to the right part of equation (3.4) we get the following evolution equation:

$$\Upsilon_m(t_{i+1}) = \Omega\left(\Upsilon_m(t_i), \Upsilon_l^m(t_i), \Lambda_m^n, \Lambda_l^n, \Gamma_m^q(t_i)\right) \tag{3.5}$$

where Λ_m^n is property n of cell m, $n = 1 \ldots N$, N is the total number of properties of each cell; Λ_l^n is property n of a neighbouring cell l and $\Gamma_m^q(t_i)$ is a state variable q of cell m at time t_i, $q = 1 \ldots Q$, Q is the total number of state variables defined at each CA cell.

For simplicity we shall require that all cells of a CA have the same N and the same Q. If this requirement is met then all cells of a CA can be processed according to a unified algorithm.

We shall use the cell properties, Λ_m^n, to store some intrinsic material information throughout the analysis. On the other hand the state variables, $\Gamma_m^q(t_i)$, would come from the solution of material constitutive equations at time t_i.

The number of cell properties and state variables is theoretically unlimited. Exactly which material properties and solution-dependent state variables are being represented in a CA depends on the particular realisation of the above CAFE generalisation.

Finally we have to address the fact that two CA arrays, the brittle and the ductile, occupy the same physical space. Therefore the state of cell m of one CA array will depend on the states of a group of S corresponding cells of the other CA array. This is necessary to ensure that any loss of material integrity, whether due to the ductile or the brittle failure mechanism, is accounted for in both CA arrays.

The full transfer rules for both CA arrays thus have the following form:

$$\begin{aligned} \Upsilon_{m(D)}(t_{i+1}) &= \Omega_D\Big(\Upsilon_{m(D)}(t_i), \Upsilon_{l(D)}^m(t_i), \Lambda_{m(D)}^n, \Lambda_{l(D)}^n, \Gamma_{m(D)}^q(t_i), \\ &\quad \Upsilon_{s(B)}(t_{i+1})\Big) \end{aligned} \tag{3.6}$$

$$\begin{aligned} \Upsilon_{m(B)}(t_{i+1}) &= \Omega_B\Big(\Upsilon_{m(B)}(t_i), \Upsilon_{l(B)}^m(t_i), \Lambda_{m(B)}^n, \Lambda_{l(B)}^n, \Gamma_{m(B)}^q(t_i), \\ &\quad \Upsilon_{s(D)}(t_{i+1})\Big) \end{aligned} \tag{3.7}$$

where subscripts D and B refer to cells from the ductile and the brittle CA arrays accordingly, cell s belongs to the group of S cells of one CA array, the

states of which will have an influence on cell m of the other CA array, $s = 1 \dots S$, $1 \leq S \leq M$.

The number of cells S of one CA array which will affect the state of cell m of the other CA array is difficult to establish exactly. As will be shown later S depends on the total number of cells in each array, M_D and M_B.

The brittle and the ductile CA arrays are totally independent of each other as far as their construction is concerned. This means that the number and the types of cells states, $\Upsilon_{m(D)}$ and $\Upsilon_{m(B)}$, the total numbers of cells in these arrays, M_D and M_B, the total numbers and types of cell properties, N_D and N_B, and state variables, Q_D and Q_B, and finally the transfer functions, Ω_D and Ω_B can be chosen for each array independently. This gives us great freedom as to how exactly material behaviour is represented through the two CA arrays.

However the cell states in the ductile CA array are affected by the states of cells in the brittle CA array and vice versa. This property ensures that any change in material integrity, no matter what fracture mechanism caused it, is accounted for in both CA arrays.

Similarly to the way we introduced time-dependent state variables at each CA cell, $\Gamma^q_m(t_i)$, to link the state of each cell with the solution of material constitutive equations, we shall now introduce solution-dependent state variables Y^r_a at each finite element integration point r linked to the states of both CA arrays:

$$Y^r_a(t_{i+1}) = \Xi\left(\Upsilon_{m(D)}(t_{i+1}), \Upsilon_{m(B)}(t_{i+1})\right) \tag{3.8}$$

where $Y^r_a(t_{i+1})$ is state variable a at time t_{i+1} and integration point r, $a = 1 \dots A$, A is the total number of state variables per integration point and Ξ is the CA to FE transfer function. The same transfer function is used for all material points.

Up until now we described the general principles of the ductile and the brittle CA organisation and the link between them. The link between the FE and the CA parts of a CAFE model depends on the exact technical realisation of a CAFE generalisation. The rest of this chapter will deal only with the CAFE model realised in the present work.

3.2 The full model

The CAFE model was realised via the user material subroutine `VUMAT` in the `Abaqus/Explicit` finite element code. This program utilises explicit dynamic integration of the equations of motion. Reduced integration 8-node finite elements `C3D8R` (HKS, 2001) were used to mesh the anticipated damage zone. These elements have only one integration point (R=1).

The explicit dynamic version of the `Abaqus` code was chosen because of the element removal feature which is not available in the `Abaqus/Standard`. The removal of dead finite elements from the mesh is necessary in large deformation analysis. Otherwise the dead elements, which have the highest strains, might turn inside out. The solution will terminate in this case.

The general structure of a CAFE model is shown in Figure 3.3.

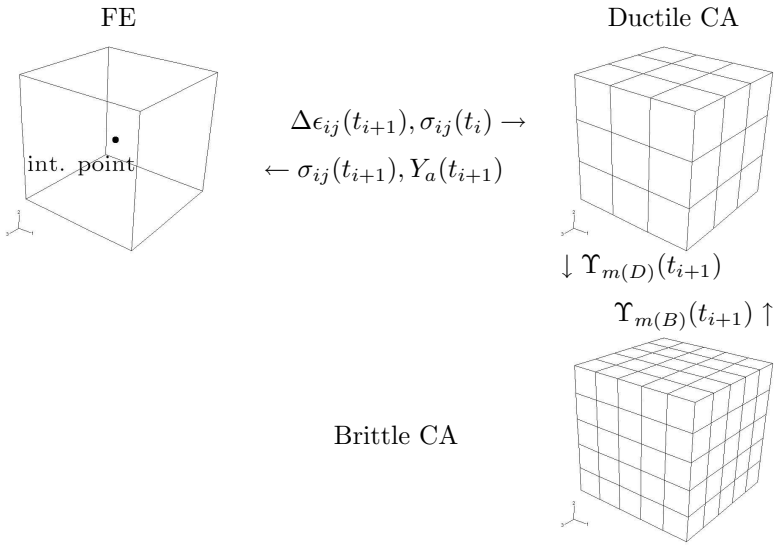

Figure 3.3: Flow of information between the three parts of the full CAFE model.

The flow of information between the three parts of the CAFE model is shown schematically with the arrows. However, the scheme does not show how the data is being processed within each part of the whole model.

3.2.1 The ductile CA array

The Rousselier continuous ductile damage model is used as a material constitutive routine for the ductile CA array (section 2.1.6).

As we said in section 3.1 the ductile CA cells are related to the ductile damage cells. Therefore the total number of cells per ductile CA, M_D, has to be chosen so that the linear size of an individual ductile CA cell is close to the ductile damage cell size, L_D. If we assume a cubic finite element of size $L_{FE} \times L_{FE} \times L_{FE}$ then the following equation can be used to choose M_D:

$$\frac{L_{FE}}{\sqrt[3]{M_D}} = L_D \tag{3.9}$$

where $\sqrt[3]{M_D}$ is the number of cells per dimension of a cubic ductile CA.

Each ductile cell m can take one of the two possible states, $\Upsilon_{m(D)}$,: *alive* or *dead*. In the beginning of the simulation $\Upsilon_{m(D)}(t_0) = alive$.

Each ductile cell m has only one cell property ($N_D = 1$), this is the value of initial void volume fraction, $\Lambda^1_{m(D)} = f_0^m$. A random number generator is used to generate f_0^m for each cell at the beginning of the simulation.

Each ductile cell m carries only one state variable ($Q_D = 1$), this is the current value of the damage parameter, $\Gamma^1_{m(D)}(t_i) = \beta_m(t_i)$.

The same critical value of the damage variable, β_{F}, is used for all ductile cells. Therefore β_{F} is a model parameter rather than a cell property.

The state of each cell m is determined by the following criterion:

$$\Upsilon_{m(D)}(t_{i+1}) = \begin{cases} alive & \text{if} \quad \beta_m(t_{i+1}) < \beta_{\mathrm{F}} \\ dead & \text{otherwise} \end{cases} \tag{3.10}$$

3.2.2 The brittle CA array

Similarly to section 3.2.1 the link between the brittle damage cell size, L_B, and the total number of brittle CA cells is as follows:

$$\frac{L_{FE}}{\sqrt[3]{M_B}} = L_B \tag{3.11}$$

where $\sqrt[3]{M_B}$ is the number of cells per dimension of a cubic brittle CA.

As was shown in section 2.3.1 a brittle damage cell is typically 10 – 20 times larger than the mean (or median or mode) grain size.

Ideally, a brittle cell size has to be related to a grain size for a progressive grain-to-grain fracture simulation. However for steels with small grain sizes this will lead to extremely high numbers of brittle cells.

The following compromise approach is proposed in this work. The brittle cell size is chosen with equation (3.11). However a randomly generated grain size value is assigned to each brittle cell. Therefore computational efficiency can be achieved while some real metallurgical data is retained in the brittle CA array.

According to the present understanding of brittle fracture initiation (section 2.2.1) a brittle crack typically initiates from a hard particle. Most usually this is a grain boundary carbide or a large inclusion, e.g. MnS. We simplify this idea for the purpose of the present modelling and formulate the following necessary condition for brittle crack initiation at a particular cell. Only cells with an adjacent grain boundary carbide can initiate brittle fracture. Thus large inclusions are not taken into account at present. However, as will be shown in Chapter 5 the influence of large inclusions can be easily incorporated into the model if only the information regarding the size, number and locations of such particles is available.

Accordingly a special state of the brittle CA cell is created – *alive with a grain boundary carbide* or simply *aliveC*. Only brittle cells with $\Upsilon_{m(B)}(t_0) = aliveC$ can initiate a brittle crack.

We have to address the problem of synchronising both CA arrays. All ductile failures must be reflected into the brittle CA array. However a distinction must be made between the brittle cells failed due to the brittle failure mode, and those which were made dead artificially to synchronise the integrity of both CA arrays. A special state of brittle CA cell is created – *dead in the ductile CA array* or simply *deadD*.

Finally the state *deadB* is reserved for the brittle CA cells which fail when the brittle failure criterion is satisfied.

Thus each brittle cell can take one of the four possible states, $\Upsilon_{m(B)}$,: *alive*, *aliveC*, *deadB* or *deadD*.

In the beginning of the simulation $\Upsilon_{u(B)}(t_0) = aliveC$ and $\Upsilon_{v(B)}(t_0) = alive$, $u = 1 \ldots U$, $v = 1 \ldots V$, $U + V = M_B$. So the fraction of brittle cells

which have a grain boundary carbide is $\eta = U/M_B$. A random number generator is used to assign the initial state to cells.

Each brittle cell m has two cell properties ($N_B = 2$), these are the fracture stress, $\Lambda^1_{m(B)} = \sigma^m_{\mathrm{F}}$, and the grain orientation angle, $\Lambda^2_{m(B)} = \alpha^m$. The grain orientation angle is obtained with a random number generator.

The use of only one grain orientation angle is, of course, a modelling simplification. In principle two angles are required to describe a crystal orientation (Kelly and Groves, 1970). However, what really matters in modelling crack propagation from one grain to another, is the grain misorientation angle, that is the minimum of all angles formed by the pairs of the crystallographic planes, where each pair contains one crystallographic plane of one grain and one crystallographic plane of the other grain. The calculation of the grain misorientation angle is very easy if each grain is described by only one orientation angle. However, it is a much more computationally expensive task if the orientation of each grain is described by two angles.

Perhaps it would be more correct to call α^m a grain orientation angle class or type. This would imply that α^m denotes a particular combination of two grain orientation angles. Accordingly if l is a grain (brittle cell) adjacent to grain m then $|\alpha^m - \alpha^l|$ is a difference between the orientation classes (types) of grains m and l. This is taken as an analogue of the true grain misorientation angle.

The fracture stress of a cell is linked to the size of the grain that this cell embodies (equation (2.26) of section 2.2.1). A random number generator is used to generate a grain size, d_g, for each cell. Then a fracture stress is assigned to each cell based on the generated grain size.

Each brittle cell m carries only one state variable ($Q_B = 1$), this is the current value of the maximum principal stress, $\Gamma^1_{m(B)}(t_i) = \sigma^m_{\mathrm{I}}$.

As was shown in section 2.2.3 a high-angle misorientation grain boundary can inhibit or even arrest crack growth (Nohava et al., 2002; Bhattacharjee and Davis, 2002; Bhattacharjee et al., 2003). Again we simplify this idea and formulate the following necessary condition for crack propagation. A crack will propagate from one brittle CA cell, m, to another, l, if the misorientation angle for these two cells, defined as the absolute value of the difference of their orientation angles, $\mid \alpha^m - \alpha^l \mid$, is less than a misorientation threshold, θ_{F}. It is

assumed that θ_{F} is a material property.

Finally the following simple propagation criterion is used which must be satisfied in all cases. A brittle cell m will become dead at time t_{i+1} if the maximum principal stress, $\sigma_{\mathrm{I}}^m(t_i)$, is greater than or equal to the fracture stress of this cell, σ_{F}^m. This criterion is identical to that of Folch (1997), section 2.3.3, if we require the probability of failure, $\Phi = 1$, and $\sigma_u = \sigma_{\mathrm{F}}$.

Thus the state of each cell m is determined by the following criterion:

$$\Upsilon_{m(B)}(t_{i+1}) =$$

$$= \begin{cases} deadB & \text{if} \quad \sigma_{\mathrm{I}}^m(t_i) \geq \sigma_{\mathrm{F}}^m \ \wedge \ \Big\{ \big(\Upsilon_{m(B)}(t_i) = aliveC \big) \ \vee \\ & \qquad \Big(\Big[\Upsilon_{l(B)}^m(t_i) = deadB \ \vee \ \Upsilon_{l(B)}^m(t_i) = deadD \Big] \ \wedge \\ & \qquad \mid \alpha^m - \alpha^l \mid < \theta_{\mathrm{F}} \Big) \Big\} \\ \Upsilon_{m(B)}(t_i) & \text{otherwise} \end{cases} \tag{3.12}$$

3.2.3 The FE part

Each material point has three solution-dependent variables ($A = 3$): state, $Y_1(t_i)$, integrity, $Y_2(t_i)$, and the fraction of brittle phase, $Y_3(t_i)$. As follows from equation (3.8) the FE state variables depend on the states of the brittle and ductile CA cells.

First, the number of brittle CA cells with $\Upsilon_{m(B)}(t_i) = deadB$,

$$X_{(B)}^B(t_i) = \sum_{m=1}^{M_B} m \quad \forall m : \Upsilon_{m(B)}(t_i) = deadB, \tag{3.13}$$

the number of brittle CA cells with $\Upsilon_{m(B)}(t_i) = deadD$,

$$X_{(B)}^D(t_i) = \sum_{m=1}^{M_B} m \quad \forall m : \Upsilon_{m(B)}(t_i) = deadD, \tag{3.14}$$

the total number of dead brittle CA cells,

$$X_{(B)}(t_i) = X_{(B)}^B(t_i) + X_{(B)}^D(t_i), \tag{3.15}$$

and the total number of dead ductile CA cells,

$$X_{(D)}(t_i) = \sum_{m=1}^{M_D} m \quad \forall m : \Upsilon_{m(D)}(t_i) = dead, \tag{3.16}$$

are calculated.

Then the FE state variables are calculated according to the following three equations:

$$Y_3(t_i) = \frac{X^B_{(B)}(t_i)}{X_{(B)}(t_i)} \tag{3.17}$$

$$Y_2(t_i) = 1 - \frac{X_{(D)}(t_i)}{X^{max}_{(D)}} - \frac{X^B_{(B)}(t_i)}{X^{max}_{(B)}} \tag{3.18}$$

$$Y_1(t_i) = \begin{cases} dead & \text{if} \quad Y_2(t_i) \leq 0 \\ alive & \text{otherwise} \end{cases} \tag{3.19}$$

where $X^{max}_{(D)}$ and $X^{max}_{(B)}$ are the maximum numbers of dead cells allowed in the ductile and the brittle CA arrays respectively. If the number of dead cells in any array exceeds its maximum then a crack (or ductile void linkage) is assumed to propagate across the whole of the FE. The load-bearing capacity of this FE is then considered zero and the FE is removed from the mesh.

So $Y_1 \in [alive, dead]$; $Y_2 \in [-1 \dots 1]$ and $Y_3 \in [0 \dots 1]$. In the beginning of the analysis $Y_1(t_0) = alive$, $Y_2(t_0) = 1$ and $Y_3(t_0) = 0$ for all finite elements included in the CAFE model. When a FE fails $Y_1(t_f) = dead$ and $Y_2(t_f) = 0$, where t_f is the time of a FE failure.

3.2.4 How the model works

As seen from sections 3.2.1 and 3.2.2 there is a fundamental difference between the roles of the ductile and the brittle CA arrays in the full model. While the ductile CA array is used to calculate material constitutive response, the brittle CA array is only used to assess the onset of brittle fracture at each cell. Before the brittle CA cells can be processed to decide if any of them have died in this time increment, the material response has to be calculated via the ductile array (Figure 3.3).

Below is the sequence of operations performed at each time increment for each FE and the corresponding two CA arrays of the CAFE model.

All tensors given to the `VUMAT` subroutine are in the local material orientation.

Step 1. Strain increment tensor at time t_{i+1}, $\Delta\epsilon_{ij}(t_{i+1})$, and the stress tensor at time t_i, $\sigma_{ij}(t_i)$, at the FE integration point are given by the `Abaqus` solver to the `VUMAT` subroutine.

Step 2. The maximum principal stress, $\sigma_{\mathrm{I}}(t_i)$, and its direction cosines, $d_k(t_i)$, are calculated from $\sigma_{ij}(t_i)$.

Step 3. The strain increment tensor at each ductile CA cell m at time t_{i+1}, $\Delta\epsilon^m_{ij}(t_{i+1})$, is calculated. The following criteria are used:

$$\forall m \quad \Delta\epsilon^m_{ij(D)}(t_{i+1}) = \Delta\epsilon_{ij}(t_{i+1}) \tag{3.20}$$

$\forall m : \Upsilon_{m(D)}(t_i) = dead$:

$$\text{if} \quad d^l_k \cdot d_k(t_i) \approx 1 \quad \text{then} \quad \Delta\epsilon^l_{ij(D)}(t_{i+1}) = c_D \cdot \Delta\epsilon_{ij}(t_{i+1}) \tag{3.21}$$

where $c_D > 1$ is the concentration factor for the ductile CA array and d^l_k are the direction cosines of the line connecting the centres of cells m and l (see Appendix A).

Then the strains at all M_D ductile CA cells are scaled so that the average of the cell strains gives the FE strain:

$$\frac{1}{M_D}\sum_{m=1}^{M_D} \Delta\epsilon^m_{ij(D)}(t_{i+1}) = \Delta\epsilon_{ij}(t_{i+1}) \tag{3.22}$$

The condition of equation (3.21) means that if there is a dead ductile cell then all neighbouring cells which lie on or near the plane perpendicular to the direction of the maximum principal FE stress will receive some strain concentration. This condition reflects the strain concentration in material surrounding a void. The '$\approx$' sign rather than '$=$' is used in the 'if' part of equation (3.21) because there are only 13 pairs of neighbouring cells with unique combinations of d^l_k (see Appendix A). So it is very unlikely that $d^l_k \cdot d_k(t_i) = 1$.

Step 4. The stress at time t_{i+1} at each ductile cell m, $\sigma^m_{ij}(t_{i+1})$, and the value of the damage variable, $\beta_m(t_{i+1})$, are obtained via the solution of the set of equations of the Rousselier continuous ductile damage model (section 2.1.6 and Appendix B).

Step 5. The state of each ductile cell m at time t_{i+1}, $\Upsilon_{m(D)}(t_{i+1})$, is obtained according to equation (3.10).

Step 6. All dead ductile CA cells are reflected into the brittle CA array (section 3.2.2). A special mapping function, $\mathbb{M}_{D\to B}$, distributes the array of ductile

CA cell states, $\Upsilon_{m(D)}(t_{i+1})$, across the brittle CA array. The result is the "synchronisation" array of the brittle CA cell states, $\Upsilon_{m(BD)}(t_{i+1})$.

$$\Upsilon_{m(BD)}(t_{i+1}) = \mathbb{M}_{D\to B}\left(\Upsilon_{\bar{m}(D)}(t_{i+1})\right) \tag{3.23}$$

The subscript "BD" means that each brittle cell m has the state of the ductile cell occupying the same physical space. The subscript $\bar{m}$ instead of usual m is used in the right part of equation (3.23) because $M_B \neq M_D$, so $\bar{m} = 1 \ldots M_D$ and $m = 1 \ldots M_B$. This change of notation is only used in equations (3.23) and (3.29).

The space of states of $\Upsilon_{m(BD)}$ is the same as of $\Upsilon_{m(D)}$, either *dead* or *alive*.

The $\Upsilon_{m(BD)}(t_{i+1}) = dead$ means that there is a ductile void in the physical space associated with brittle cell m. So the state of brittle cell m is changed to *deadD* to acknowledge this fact. This is expressed by the following equation

$$\Upsilon_{m(B)}(t_{i+1}) = \begin{cases} deadD & \text{if} \quad \Upsilon_{m(BD)}(t_{i+1}) = dead \wedge \\ & \quad \left(\Upsilon_{m(B)}(t_i) = alive \vee \right. \\ & \quad \left. \Upsilon_{m(B)}(t_i) = aliveC\right) \\ \Upsilon_{m(B)}(t_i) & \text{otherwise} \end{cases} \tag{3.24}$$

The work of mapping function $\mathbb{M}_{D\to B}$ is illustrated in Figures 3.4.a and 3.4.b.

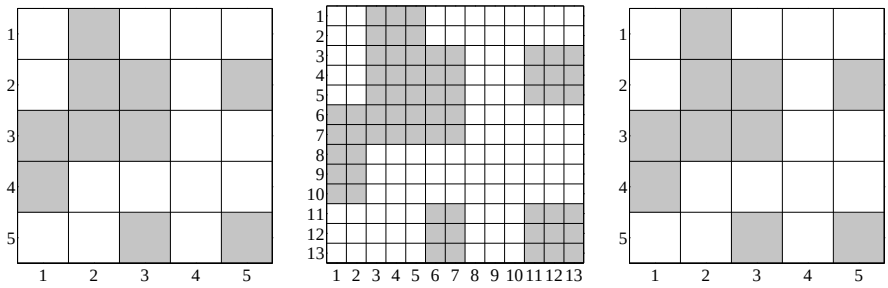

a. Ductile (in) b. Brittle (out/in) c. Ductile (out)

Figure 3.4: Illustration of the mapping operations, $\mathbb{M}_{D\to B}$ and $\mathbb{M}_{B\to D}$.

Figure 3.4.a shows a two-dimensional slice of $\Upsilon_{m(D)}(t_{i+1})$. Dead cells are grey and the white ones are alive. Figure 3.4.b shows a two-dimensional slice

of $\Upsilon_{m(BD)}(t_{i+1})$. It is easy to see that the locations of groups of grey cells in $\Upsilon_{m(BD)}(t_{i+1})$ are close to locations of grey cells in $\Upsilon_{m(D)}(t_{i+1})$. Because of the discrete nature of the CA space, the dead cells in $\Upsilon_{m(BD)}(t_{i+1})$ will occupy exactly the same physical space as the dead cells in $\Upsilon_{m(D)}(t_{i+1})$ only if the number of cells per linear brittle CA dimension, $\sqrt[3]{M_B}$, is divisible by the number of cells per linear ductile CA dimension, $\sqrt[3]{M_D}$:

$$\mod \sqrt[3]{\frac{M_B}{M_D}} = 0 \tag{3.25}$$

In the example shown in Figures 3.4.a and 3.4.b $\sqrt[3]{M_B} = 13$ and $\sqrt[3]{M_D} = 5$, so the condition of equation (3.25) does not hold. Therefore the locations of dead (grey) cells in physical space in $\Upsilon_{m(D)}(t_{i+1})$ and in $\Upsilon_{m(BD)}(t_{i+1})$ are only close to each other, but not identical.

Step 7. This step is the brittle CA analogue for the ductile CA (Step 3).

The maximum principal stress in each brittle CA cell m at time t_{i+1}, $\sigma_{\mathrm{I}}^m(t_i)$, is calculated. The following criteria are used:

$$\forall m \quad \sigma_{\mathrm{I}}^m(t_i) = \sigma_{\mathrm{I}}(t_i) \tag{3.26}$$

$$\forall m : \Upsilon_{m(B)}(t_i) = deadB : \text{ if } d_k^l \cdot d_k(t_i) \approx 1 \text{ then } \sigma_{\mathrm{I}}^l(t_i) = c_B \cdot \sigma_{\mathrm{I}}(t_i) \tag{3.27}$$

$$\forall m : \Upsilon_{m(B)}(t_i) = deadD : \text{ if } d_k^l \cdot d_k(t_i) \approx 1 \text{ then } \sigma_{\mathrm{I}}^l(t_i) = c_D \cdot \sigma_{\mathrm{I}}(t_i) \tag{3.28}$$

where $c_B > 1$ is the concentration factor for the brittle CA array.

The meaning of equations (3.27) and (3.28) for the brittle CA array is similar to that of equation (3.21) for the ductile CA array (Step 3).

Step 8. This step is the brittle CA analogue for the ductile CA (Step 5).

The state of each brittle cell m at time t_{i+1}, $\Upsilon_{m(B)}(t_{i+1})$, is obtained according to equation (3.12).

Step 9. This step is the brittle CA analogue for the ductile CA (Step 6).

All dead brittle CA cells are reflected into the ductile CA array. A special mapping function, $\mathbb{M}_{B\to D}$, distributes the array of brittle CA cell states, $\Upsilon_{m(B)}(t_{i+1})$, across the ductile CA array. The result is the "synchronisation" array of the ductile CA cell states, $\Upsilon_{m(DB)}(t_{i+1})$.

$$\Upsilon_{\bar{m}(DB)}(t_{i+1}) = \mathbb{M}_{B\to D}\left(\Upsilon_{m(B)}(t_{i+1})\right) \tag{3.29}$$

The subscript "DB" means that each ductile cell $\bar{m}$ has the state of the brittle cell occupying the same physical space. The subscript $\bar{m}$ instead of usual m is used in the left part of equation (3.29) because $M_B \neq M_D$, so $\bar{m} = 1 \dots M_D$ and $m = 1 \dots M_B$. This change of notation is used only in equations (3.29) and (3.23).

The space of states of $\Upsilon_{m(DB)}$ is the same as of $\Upsilon_{m(D)}$, either *dead* or *alive*.

The $\Upsilon_{m(DB)}(t_{i+1}) = dead$ means that there is a brittle crack in the physical space associated with ductile cell m. So the state of ductile cell m is changed to *dead* to acknowledge this fact. This is expressed by the following equation

$$\Upsilon_{m(D)}(t_{i+1}) = \begin{cases} dead \text{ if } \Upsilon_{m(DB)}(t_{i+1}) = dead \wedge \Upsilon_{m(D)}(t_i) = alive \\ \Upsilon_{m(D)}(t_i) \quad \text{otherwise} \end{cases} \tag{3.30}$$

In contrast with the brittle CA array, no special cell state is created in the ductile CA to distinguish between the dead ductile cells due to the ductile failure mode and those made dead artificially for synchronisation (equations (3.24) and (3.30)). So the percentage of brittle phase can only be calculated via the brittle CA.

The operation of mapping function $\mathbb{M}_{B \to D}$ is illustrated in Figures 3.4.b and 3.4.c.

It is important to note that although each of the two mapping functions, $\mathbb{M}_{D \to B}$ and $\mathbb{M}_{B \to D}$, reflects the state of one CA array onto the state of another CA array only approximately, mapping errors do not accumulate. As shown in Figure 3.4 the sequential application of both mapping operations produces a cell state array identical to the initial one. It is easy to see that Figures 3.4.a and 3.4.c are identical. This property of mapping functions can be written symbolically as follows

$$\Upsilon_{m(D)}(t_{i+1}) = \mathbb{M}_{B \to D}\left(\mathbb{M}_{D \to B}\left(\Upsilon_{m(D)}(t_{i+1})\right)\right) \tag{3.31}$$

Step 10. All dead ductile cells receive zero stress:

$$\forall m : \ \Upsilon_{m(D)}(t_{i+1}) = dead \quad \sigma_{ij}^m(t_{i+1}) = 0. \tag{3.32}$$

Step 11. The FE stress at time t_{i+1}, $\sigma_{ij}(t_{i+1})$ is calculated as

$$\sigma_{ij}(t_{i+1}) = \frac{1}{M_D} \sum_m \sigma_{ij}^m(t_{i+1}). \tag{3.33}$$

So the stress at the FE integration point is the average of the stresses of all ductile CA cells, including the dead cells.

Step 12. The FE solution-dependent variables at time t_{i+1}, $Y_k(t_{i+1})$, are calculated according to equations (3.17), (3.18) and (3.19).

Step 13. The FE stress tensor and solution-dependent variables at time t_{i+1}, $\sigma_{ij}(t_{i+1})$ and $Y_k(t_{i+1})$, are returned by the `VUMAT` subroutine to the `Abaqus` solver.

Step 13 completes the cycle.

3.2.5 Problems

1. High computational costs.

The running times of the full CAFE model are two – three orders of magnitude smaller comparing with the pure finite element model where each ductile (or brittle) CA cell is substituted by a finite element of equal size. From this point of view the CAFE model is very fast.

However, a typical simulation time for a full 3D Charpy impact test is days rather than hours (see section 4.1.3). This is because the integration of the Rousselier damage model (Step 4, page 49) has to be performed for each ductile cell. The system of two nonlinear equations is solved in this step using Newton's iterative method (Appendix B). This is a relatively time-consuming operation.

2. Loss of precision due to averaging.

As is shown in Appendix B the elastic strain tensor, ϵ^e_{ij}, which is used in equation (B.8) and is updated according to equation (B.56), has to be stored from one time increment to another throughout the analysis. The elastic strains are typically very small for steels, therefore the components of ϵ^e_{ij} must be calculated with high precision. A small change in ϵ^e_{ij} will lead to a very significant change of the Rousselier model response (σ_{ij} and β).

However, the maintenance of high precision of ϵ^e_{ij} is difficult due to a simplistic strain redistribution criterion (Step 3, page 49) and due to stress averaging (Step 11, page 52).

Each ductile cell will have a unique strain history due to a unique, randomly assigned, initial void volume fraction, f_0^m. A ductile cell m should theoretically receive the strain increment at time t_{i+1}, $\Delta\epsilon^m_{ij(D)}(t_{i+1})$, based on the stress at this cell in the previous time increment, t_i, $\sigma^m_{ij}(t_i)$. However Steps 11 of increment t_i and Step 3 of the next time increment, t_{i+1}, effectively result in the value of $\Delta\epsilon^m_{ij(D)}(t_{i+1})$ being based on the averaged (macro or finite element) stress. This strain increment might be quite far from the "true" strain increment for cell m. $\Delta\epsilon^m_{ij(D)}(t_{i+1})$ directly affects ϵ^e_{ij} for cell m, as expressed by equation (B.56). As a result ϵ^e_{ij} might not be calculated accurately.

The greater the dissimilarity between the deformation histories of two neighbouring ductile cell (related to a dissimilarity of f_0 for these cells), the further ϵ^e_{ij} will be from the "true" value. In its extreme this loss of precision results in ϵ^e_{ij} values which are so far from the accurate ones that the solution of the system of equations (B.1) – (B.7) is meaningless (e.g. negative $\Delta\sigma_{eq}$) or it cannot be found at all. The analysis will terminate at this stage.

The probability of encountering this problem obviously increases with the number of finite elements in the model. For example this problem was never encountered during the CAFE simulation of a single-FE model (sections 4.1.1 and 4.1.2). However it happened on several occasions during the Charpy test modelling, where the CAFE model included 900 finite elements (section 4.1.3).

A simplified CAFE model is proposed which aims to solve the above problems.

3.3 The simplified model

The general structure of the simplified CAFE model is shown in Figure 3.5.

The major difference between the full and the simplified models is that the Rousselier model integration in the latter is performed at the finite element level. The damage variable, $\beta(t_{i+1})$, is given to the ductile CA array in the simplified model instead of the strain increment tensor, $\Delta\epsilon_{ij}(t_{i+1})$. Accordingly only the solution-dependent state variables are returned to the FE from the ductile CA array, as the new macro stress tensor, $\sigma_{ij}(t_{i+1})$, is calculated already at the FE

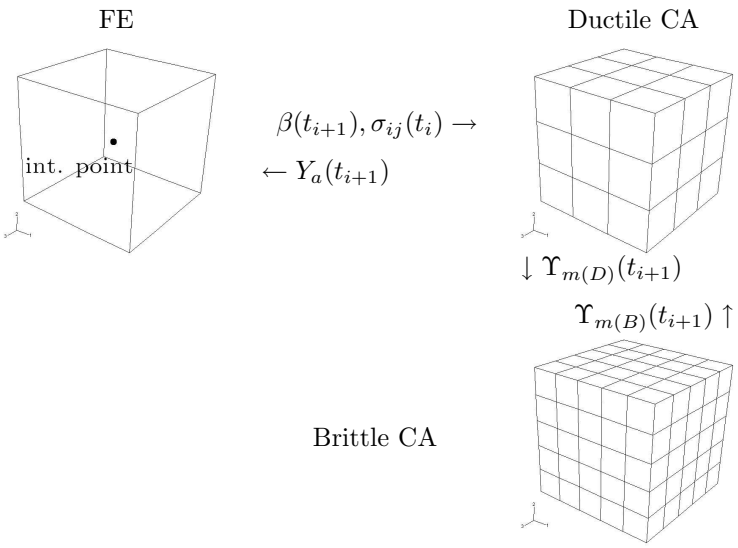

Figure 3.5: Flow of information between the three parts of the simplified CAFE model.

level (Figures 3.3 and 3.5). All other differences between the two models are the consequences of this major one.

The critical value of the damage variable is now a randomly assigned cell property, $\Lambda^1_{m(D)} = \beta^m_{\mathrm{F}}$. So β^m_{F} instead of β_{F} is used in equation (3.10) for the simplified model. The other properties of the ductile CA array are as described in section 3.2.1.

The brittle CA array and the FE part are used exactly as in the full model (sections 3.2.2 and 3.2.3).

3.3.1 How the model works

Below is the sequence of operations performed at each time increment for each FE and the corresponding two CA arrays of the CAFE model.

Step 1. The same as Step 4 of the full model but performed at the FE level. The damage variable at time t_i, $\beta(t_{i+1})$, at the FE integration point is given by the `Abaqus` solver to the `VUMAT` subroutine.

Step 2. The same as for the full model.

Step 3. The same as for the full model but applied to the damage variable.

The damage variable at each ductile CA cell m at time t_{i+1}, $\beta_m(t_{i+1})$, is calculated. The following criteria are used:

$$\forall m \quad \beta_m(t_{i+1}) = \beta(t_{i+1}) \tag{3.34}$$

$\forall m : \Upsilon_{m(D)}(t_i) = dead$:

$$\text{if} \quad d_k^l \cdot d_k(t_i) \approx 1 \quad \text{then} \quad \beta_l(t_{i+1}) = c_D \cdot \beta(t_{i+1}) \tag{3.35}$$

No scaling is performed as opposed to the full model.

Step 4. Not present in the simplified model.

Step 5. – **Step 9.** The same as for the full model.

Step 10. – **Step 11.** Not present in the simplified model.

Step 12. The same as for the full model.

Step 13. The same as for the full model but only solution-dependent variables at time t_{i+1}, $Y_a(t_{i+1})$, are returned by the `VUMAT` subroutine to the `Abaqus` solver.

Step 13 completes the cycle.

It is easy to see that in the simplified model the roles of the ductile and the brittle CA arrays are very similar as opposed to the full model (section 3.2.4).

In the full model the ductile CA array is used for the calculation of material constitutive response and for the simulation of the fracture propagation while the brittle CA array is only used to simulate fracture propagation. In the simplified model both the brittle and the ductile CA arrays are used only for the simulation of the fracture propagation at each CA scale. The material constitutive response is calculated at the FE level.

A significant reduction of computational time is thus achieved. Also there is no averaging in the simplified model since Step 11 is not present. So the accuracy of ϵ_{ij}^e is not reduced.

3.4 Important properties

Both the full and the simplified CAFE models have the following two important properties.

1. In this particular realisation of a CAFE generalisation finite elements with a single integration point (`C3D8R`) have been used. As a consequence there are no stress or strain gradients across finite elements. Therefore mapping procedures such as triangulation (Das, 2002) or the Wigner-Seitz algorithm (Raabe and Becker, 2000) need not be applied to decide which CA cells fall under the influence of a particular integration point.

This property makes the present CAFE models fast. However, care must be taken to ensure that finite element sizes are appropriate for regions of high strain gradients as the accuracy of a single integration point finite element is inevitably not as good as that of a finite element with several integration points.

2. Neither rotation nor deformation of a finite element are transferred to the corresponding CAs. This is a very important property of the present CAFE models. As a consequence the fracture propagation path can only be visualised in the initial finite element configuration. This was a conscious decision.

The present work aims to model and understand the behaviour of a macroscopic sample of material based on micromechanics of fracture. If, however, the emphasis is shifted towards the modelling and understanding of the fracture at the microscale, then all CA arrays have to be rotated and deformed using the deformation gradient tensor at the corresponding integration point (Das, 2002). In this case the exact locations of all cells in physical space will be known throughout the analysis and the fracture propagation path can be visualised on a deformed mesh.

3.5 The list of model parameters

To complete this chapter, the full list of the parameters for both CAFE models is shown below.

1. M_D – the total number of cells in the ductile CA.

2. M_B – the total number of cells in the brittle CA.

3. a probability density function, $f(f_0)$, for the full model and $f(\beta_{\mathrm{F}})$, for the simplified model.

4. η – a fraction of the brittle CA cells to have a grain boundary carbide.

5. a probability density function $f(d_g)$.

6. a probability density function $f(\alpha)$.

7. $X_{(D)}^{max}$ – the maximum number of dead cells allowed per ductile CA.

8. $X_{(B)}^{max}$ – the maximum number of dead cells allowed per brittle CA.

9. c_D – the concentration factor for the ductile CA array.

10. c_B – the concentration factor for the brittle CA array.

Chapter 4

Results

All results in this Chapter were obtained with the following soft- and hardware. The `VUMAT` subroutine was written in `FORTRAN 95`, and compiled and linked with `Compaq Visual Fortran` compiler, version 6.1 (Compaq, 1999). The `Abaqus/Explicit` version 6.2-1 code was used. The platform used was a Pentium III, 1 GHz PC run under Windows 2000 operating system. The amount of operating memory used was approximately 42 MB for the examples in sections 4.1.1 and 4.1.2 and 50 MB for the examples in sections 4.1.3 and 4.2.1.

All examples in this Chapter illustrate the ability of the present CAFE models, both the full and the simplified, to simulate fracture propagation typical of that in a thermomechanically control rolled (TMCR) microalloyed steel. Sections 4.1.1 and 4.1.2 illustrate some important features of the full CAFE model by simulating the fracture propagation in a typical TMCR steel. Fracture of a particular TMCR steel is modelled in sections 4.1.3 and 4.2.1.

4.1 The full CAFE model

4.1.1 Single FE, tension – compression

This simple example is used to demonstrate the behaviour of the full CAFE model.

The model consists of a single cubic 1mm × 1mm × 1mm finite element. The initial shape of the finite element (dashed lines) and the boundary conditions

(arrows) are shown in Figure 4.1.a.

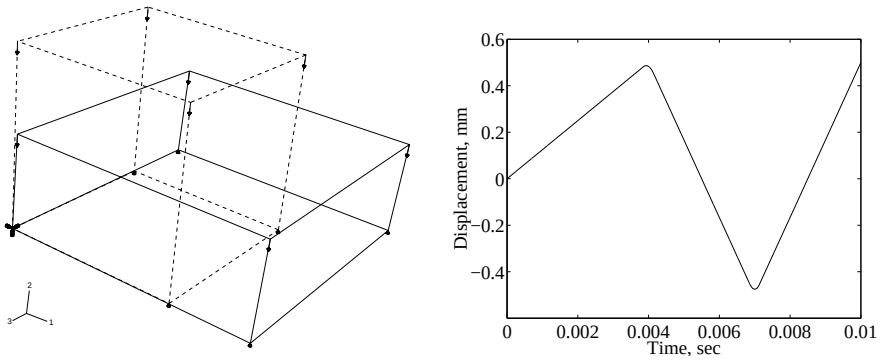

a. Initial and deformed meshes b. Applied displacement, $u_2(t)$

Figure 4.1: A single finite element model under alternating uniaxial tension and compression.

The vertical displacement of the four bottom nodes is zero and for the four top nodes it is described by the function $u_2(t)$ shown in Figure 4.1.b.

The material plastic properties are described by the power hardening law of the form:

$$\sigma_{\mathrm{Y}} = \sigma_{\mathrm{Y0}} \left(\epsilon^p_{eq} \frac{3G}{\sigma_{\mathrm{Y0}}} + 1 \right)^n \tag{4.1}$$

where σ_{Y0} is the first yield stress and n is the hardening exponent.

The simulation was performed at $T = 20°\mathrm{C}$. For this temperature the values $\sigma_{\mathrm{Y0}} = 447$ MPa and $n = 0.0575$ were chosen based on data shown in Figure 4.11. The Young's modulus and the Poisson ratio are $E = 2 \times 10^5$ MPa and $\nu = 0.3$ respectively. The hardening curve is shown in Figure 4.2.

A $5 \times 5 \times 5$ cell ductile ($M_D = 125$) and a $20 \times 20 \times 20$ cell brittle ($M_B = 8000$) CA array were created. Thus the ductile damage cell size is $L_D = 1/5 = 0.2$ mm and the brittle damage cell is $L_B = 1/20 = 0.05$ mm.

A two-parameter Weibull distribution was used to simulate the distribution of the initial void volume fraction, f_0. The shape parameter was taken as $W_\beta = 2$ and the scale parameter was taken as $W_\eta = 2.82 \times 10^{-4}$. The resulting histogram of f_0 is shown in Figure 4.3.

The fracture stress value, σ_{F}, was assigned to each brittle CA cell based on the normal distribution with $\bar{\sigma}_{\mathrm{F}} = 1.9 \times 10^3$ MPa and $\mathrm{STD}(\sigma_{\mathrm{F}}) = 3.6 \times 10^2$ Mpa. The resulting histogram of σ_{F} is shown in Figure 4.4.

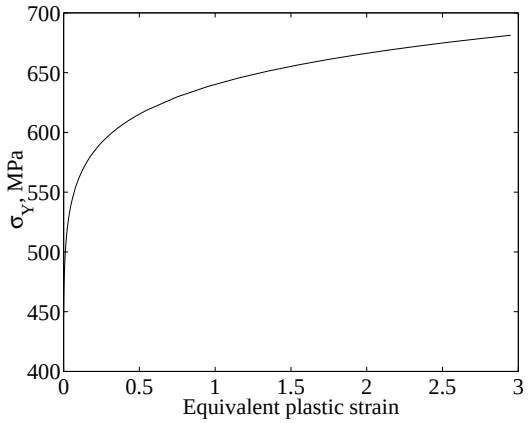

Figure 4.2: Yield stress, $\sigma_{\mathrm{Y}}(\epsilon^{p}_{eq})$.

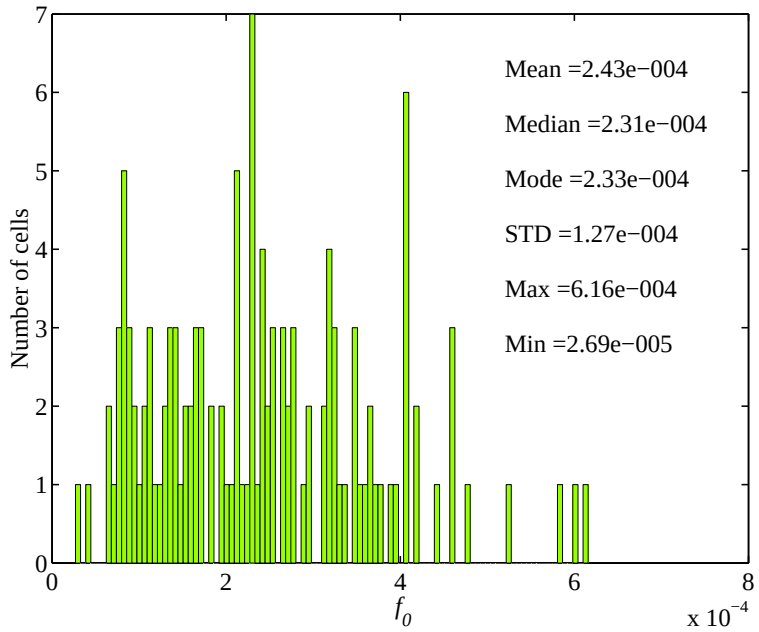

Figure 4.3: The initial void volume fraction histogram.

As this example does not simulate the behaviour of any particular steel, but rather illustrates the CAFE model behaviour, the actual numerical values of f_0 and σ_{F} assigned to each ductile or brittle cell are not very important, providing they lie within the reasonable ranges of these parameters for TMCR steels. Davis (2003) reported that no large second phase particles were observed in the fracture surfaces of the broken tensile and Charpy samples of a TMCR material

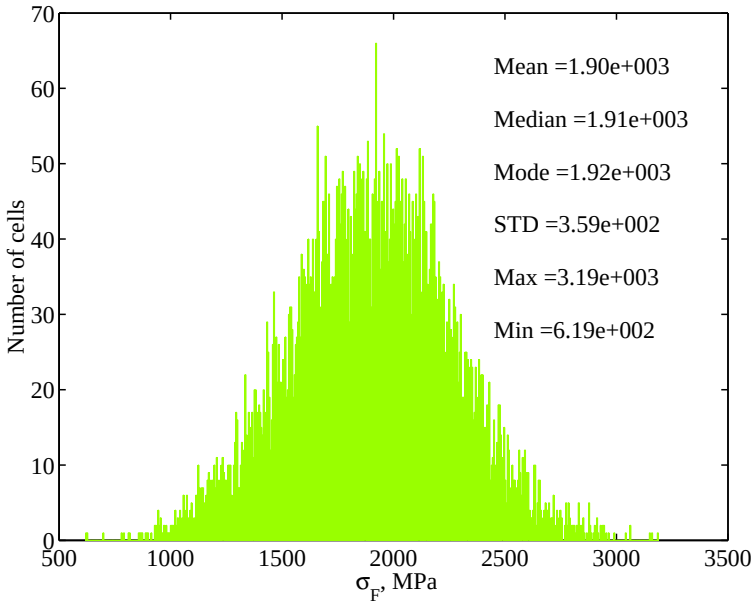

Figure 4.4: The fracture stress histogram.

described in section 4.1.3. However, if $f_0 = 0$, then the Rousselier model cannot simulate material softening, equations (B.1) – (B.7). Even if $f_0 \neq 0$ but very small, then the softening behaviour predicted by the model is too slow, and the strains to fracture are unrealistically high. Therefore the author had to choose a reasonable value of $\bar{f}_0$ based on his previous experience, and that of other people, of modelling ductile fracture (Shterenlikht et al., 2003; Andrews et al., 2002; Burstow, 1998)

To further simplify this example no grain size, d_g, or grain orientation, α, distribution is used. Also for reasons of simplicity $\eta = 1$, so that brittle fracture can initiate at any brittle CA cell.

The values for other model parameters used in this example (section 3.5) are $c_D = 1.4$, $c_B = 1.6$, $X^{max}_{(D)} = M_D^{2/3}$ and $X^{max}_{(B)} = M_B^{2/3}$.

There is little guidance as to how to choose the values for the above four parameters. We can assume that $c_B > c_D$ as the strain concentration ahead of a crack is higher than at the surface of a void. On the other hand $M^{2/3}$ is the number of cells in a square section of a cubic CA array. So $X^{max} = M^{2/3}$ is chosen on the assumption that a FE will fail when a planar crack, perpendicular to one of the three basis directions, crosses either of the two CA arrays.

The parameters of the Rousselier damage model (section 2.1.6) are: $D = 3$, $\sigma_1 = 500$ MPa and $\beta_F = 8$. These parameters are tuned on the CAFE modelling of the Charpy test at the upper shelf (section 4.1.3).

The computation of this example took less than 10 minutes.

The modelling results are shown in Figures 4.5 – 4.9. Of these Figures 4.5 – 4.7 present results on the macro (FE) scale. The micro (CA) scale outcome of the simulation is shown in Figures 4.8 and 4.9.

Figure 4.5.a shows the vertical stress against time, $\sigma_{22}(t)$. It is easy to see that the failure of the finite element occurred before the second change of the direction of applied displacement (Figure 4.1.b). Accordingly the shape of the finite element at the end of the simulation is that of a compressed element, as shown in Figure 4.1.a (solid lines).

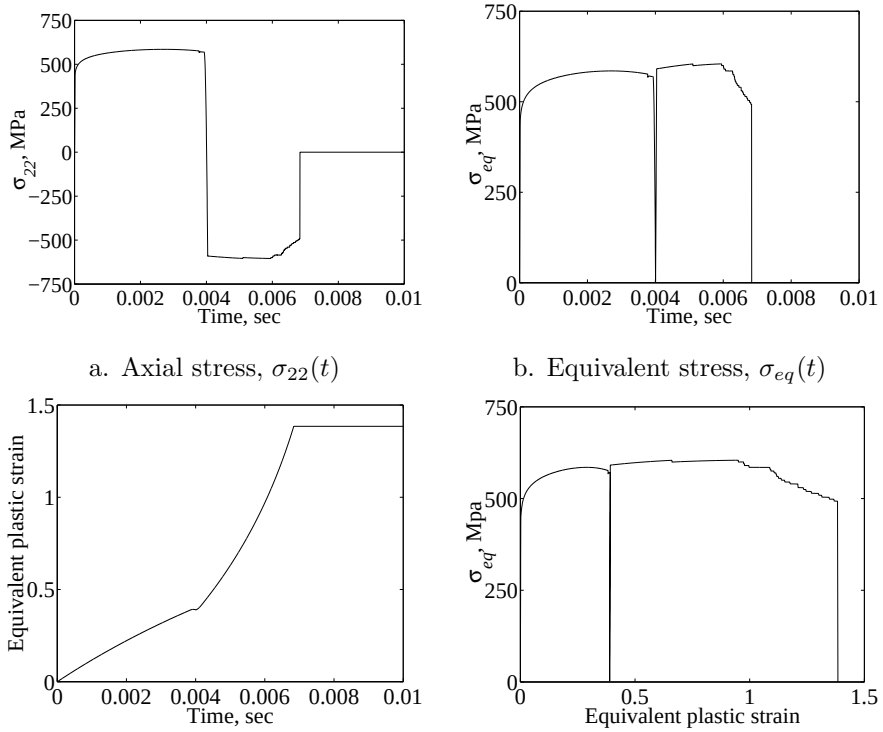

a. Axial stress, $\sigma_{22}(t)$

b. Equivalent stress, $\sigma_{eq}(t)$

c. Equivalent plastic strain, $\epsilon^p_{eq}(t)$

d. Equivalent stress, $\sigma_{eq}(\epsilon^p_{eq})$

Figure 4.5: A single finite element model under alternating uniaxial tension and compression.

The plot of von Mises equivalent stress against time, $\sigma_{eq}(t)$, is shown in

Figure 4.5.b. Two points worth noting are the time delay at $t = 4 \times 10^{-3}$ sec associated with elastic unloading and loading in the opposite direction, and the difference in the maximum σ_{eq} values in tension and compression. The maximum σ_{eq} in tension and compression are 585 MPa and 604 MPa respectively. This difference is due to the Rousselier model depending on the sign of the mean stress, σ_m (equation (2.16), section 2.1.6). This property of the Rousselier model is in a good agreement with various experimental observations that the positive σ_m values cause much greater damage than negative values (e.g. Bridgman, 1952).

Elastic unloading and loading can be seen also in the plot of equivalent plastic strain against time, $\epsilon^p_{eq}(t)$, shown in Figure 4.5.c.

The equivalent plastic strain – equivalent stress plot, $\sigma_{eq}(\epsilon^p_{eq})$, is shown in Figure 4.5.d. It is easy to see, by comparing this plot with that of $\sigma_{eq}(t)$ shown in Figure 4.5.b, that damage indeed accumulates much slower (in terms of ϵ^p_{eq}) in compression than in tension. For $\Delta\epsilon^p_{eq} = 0.6$, from $\epsilon^p_{eq} = 0.4$ to $\epsilon^p_{eq} \approx 1$, σ_{eq} remains virtually constant thus indicating that there is no loss of load bearing capacity during this large strain increment.

The evolution of three finite element solution-dependent state variables, Y_1, Y_2 and Y_3 is shown in Figures 4.6 and 4.7.

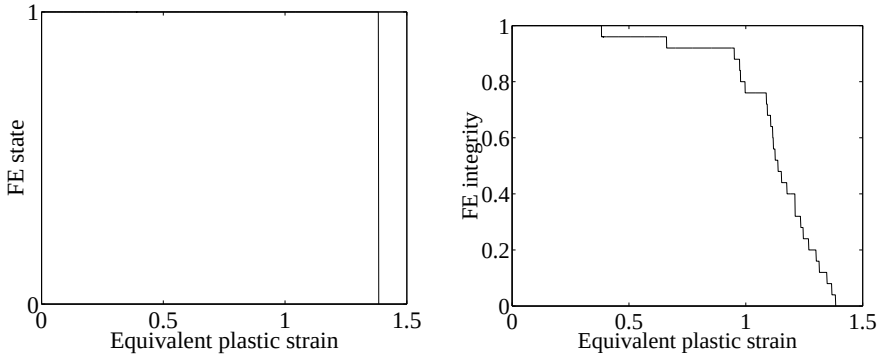

a. FE state, $Y_1(\epsilon^p_{eq})$ b. FE integrity, $Y_2(\epsilon^p_{eq})$

Figure 4.6: A single finite element model under alternating uniaxial tension and compression.

The state of the finite element, Y_1, changed from *alive* (1) to *dead* (0) at the moment when its integrity, Y_2, reached zero (Figures 4.6.a and 4.6.b). Each

step in Figure 4.6.b is associated with the failure of one or more cells in either of the CA arrays. These steps are also visible in Figures 4.5.a, 4.5.b and 4.5.d.

The evolution of the brittle phase per FE, Y_3, is shown in Figure 4.7. It is important to note that the brittle phase can decrease during the simulation according to equation 3.17. This is what happened in the present example. The brittle phase in the end of the analysis is only $Y_3 = 6.25 \times 10^{-4}$ or 0.06%. In practise such fracture would be routinely called a 100% ductile.

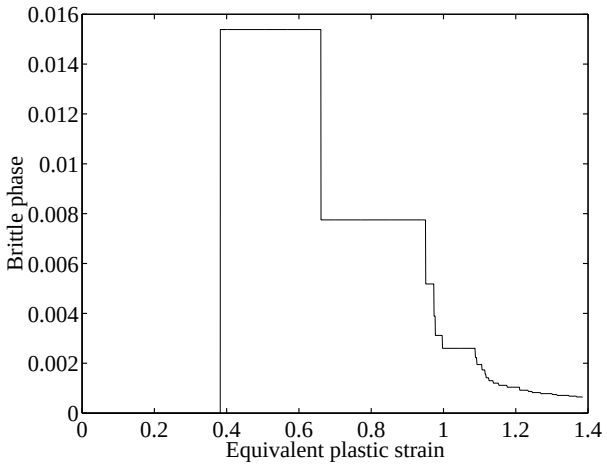

Figure 4.7: Brittle phase per FE, $Y_3(\epsilon^p_{eq})$.

The state of the brittle CA array at the end of the simulation is shown in Figure 4.8. As was said in section 3.4 the visualisation of the fracture on a CA scale in the present model is only possible in the initial (undeformed) configuration. Therefore the bounding box in Figure 4.8 represents the initial shape of the finite element.

All results on the CA scale in this and the following examples were generated with the `EnSight` visualisation software (CEI, 2002).

All *aliveC* cells are transparent and only the *deadB* (black) and *deadD* (grey) cells are shown. In fact there is only one *deadB* cell and all other dead cells are *deadD*. All *deadD* cells are grouped in $4 \times 4 \times 4 = 64$ cell cubes because there are 64 brittle CA cells per each ductile cell ($M_B/M_D = 8000/125 = 64$).

There is a tendency for the dead ductile cells to form clusters in XZ planes, which are the planes perpendicular to the direction of the maximum principal stress. However this tendency is quite weak and can only be seem in the bottom

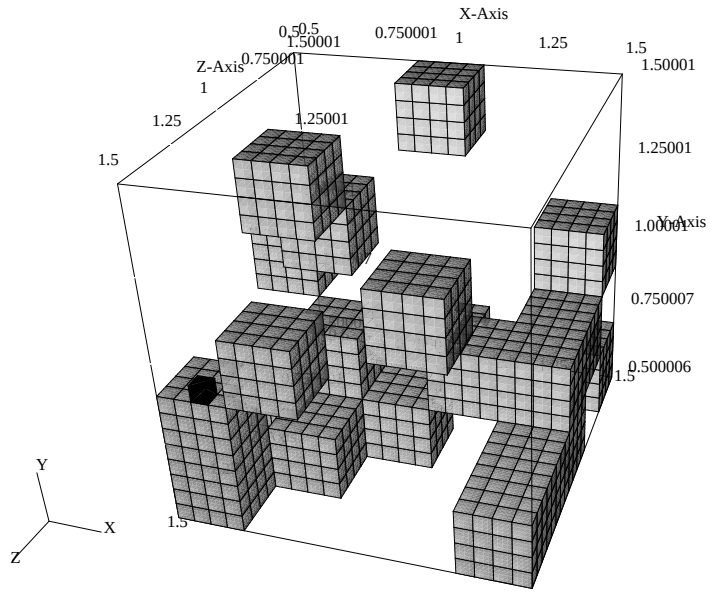

Figure 4.8: The state of the brittle CA array at the end of the simulation, $\epsilon^p_{eq} = 1.38$. Grey cells are $\Upsilon_{m(B)} = deadD$ and black cells are $\Upsilon_{m(B)} = deadB$.

layer of the dead ductile cells. This suggests that the concentration factor for the ductile CA array, $c_D = 1.4$, used in this analysis is not high enough.

On the other hand there is experimental evidence that there might be many voids in the vicinity of the main ductile crack which never coalesce with other voids or with the main crack (Puttick, 1959). Taking these observations into account the simulation result shown in Figure 4.8 seems reasonable.

The sequence of eight snapshots of the brittle CA array throughout the simulation is shown in Figure 4.9.

The fracture process started at $\epsilon^p_{eq} = 0.38$ when one ductile CA cell became dead. Mapping function $\mathbb{M}_{D\rightarrow B}$ (Step 6, page 49) then translated the location of this cell into the locations of the corresponding 64 brittle cells which became *deadD*. These cells constitute the grey block in Figure 4.9.b. Figure 4.10 shows another projection of the same state of the brittle CA array as Figure 4.9.b. The locations of the *deadD* cells are more clear in Figure 4.10. There are $4 \times 4 \times 5 = 80$ cells adjacent to the *deadD* cells which lie on the XZ planes. These are the cells which satisfy the condition of equation (3.28), i.e. these cells will be given the maximum principal stress higher than the value for the

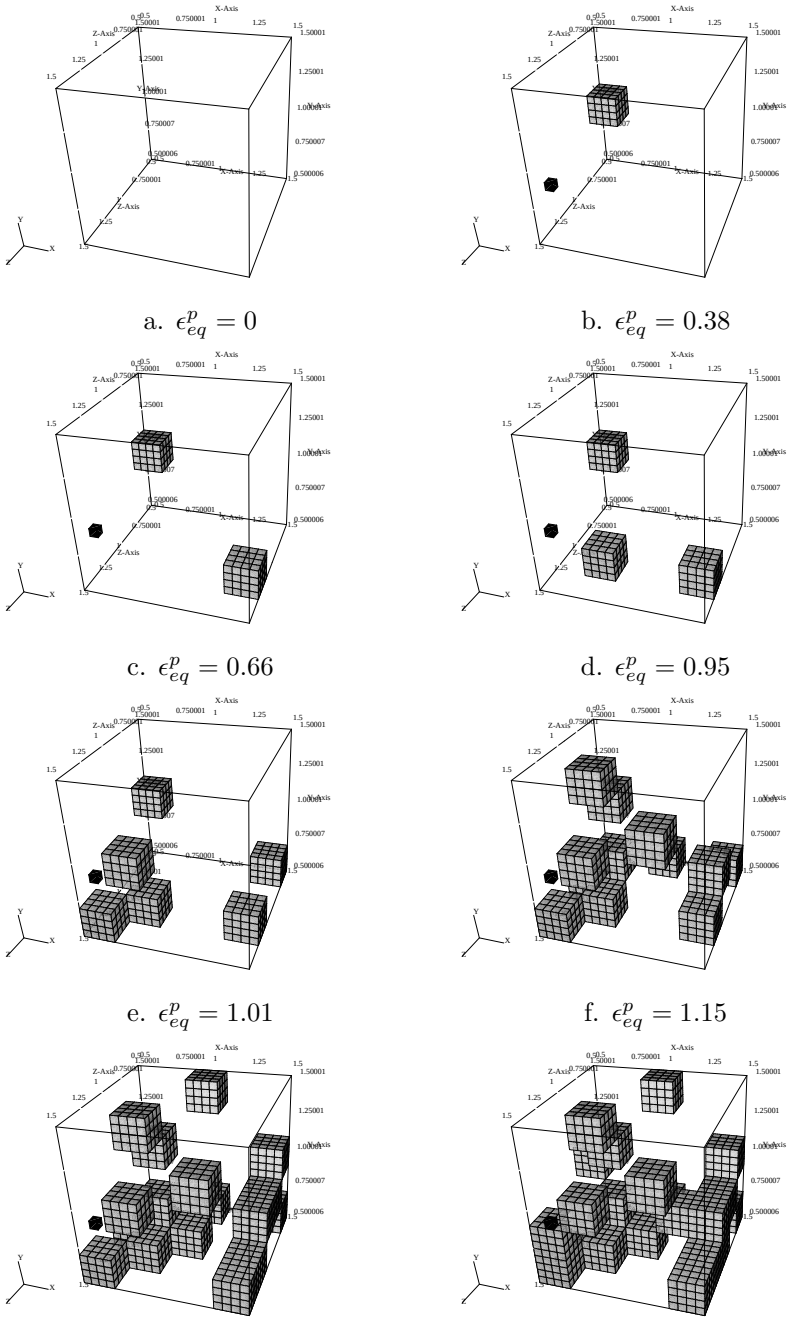

a. $\epsilon^p_{eq} = 0$ b. $\epsilon^p_{eq} = 0.38$

c. $\epsilon^p_{eq} = 0.66$ d. $\epsilon^p_{eq} = 0.95$

e. $\epsilon^p_{eq} = 1.01$ f. $\epsilon^p_{eq} = 1.15$

g. $\epsilon^p_{eq} = 1.25$ h. $\epsilon^p_{eq} = 1.38$

Figure 4.9: Damage propagation across the FE.

finite element integration point, $\sigma^l_{\mathrm{I}}(t_i) = c_D \cdot \sigma_{\mathrm{I}}(t_i)$. Because of the self-closing boundary condition (Figure 3.2, page 40) the black cell in Figure 4.10 is one of

these cells.

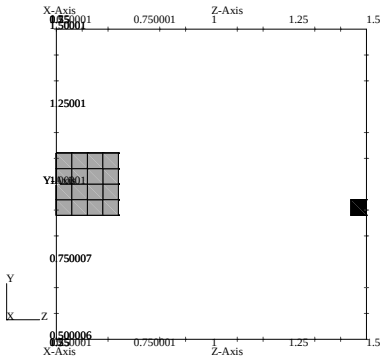

Figure 4.10: The state of the brittle CA array at $\epsilon^p_{eq} = 0.38$.

At $\epsilon^p_{eq} = 0.38$, $\sigma_{\rm I} = 576$ MPa, (in this example $\sigma_{\rm I} = \sigma_{22}$, Figure 4.5.a) therefore $\sigma^l_{\rm I} = 1.4 \times 576 = 806$ MPa. The data from Figure 4.4 shows that there only 5 brittle CA cells with $\sigma_{\rm F} \leq 806$ MPa. Accidentally one of these five happened to be the black cell in Figure 4.10. So this cell became *deadB* in the same time increment as the first ductile cell became dead. Accordingly the brittle phase at this moment was $1/64 = 0.0156$ (Figure 4.7).

The data for $\sigma_{\rm F}$ (Figure 4.4) and $\sigma_{22} = \sigma_{\rm I}$ (Figure 4.5.a) help to explain why there is only one *deadB* brittle CA cell at the end of the simulation.

The maximum $\sigma_{\rm I}$ in the analysis is $\sigma_{\rm I} = 604$ (Figure 4.5.a). Therefore the maximum $\sigma^l_{\rm I}$ is $\sigma^l_{\rm I} = 1.4 \times 604 = 845$ MPa. However Figure 4.4 shows that there are only 7 brittle CA cells with $\sigma_{\rm F} \leq 845$ MPa. Thus the probability that $max(\sigma^m_{\rm I}) \geq \sigma_{\rm F}$ for a brittle CA cell m is only $7/8000 = 8.75 \times 10^{-4}$.

The above discussion reveals the importance of the whole fracture stress distribution rather than its single characteristics (mean, median or mode) in transitional ductile – brittle fractures. It shows that transitional behaviour is only possible if there is a reasonable scatter of the fracture stress values. If there is no scatter and all brittle CA cells receive the same fracture stress, then the resulting fracture will be either 100% brittle or 100% ductile, because all brittle CA cells will behave as one.

The importance of the fracture stress is one of the major issues of the present work and it will be illustrated in greater detail in the next examples.

4.1.2 Single FE, forward tension – simulation of scatter

In this example the capacity of the full CAFE model to simulate the scatter at the transitional temperatures is illustrated. Similarly to the previous example (section 4.1.1), material properties were chosen to qualitatively reproduce fracture propagation in a TMCR steel.

The model consists of a single cubic 1mm × 1mm × 1mm finite element (Figure 4.1, dashed lines) under uniaxial tension.

The power hardening law of equation (4.1) was used. The first yield stress, σ_{Y0}, and the hardening exponent, n, are temperature-dependent as shown in Figure 4.11.

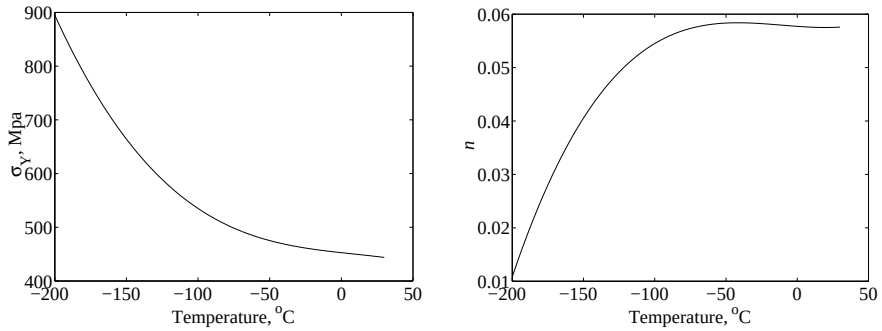

a. First yield stress, $\sigma_{Y0}(T)$ b. Hardening exponent, $n(T)$

Figure 4.11: Temperature dependence of material properties. Based on the experimental data provided by Davis (2003).

As in the previous example (section 4.1.1) $E = 2 \times 10^5$ MPa and $\nu = 0.3$.

A $5 \times 5 \times 5$ cell ductile ($M_D = 125$) and a $10 \times 10 \times 10$ cell brittle ($M_B = 1000$) CA array were created. Thus the ductile damage cell size is $L_D = 1/5 = 0.2$ mm and the brittle damage cell is $L_B = 1/10 = 0.1$ mm.

As in the previous example a two-parameter Weibull distribution was used to simulate the distribution of the initial void volume fraction, f_0. The shape parameter was taken as $W_\beta = 2$ and the scale parameter was taken as $W_\eta = 2.82 \times 10^{-4}$. The resulting histogram of f_0 in each of the simulations of this example was similar to that shown in Figure 4.3.

The fracture stress value, σ_F, was assigned to each brittle CA cell based on the normal distribution with $\bar{\sigma}_F = 1.9 \times 10^3$ MPa and $\mathrm{STD}(\sigma_F) = 5 \times 10^2$ MPa.

An example of the resulting histogram of σ_{F} is shown in Figure 4.12.

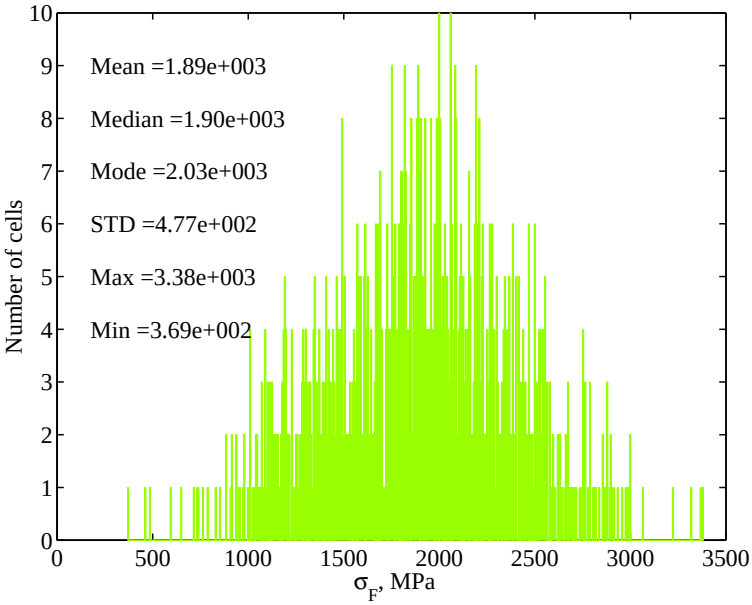

Figure 4.12: The fracture stress histogram.

The values for other model parameters are $\eta = 1$, $c_D = 1.4$, $c_B = 1.7$, $X^{max}_{(D)} = M^{2/3}_D$ and $X^{max}_{(B)} = M^{2/3}_B$. As in the previous example the parameters of the Rousselier damage model are $D = 3$, $\sigma_1 = 500$ MPa and $\beta_{\mathrm{F}} = 8$.

The simulations were performed at six temperatures, from $T = -196°\mathrm{C}$ to $T = 0°\mathrm{C}$, three runs at each temperature.

All simulations of this example took less than 4 minutes.

The modelling results are shown in Figures 4.13 – 4.17. Of these, Figures 4.13 – 4.16 present results on the macro (FE) scale. The micro (CA) scale results of the simulations are shown in Figure 4.17.

Figure 4.13 shows the evolution of the equivalent plastic stress, $\sigma_{eq}(\epsilon^p_{eq})$, during the simulation for all 18 runs.

The scatter of ϵ^p_{eq} to failure is very low at $-196°\mathrm{C}$, higher at $-175°\mathrm{C}$, the highest at $-150°\mathrm{C}$, lower at $-100°\mathrm{C}$ and very low again at $-50°\mathrm{C}$ and at $0°\mathrm{C}$. This Figure 4.13 demonstrates that the full CAFE model can generate the scatter in terms of ϵ^p_{eq} to failure. And the level of this scatter is temperature-dependent.

Figures 4.14 and 4.15 show the evolution curves of two of the FE solution-

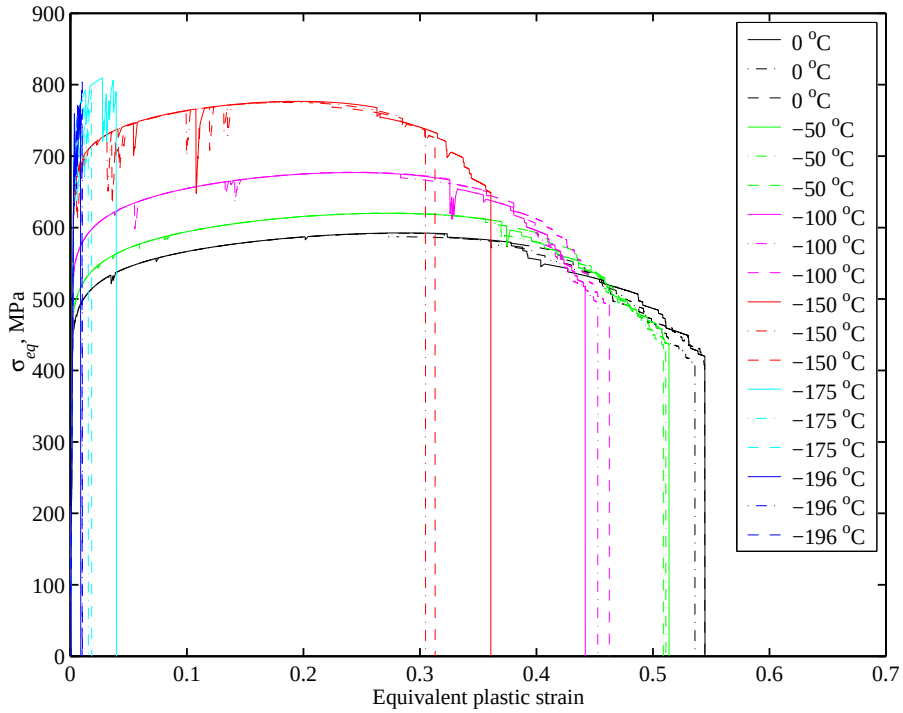

Figure 4.13: Equivalent von Mises stress, $\sigma_{eq}(\epsilon^p_{eq})$.

dependent variables: integrity, $Y_2(\epsilon^p_{eq})$, and the brittle phase, $Y_3(\epsilon^p_{eq})$.

It is easy to see in Figure 4.14 that the diversity of the shapes of the three $Y_2(\epsilon^p_{eq})$ curves at each temperature is maximal at -150°C and decreasing towards -196°C and towards 0°C. The three $Y_2(\epsilon^p_{eq})$ curves at -196°C (dark blue) lie virtually on top of each other. However the three curves at 0°C (black) can be easily distinguished one from another. Thus the scatter in terms of $Y_2(\epsilon^p_{eq})$ is also temperature-dependent.

Figure 4.15 shows the evolution of the fraction of the brittle phase per FE during the simulation, $Y_3(\epsilon^p_{eq})$. The curves at -196°C and at -175°C (dark and light blue) are not visible because in all six simulations $Y_3 = 1$ from the onset of the fracture propagation until the failure of the FE (compare with Figures 4.13 and 4.14).

The scatter in terms of the difference in curve shapes at each temperature is temperature-dependent. The six curves, three at -196°C and three at -175°C, lie on top of each other. However for all other temperatures the shapes the

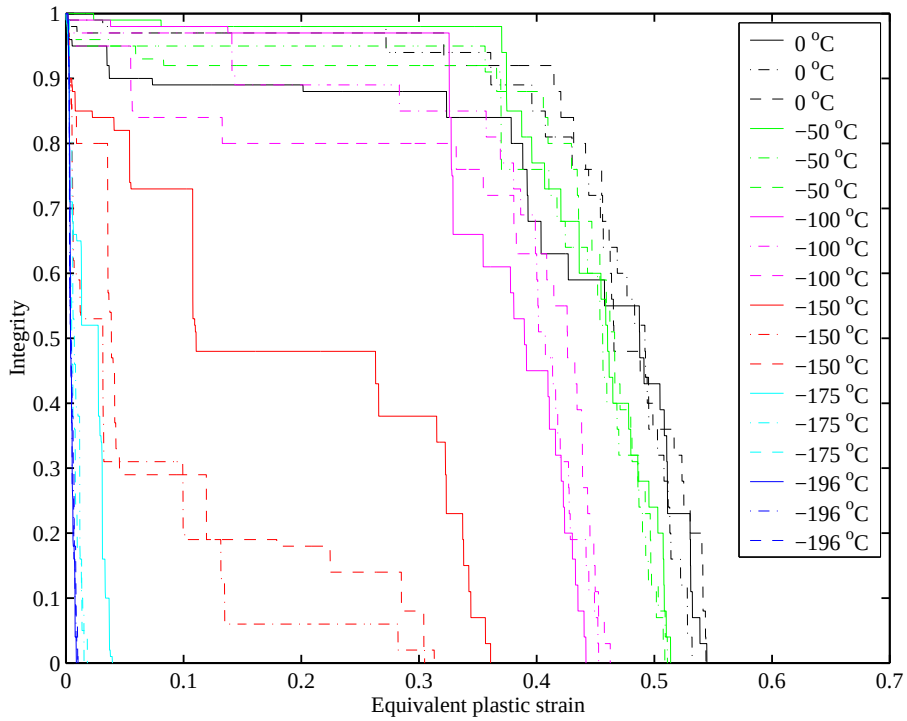

Figure 4.14: FE integrity, $Y_2(\epsilon^p_{eq})$.

curves are distinctly different.

The values of the brittle phase at the point of a FE failure are not very clear from Figure 4.15. They are shown separately in Figure 4.16 which is a typical illustration of the transitional ductile – brittle fracture behaviour.

In this example the lower shelf temperatures are below -175°C, the upper shelf is above -50°C and the transitional temperatures are from -150°C to -100°C. The level of scatter in the transitional region is higher than in the lower or in the upper shelf. It is interesting to note that the transition from the lower shelf is quite sharp, whereas the transition from the upper shelf is much smoother.

As in the example of section 4.1.1 the results of this section are rather qualitative than quantitative. Although the model is very capable of simulating the transitional behaviour, the transitional temperature range might be shifted from that obtained experimentally. This is primarily due to difficulties of finding the proper values for c_D, c_B, $X^{max}_{(D)}$, $X^{max}_{(B)}$, W_β and W_η (for the distribution of f_0)

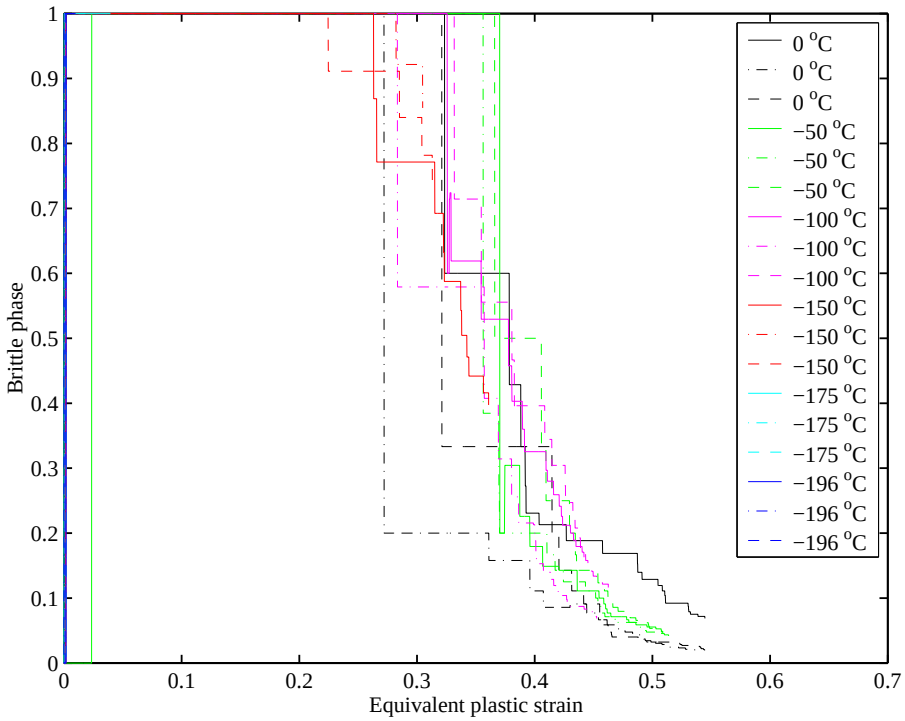

Figure 4.15: Brittle phase per FE, $Y_3(\epsilon^p_{eq})$.

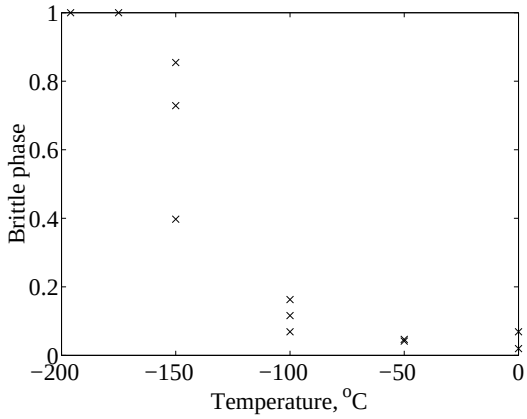

Figure 4.16: The fraction of the brittle phase at the end of the simulation.

and STD(σ_F). This issue is discussed in greater detail in section 4.2.1. On the other hand there is no necking in a single FE model. Therefore the stress triaxiality in this and the previous examples is very low, unlike in any real fracture test.

Figure 4.17 shows the state of the brittle CA array at the point of FE failure at six temperatures. The results of two of the three simulations at each temperature are shown. As in Figures 4.8 and 4.9 the black cells are *deadB* and the grey ones are *deadD*. In this example each ductile cell occupies the space of $2 \times 2 \times 2 = 8$ brittle cells since $M_B/M_D = 1000/125 = 8$.

A major brittle fracture plane is obvious at -196°C (Figures 4.17.a and 4.17.a) and at -175°C (Figures 4.17.c and 4.17.d). However in all four cases there are several *deadB* cells apart from the main crack. These cells represent

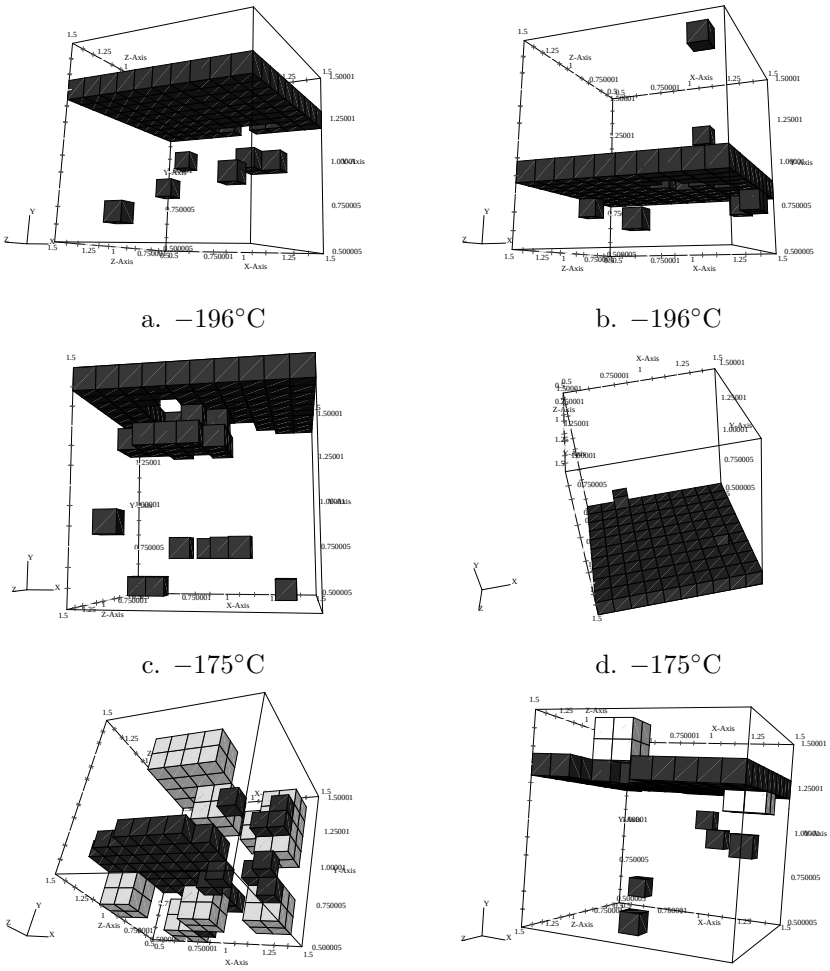

a. -196°C b. -196°C

c. -175°C d. -175°C

e. -150°C f. -150°C

Figure 4.17: Damage propagation across the FE. Grey cells are $\Upsilon_{m(B)} = deadD$ and black cells are $\Upsilon_{m(B)} = deadB$. (Continued on the next page).

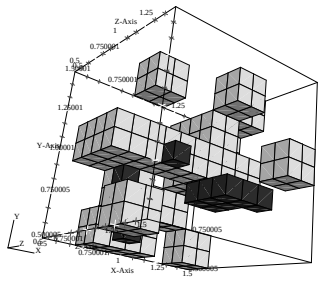

g. $-100°C$

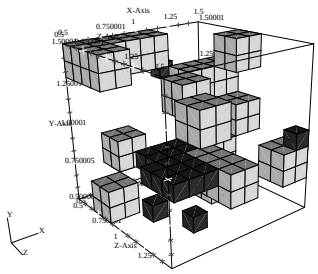

h. $-100°C$

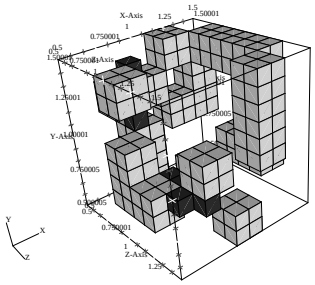

i. $-50°C$

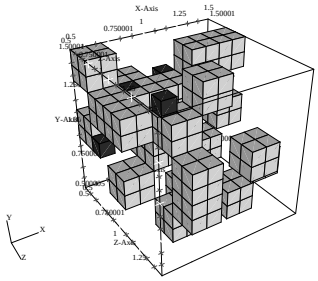

j. $-50°C$

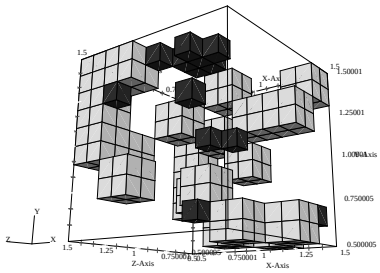

k. $0°C$

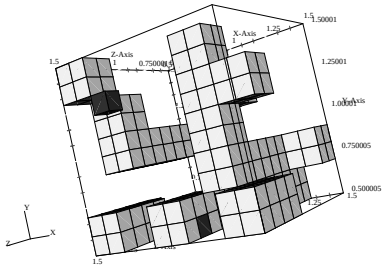

l. $0°C$

Figure 4.17: *Continued.*

the microcracks which were arrested due to a drop of applied stress or due to a very high fracture stress in all neighbourhood grains (cells). These microcracks have been observed in experiments (Lin et al., 1987; Nohava et al., 2002). The overall similarity between these four brittle CA states is clear. That is what one would expect after seeing the results in Figures 4.13 – 4.16.

The two brittle CA states at $-150°C$ (Figures 4.17.e and 4.17.f) are quite different. There is a large brittle crack in Figure 4.17.e; however it did not cross the whole of the FE and the final failure was due to ductile fracture. In contrast, the brittle cleavage plane crossed virtually the whole of the FE in Figure 4.17.f

and only two ductile cells failed. Consequently the brittle phase for the state shown in Figure 4.17.e is $Y_3 = 0.4$ and for the state shown in Figure 4.17.f it is $Y_3 = 0.85$ (see Figure 4.16).

With temperatures increasing to $-100°C$ (Figures 4.17.g and 4.17.h), $-50°C$ (Figures 4.17.i and 4.17.j), and $0°C$ (Figures 4.17.k and 4.17.l), one can see an increasing number of *deadD* cells. The difference between the states at each temperature is insignificant.

Thus the results on the micro (CA) scale (Figure 4.17) are complementary to those of the macro (FE) scale (Figures 4.13 – 4.16).

Finally a special transition temperature diagram can be constructed by combining the data from Figures 4.11.a, 4.12, 4.13 and 4.16. This diagram is shown in Figure 4.18.

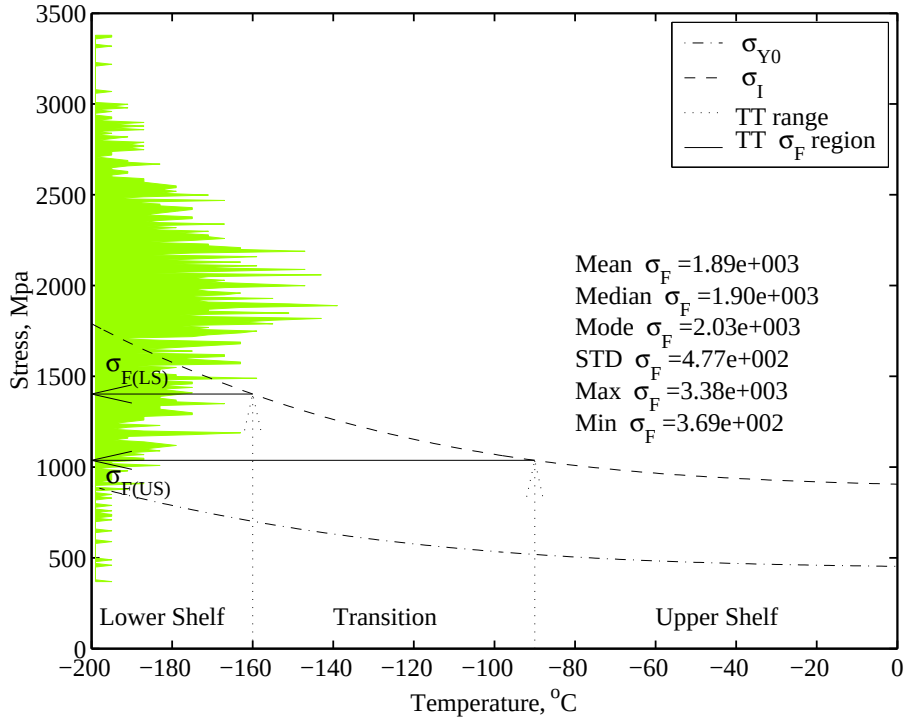

Figure 4.18: Transition temperature diagram.

This diagram illustrates schematically the influence of the fracture stress distribution on the transition temperature range.

The fracture stress distribution, assumed to be independent of temperature,

is shown on the left. The maximum principal stress line, $\sigma_{\mathrm{I}}(T)$, is drawn slightly higher than $c_B \times \sigma_{Y0}(T)$ because the data in Figure 4.13 shows that brittle fracture can happen after the onset of plasticity, so $\sigma_{\mathrm{I}} > \sigma_{Y0}$. The transition range obtained from Figure 4.16 is approximately from $-160°$C to $-90°$C. By establishing the intersection points of the transition temperature limits with the $\sigma_{\mathrm{I}}(T)$ curve, the transition temperature range of σ_{F} can be obtained: $\sigma_{\mathrm{F(US)}}$ and $\sigma_{\mathrm{F(LS)}}$.

The number of cells which have the fracture stress lower than the upper shelf limit, $\sigma_{\mathrm{F(US)}}$, is so small that it is very unlikely that many brittle cells m with $\sigma_{\mathrm{F}}^m < \sigma_{\mathrm{F(US)}}$ will be located near the fracture propagation path. Although some brittle cells with particularly low σ_{F} will still fracture even at the upper shelf temperatures (see e.g. Figures 4.17.i – 4.17.l), the number of these cells is so small that they do not affect the fracture process significantly.

On the other hand the lower shelf limit, $\sigma_{\mathrm{F(LS)}}$, is so high that it is very likely that many cells m with $\sigma_{\mathrm{F}}^m < \sigma_{\mathrm{F(LS)}}$ will be located near the fracture propagation path.

Thus the number of brittle cells which can fracture is inversely related to temperature in the transitional region but saturation is reached as temperature approaches either shelf.

At very low temperatures (the lower shelf) the number of brittle cells which can fail is so high that all but a few brittle cells located at the fracture propagation path will fail. Further decrease of temperature results in saturation and no significant change in fracture behaviour occurs. Similarly, at very high temperatures (the upper shelf) this number is so small that very few brittle cells will fail. For all practical purposes this is 100% ductile fracture. The saturation is thus reached and further increase of temperature does not change the picture. As both the upper and the lower shelves can be described as "saturation", the levels of scatter are small at these temperatures.

The fracture behaviour is different at transitional temperatures. The number of brittle cells which can fail is now temperature-dependent and the fracture propagation behaviour is affected by the locations of these cells as well as the total number of them. So there might be a situation when no suitable brittle cell is located at a point of highest macro (FE) stress. This will lead to further

increase of macroscopic stress until the brittle fracture criterion of equation (3.12) is met at a point where a suitable brittle cell is located. However, in the next simulation the locations of the brittle cells which could fail will be different and thus the whole of the fracture propagation path will change. This is the reason for the high scatter in the transitional temperature range.

The diagram in Figure 4.18 suggests that there are two important parameters of the fracture stress distribution, $\sigma_{\mathrm{F(LS)}}$ and $\sigma_{\mathrm{F(US)}}$. If we assume that these are true material parameters and that they do not change with temperature, then the diagram will indicate that the increase of the maximum principal stress, whether due to higher yield stress or due to high stress triaxiality, shifts the transition temperature range right, towards higher temperatures. There is some experimental evidence to support this point.

Results presented by Kohout (2001) show that the transition temperatures for V-notched Charpy samples are higher than for U-notched ones. This happens because the stresses below the V-notch are higher than below the U-notch.

Hertzberg reproduced results (Hertzberg, 1996, page 389) which show that the transition temperature range obtained in drop weight (DWTT) and in dynamic (DT) tear tests for A541 Class 6 steel is significantly higher than that recorded with the Charpy test. The reason is that DWTT and DT "may be considered to be oversized Charpy samples" (Hertzberg, 1996, page 387). As a consequence there is much higher stress triaxiality in DWTT and DT samples compared with the Charpy specimen.

Materials which exhibit elevation of the first yield stress with strain rate produce a transition temperature shift when tested at different strain rates. Results reproduced by Hertzberg for impact and slow-bend Charpy tests (Hertzberg, 1996, pages 392 and 393) show that the transition temperature range for the impact Charpy test is higher that for the slow-bend test.

The analysis of the diagram in Figure 4.18 has one very important conclusion. This is that the whole of the grain size distribution is necessary for proper simulation of the transitional fracture behaviour. If all grains have the same grain size, e.g. the mean grain size, then no transitional behaviour is possible, as the model will show that all cells fail in either ductile or brittle mode, depending on the simulation temperature.

Indeed the diagram of Figure 4.18 indicates that the higher the STD(σ_{F}), the wider is the transition temperature range. If STD(σ_{F}) is very small, then the values $\sigma_{\mathrm{F(LS)}}$ and $\sigma_{\mathrm{F(US)}}$ are very close and the transition range is very narrow. If STD(σ_{F})=0, which is the case of using a uniform grain size, then $\sigma_{\mathrm{F(LS)}} = \sigma_{\mathrm{F(US)}}$ and the width of the transitional region is zero. Effectively the model in that case can only simulate the upper or the lower shelf behaviour.

The grain size distribution has such an important role in this example because there are no explicit initiation sites of brittle fracture, or rather every cell is a potential initiation site as $\eta = 1$. However, if $\eta < 1$, as in the next two examples (sections 4.1.3 and 4.2.1), then the distribution of the initiation sites (fracture stress distribution of *aliveC* brittle cells) is a key factor affecting transitional behaviour.

4.1.3 The Charpy test

This example illustrates the simulation of the Charpy impact test with the use of the full CAFE model.

Figures 4.19 and 4.20 show the meshes of all bodies included in the model. These are the specimen, the anvils and the BS EN 10045-1 (1990) striker. Only the first 35 mm of the striker tup is modelled.

A 0.15 friction coefficient is adopted for all contact surfaces.

The full CAFE model is only used in the finite elements located near the anticipated fracture propagation path (damage zone). The damage zone consists of 900 `C3D8R` elements (HKS, 2001) which are shown in Figure 4.21. Majority of these are 1mm $\times$ 1mm $\times$ 1mm cubic elements. However slightly smaller elements are used near the root of the notch.

$5 \times 5 \times 5$ cell ductile ($M_D = 125$) and $10 \times 10 \times 10$ cell brittle ($M_B = 1000$) CA arrays were created for each finite element in the damage zone. Thus the ductile damage cell size is $L_D \approx 1/5 = 0.2$ mm and the brittle damage cell is $L_B \approx 1/10 = 0.1$ mm. The full CAFE model will therefore have 112500 ductile and 900000 brittle CA cells.

The material simulated in this example is a laboratory control rolled TMCR steel. The data for this steel is obtained from published papers and by private communication (Bhattacharjee and Davis, 2002; Bhattacharjee et al., 2003;

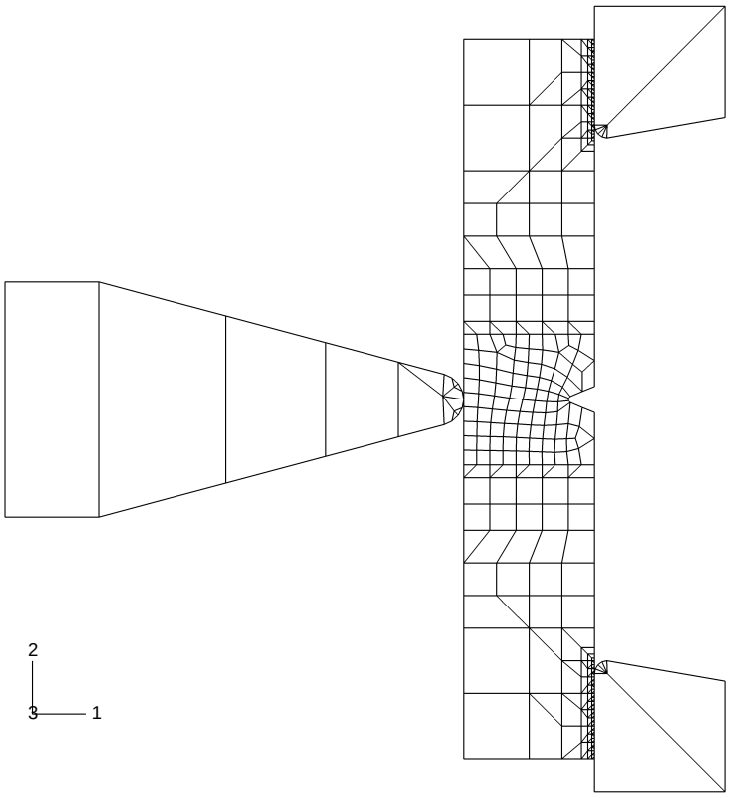

Figure 4.19: The finite element mesh of the Charpy specimen, the anvils and the striker.

Davis, 2003).

Figure 4.22 shows two typical illustrations of the brittle and the ductile fracture surfaces obtained on the present TMCR steel. The average spacing between the larger voids is approximately 100 micron. The average cleavage facet size is approximately 50 micron. Thus the damage cell sizes used in this example are roughly two times larger than the microstructural features to which they are usually related. This was a conscious decision aimed at cutting the simulation time. The author believes that such discrepancy can be dealt with appropriately by the present CAFE model, e.g. by assigning the fracture stress to each brittle cell based on the grain size distribution (section 3.2.2).

The chemical composition of this TMCR steel is shown in Table 4.1.

The rolling process starts at 1120°C from a 145 mm thick slab and includes

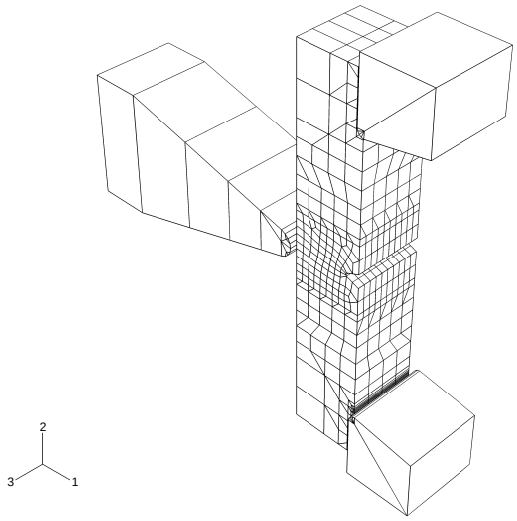

Figure 4.20: A three-dimensional view of the Charpy test model.

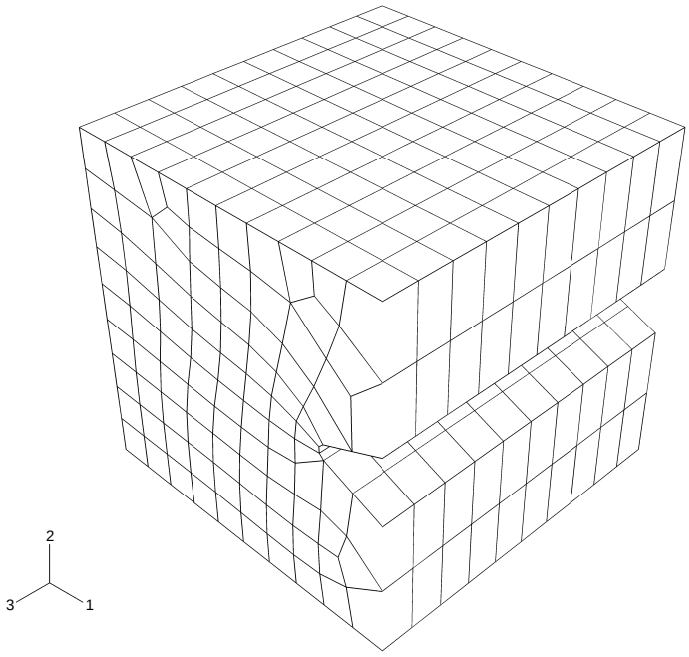

Figure 4.21: The mesh of the damage zone of the Charpy specimen containing 900 finite elements.

26 passes to a finish roll temperature of 717°C. The final slab thickness was approximately 30 mm. Figure 4.23 shows the microstructure of this steel at the

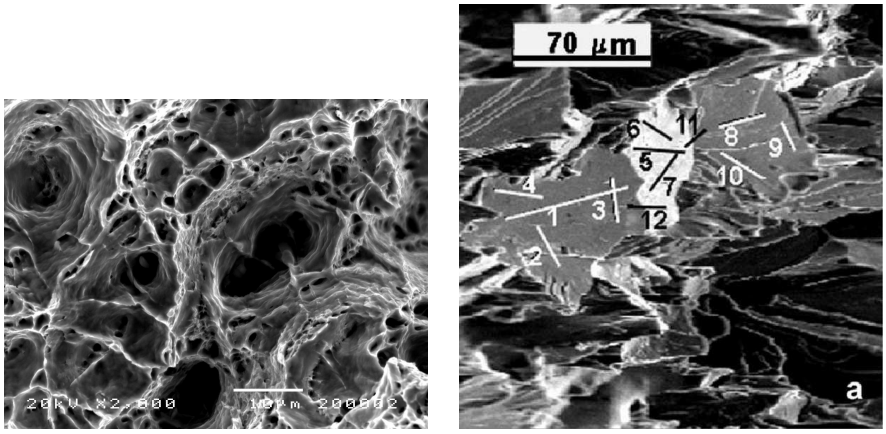

a. Ductile fracture b. Brittle fracture

Figure 4.22: Typical ductile and brittle fracture surfaces of this TMCR steel. Figure a. courtesy of Davis (2003), Figure b. is reproduced from Bhattacharjee and Davis (2002).

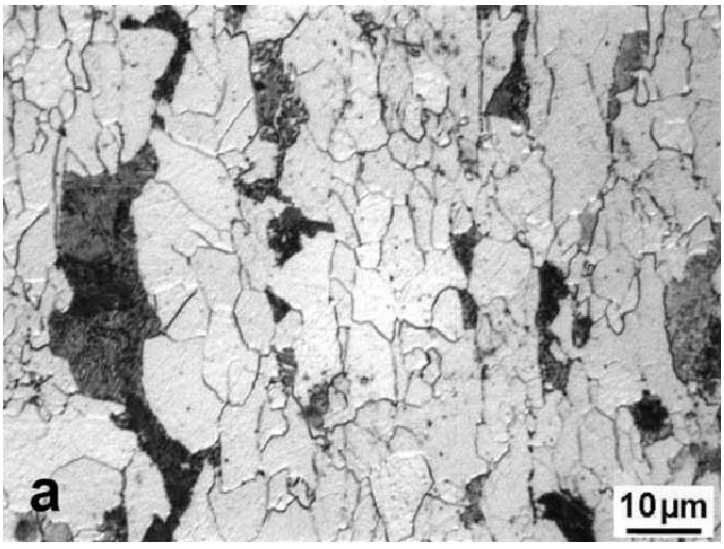

Figure 4.23: Microstructure of the TMCR steel. From Bhattacharjee and Davis (2002).

mid-thickness location, 15 mm below the surface. The grain size distribution at the mid-thickness plane is shown in Figure 4.24.

Figures 4.23 and 4.24 suggest a duplex distribution. There is an obvious drop in Figure 4.24 at $d_g \approx 1.1$ micron which separates the two parts of the

C	Si	Mn	P	S	Al	Nb	V
0.1	0.31	1.42	0.017	0.005	0.046	0.045	0.046

Table 4.1: Chemical composition of the TMCR steel used (weight %). From Bhattacharjee and Davis (2002).

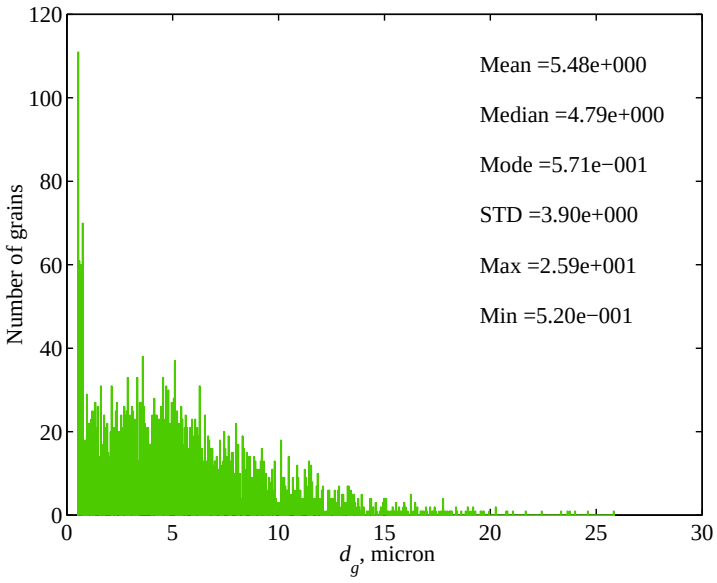

Figure 4.24: The 500-bin histogram of the grain size, d_g. Data courtesy of Davis (2003).

histogram. The two parts of the full histogram split at $d_g = 1.1$ micron are shown in Figures 4.25 and 4.26.

It must be said that Dr C Davis, who provided the raw grain size data used in the histogram shown in Figure 4.24, suggested that high number of grains with $d_g < 1$ micron might be a by-product of the measuring technique. However, it is not obvious what is the minimum reliable grain size (Davis, 2003). For this reason the grain size data was used in this example exactly as provided without any filtering. Moreover, as will be shown below, grains with $d_g \leq 1.1$ micron do not contribute to the fracture propagation due to very high fracture stresses. Nevertheless, this example demonstrates a useful technique for simulating duplex grain size distributions.

We shall approximate each part of the full histogram with a separate Weibull

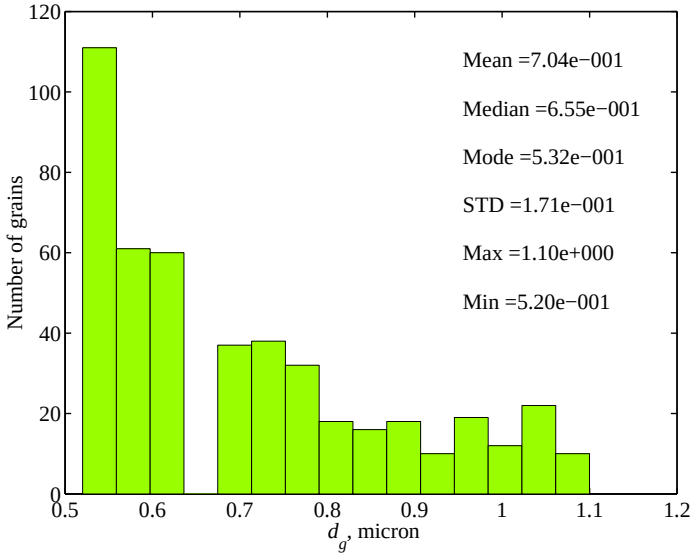

Figure 4.25: The 15-bin histogram of $d_g \leq 1.1$ micron.

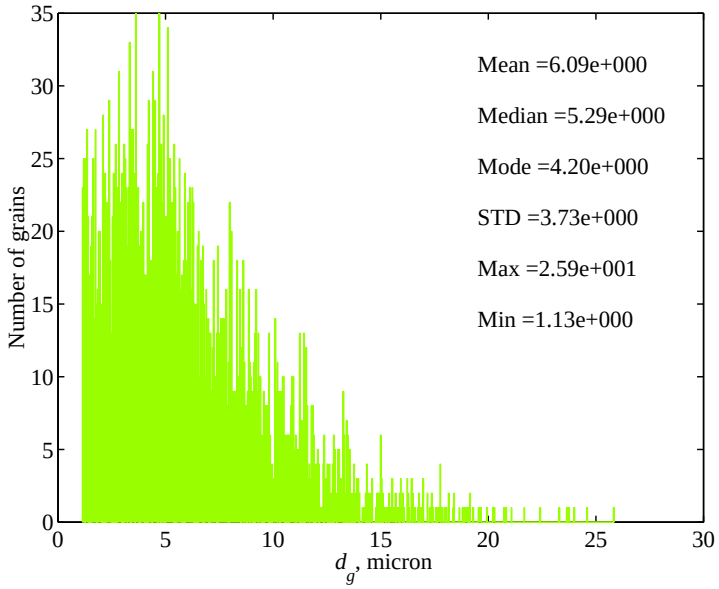

Figure 4.26: The 500-bin histogram of $d_g > 1.1$ micron.

distribution based on the mean and the standard deviation values of this part. The $d_g \leq 1.1$ micron part of the histogram (Figure 4.25) is simulated with a Weibull distribution with parameters $W_\beta = 1.065$, $W_\eta = 0.189$ and $W_\gamma = 0.52$ ("W_l distribution"). The $d_g > 1.1$ micron part of the histogram (Figure 4.26) is

simulated with a Weibull distribution with parameters $W_\beta = 1.298$, $W_\eta = 5.401$ and $W_\gamma = 1.1$ ("W_r distribution").

There are 4087 data points in the full histogram (Figure 4.24), 464 data points in the $d_g \leq 1.1$ micron histogram (Figure 4.25) and 3623 data points in the $d_g > 1.1$ micron histogram (Figure 4.26). Therefore the fraction of cells for which the grain size will be generated with the W_l distribution is $464/3623 = 0.128$. For the rest of the brittle cells the W_r distribution will be used.

The histogram of the brittle CA cell grain sizes generated with the W_l and the W_r distributions is shown in Figure 4.27.

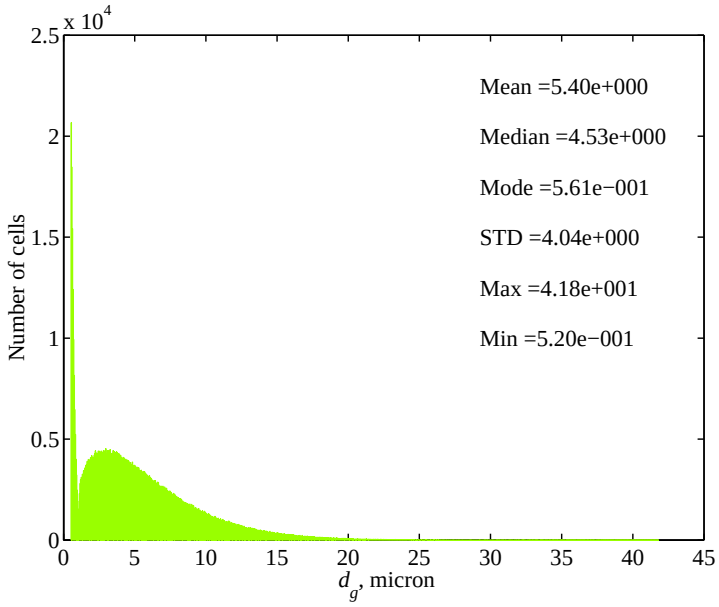

Figure 4.27: The 1000-bin histogram of the generated grain size.

It is much smoother that the experimentally obtained histogram shown in Figure 4.24. This is partly due to a much larger number of cells (900000) than the number of grains for which size was obtained experimentally (4087). On the other hand the Weibull distribution is only an approximation of the very complex experimental data. However, statistical characteristics of the histograms shown in Figures 4.24 and 4.27 are quite similar.

Wu and Davis (2003) reported an effective fracture surface energy of 52 J/m^2 for a TMCR steel very similar to that used in this work. This value agrees well with "typical" surface energy values (Lin et al., 1987).

Taking this value as the effective surface energy of a ferrite – ferrite interface, γ_{ff}, we can generate the fracture stress values using the grain size histogram (Figure 4.27) according to equation (2.26), page 28. The histogram of the generated brittle CA cell fracture stress is shown in Figure 4.28.

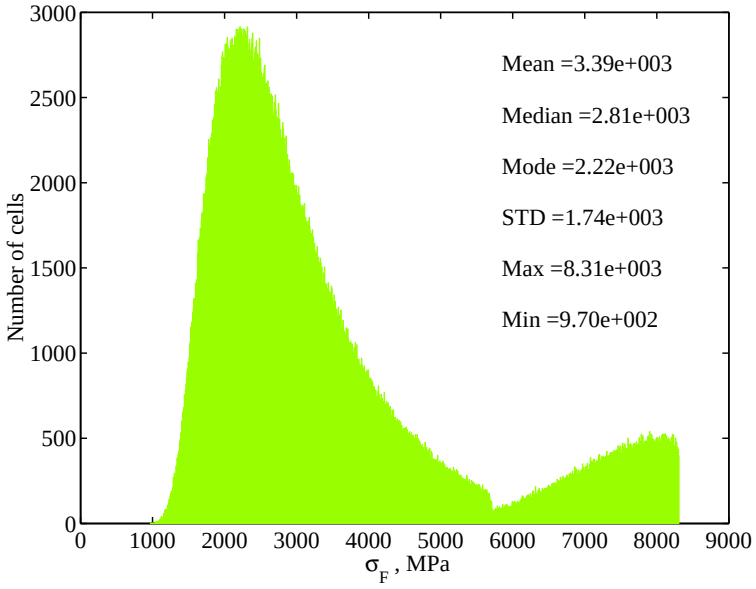

Figure 4.28: The 1000-bin histogram of the generated fracture stress, σ_{F}.

As in the example of section 4.1.1 a two-parameter Weibull probability density function was used to simulate the distribution of the initial void volume fraction, f_0. The shape parameter was taken as $W_\beta = 2$ and the scale parameter was taken as $W_\eta = 2.82 \times 10^{-4}$. The resulting histogram of f_0 is shown in Figure 4.29.

The value of the misorientation threshold, θ_{F}, is chosen based on the experimental data reported by Bhattacharjee and Davis (2002). The authors observed misorientation angles as high as 12° within a single cleavage facet. On the other hand the angles between the facets were reported in the range 17° – 45°. Accordingly $\theta_{\mathrm{F}} = 30°$ is used in this example.

The maximum possible misorientation angle for this steel is $\theta_{max} \approx 60°$ (Bhattacharjee and Davis, 2002; Bhattacharjee et al., 2003). Therefore the orientation angle, α, assigned to each brittle CA cell, is generated using a uniform distribution, $\alpha \in [0 \ldots \theta_{max}]$.

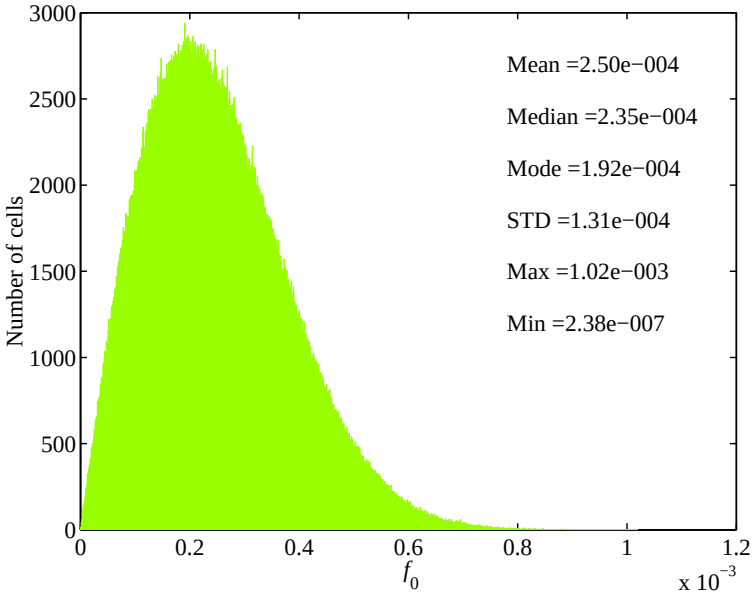

Figure 4.29: The initial void volume fraction histogram.

The value $\eta = 5 \times 10^{-3}$ is used in this example. So only $5 \times 10^{-3} \times 900000 = 4500$ randomly chosen brittle CA cells can initiate brittle fracture.

The values for other model parameters are $c_D = 1.4$, $c_B = 3$, $X_{(D)}^{max} = M_D^{2/3}$ and $X_{(B)}^{max} = M_B^{2/3}$.

As in the previous example the power hardening law of the form expressed by equation (4.1) was used. The temperature dependence of the first yield stress, σ_{Y0}, and the hardening exponent, n, for this TMCR steel is shown in Figure 4.11. Both curves are fitted over the data extracted from the tensile test results provided by Davis (2003).

One useful feature of the present CAFE models (both the full and the simplified) is that each fracture mechanism can be "switched" on and off according to user's wish. This feature is used in this example to tune the parameters of the Rousselier ductile damage model. By switching off the brittle failure we can ensure that all fractures will occur in the ductile CA array.

If both the brittle and the ductile fracture mechanisms are switched on then the running time of this example is about one week. If the brittle fracture is switched off then the running time can be cut roughly by a factor of three, to two – three days.

However, even two days is a long time for tuning as tens of runs might be necessary to find the best combination of modelling parameters. Accordingly a simplified tuning procedure was adopted in this example to cut the number of simulations (section 2.4). All three Rousselier model parameters, D, σ_1 and β_F, were tuned together. The tuning was aimed at achieving the total energy absorbed similar to that obtained in the Charpy test at the upper shelf temperatures.

A more thorough tuning could have been performed if experimental force – time Charpy data were available. This sort of data is usually obtained with the instrumented Charpy test (Shterenlikht et al., 2003). Unfortunately no such data were available for this steel.

The Charpy impact data from Bhattacharjee et al. (2003) shown in Figure 4.39 was used for tuning. The experimentally obtained upper shelf temperatures for this TMCR steel are $T \geq -20°C$ and the corresponding Charpy energy values are $C_v \approx 180J$ (Figure 4.39).

The best fitted values for the Rousselier model parameters are $D = 3$, $\sigma_1 = 500$ MPa and $\beta_F = 8$.

After the tuning the simulation of the Charpy test at $T = -50°C$ was performed. The simulation results on the macro (FE) scale are shown in Figures 4.30 and 4.31. Accordingly Figures 4.32 – 4.35 demonstrate results on the micro (CA) scale.

Figure 4.30.a shows the modelling force curve. As no instrumented Charpy test data were available for this TMCR steel, Figure 4.30.b shows a typical force curve obtained during the instrumented Charpy test on a TMCR steel different from the one used in the present work. This experimental data is courtesy of Davis (2003) and is given here only for qualitative comparison of force drop in the model and in the experiment. It is very likely that the experimental force curve obtained on the TMCR steel used in this example would exhibit a similar drop to that shown in Figure 4.30.b.

It is easy to see that brittle fracture propagates slower in the model than in the experiment. Brittle fracture propagation can be easily identified in the experimental force curve (Figure 4.30.b) as an instantaneous drop of force from the maximum value to almost zero. The model, however, exhibits a more gradual

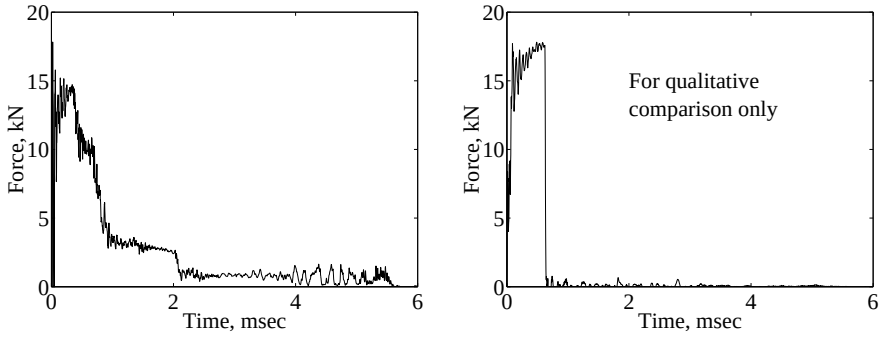

a. Simulation b. A typical experiment

Figure 4.30: Modelling ($T = -50°$C) and experimental ($T = -60°$) Charpy force curves. Experimental data obtained on a different TMCR steel is courtesy of Davis (2003).

reduction in force.

The present CAFE model cannot simulate a sharp drop of force because the fracture cannot propagate from one finite element into another. This is a limitation imposed by the organisation of the `Abaqus` code (section 5.1). Thus brittle fracture must reinitiate in each finite element (each brittle CA) in the fracture propagation path which results in a more gradual brittle fracture propagation process.

The total energy absorbed predicted by the model is 89J. The energies obtained in the experiment (Figure 4.39) at this temperature range from 117J to 142J. Therefore the full CAFE model probably underpredicts the total energy absorbed at $T = -50°$C. However, at least three simulations have to be performed before some indication of the scatter of simulated energy values can be obtained. Because of the long running times it was not feasible to do this with the full CAFE model.

A deformed mesh at the end of the simulation is shown in Figure 4.31. The failed FEs are removed from the mesh.

The visualisation of results on the micro (CA) scale is not straightforward because all CAs are cubic but some FEs are not. To avoid the overlapping of the CA blocks during visualisation they are shown shrunk. However the position and the size of each CA is related to the position and size of the corresponding FE. This technique is illustrated in Figure 4.32. The brittle CA arrays are used

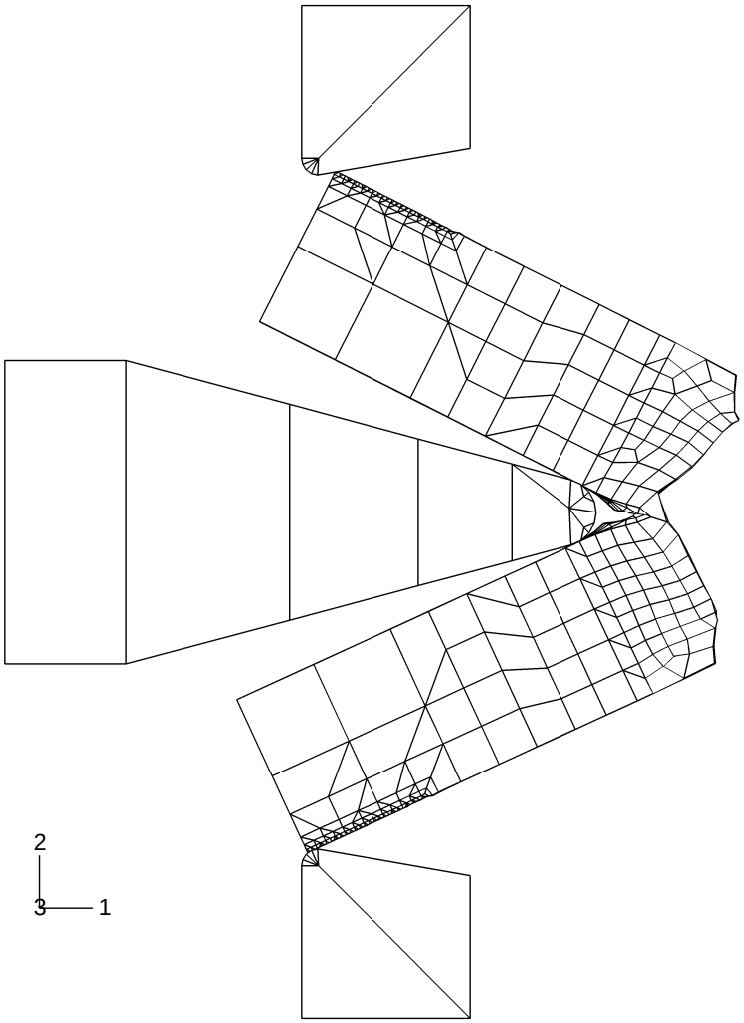

Figure 4.31: Deformed FE mesh of the Charpy test simulation at $T = -50°\text{C}$.

for visualisation in this example.

Figure 4.33 shows all 4500 *AliveC* brittle cells generated for this example. Only these cells can initiate the brittle fracture.

Fracture propagation on the CA scale is shown in Figure 4.34. Only *DeadB* (black) and *DeadD* (green) cells are shown. So the brittle fracture areas are black and green areas represent the ductile fracture. Fracture propagates on the XZ plane along direction X.

Fracture starts in the ductile mode. However several small brittle cracks are also visible in Figures 4.34.a and 4.34.b. It is easy to see that the fracture

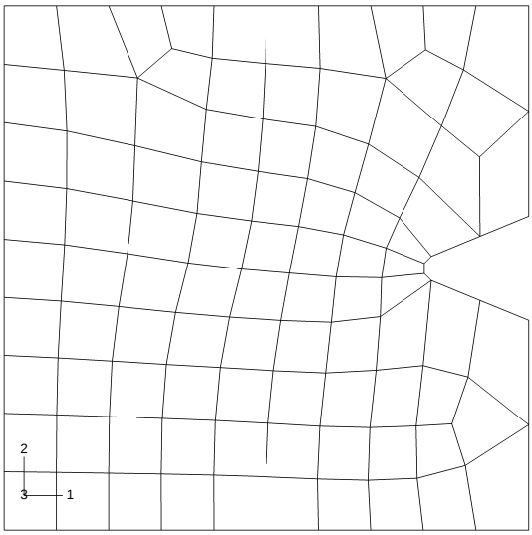

a. FE mesh of the damage zone

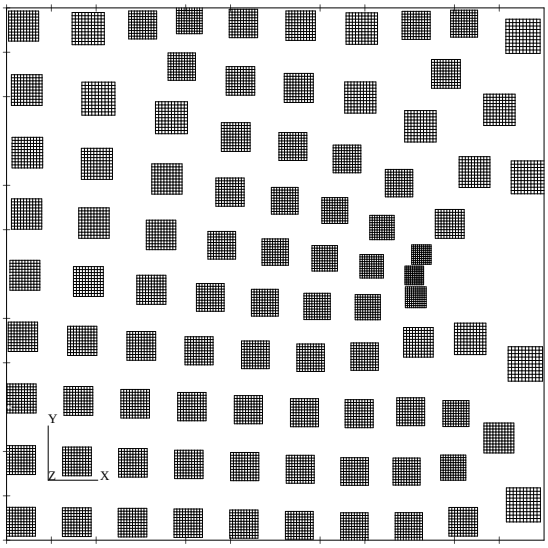

b. Corresponding brittle CA blocks

Figure 4.32: FE mesh of the damage zone and the corresponding brittle CAs.

propagation front is not a straight line but rather an arc (Figures 4.34.c – 4.34.g). The brittle fracture starts after some ductile crack extension (Figure 4.34.d) and stops when the remaining ligament is very small and the dominant

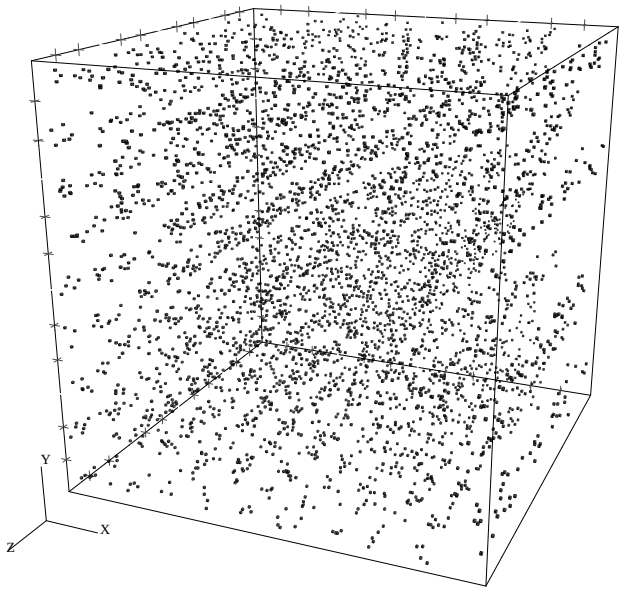

Figure 4.33: Locations of *AliveC* brittle cells.

fracture mode is ductile plastic collapse (Figures 4.34.g and 4.34.h).

This is a very realistic sequence of fracture propagation events.

The fracture surface at the end of the simulation is shown in Figure 4.35. Photographs of three broken Charpy samples of this TMCR steel at $T = -50°$ are shown in Figures 4.43.c – 4.43.e. The simulated percentage of the brittle phase, 54%, is within the range of the experimental values which are from 45% to 75%.

The regions of initial ductile fracture, of brittle fracture and of the final ductile fracture, associated with the plastic collapse in the remaining ligament, which are found in the experimental fracture surfaces at this temperature (Figures 4.43.c – 4.43.e.) are adequately reproduced in the simulated fracture surface (Figure 4.35). Moreover the shapes of these regions are not too dissimilar especially if we remember that the simulated fracture surface is drawn on the initial (undeformed) mesh geometry.

One point of difference between the simulated and the experimental fracture surfaces is that the remaining ligament in the model is unbroken. The finite elements in the last raw of the fracture propagation plane are still alive at the end of the simulation. Figure 4.31 shows that these FEs are highly distorted

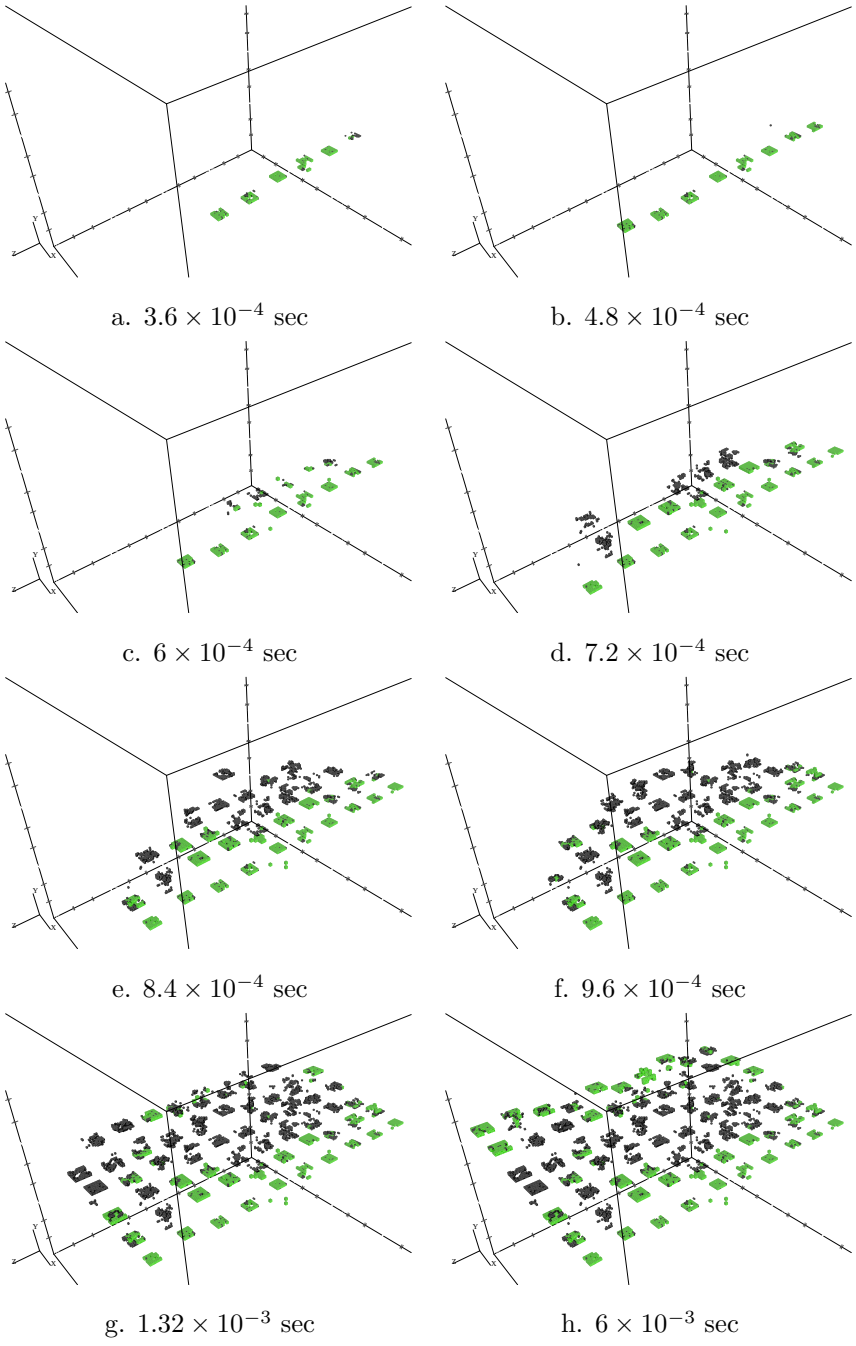

a. 3.6×10^{-4} sec

b. 4.8×10^{-4} sec

c. 6×10^{-4} sec

d. 7.2×10^{-4} sec

e. 8.4×10^{-4} sec

f. 9.6×10^{-4} sec

g. 1.32×10^{-3} sec

h. 6×10^{-3} sec

Figure 4.34: Fracture propagation on the CA scale at $T = -70°$C. Only *DeadB* (black) and *DeadD* (green) cells are shown.

suggesting high shear and very low mean stresses in these elements. Accordingly these elements still carry some load bearing capacity as the Rousselier damage

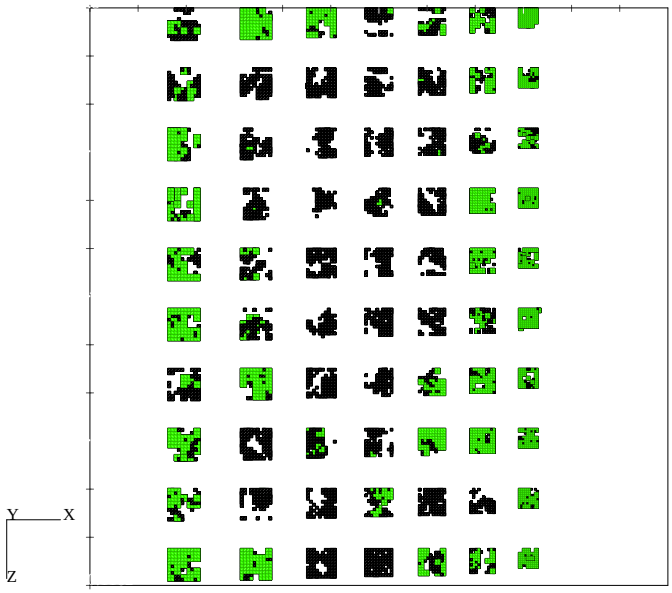

Figure 4.35: The simulated Charpy fracture surface at $T = -50°C$. The brittle phase is 54%.

model can only account for a volumetric void growth, but not for a shape change (section 2.1.6).

An unbroken remaining ligament of 0.1 – 0.25 mm is sometimes observed in the tested Charpy samples of this TMCR steel though usually at higher temperatures.

The results of this example show that the full CAFE model is capable of simulating transitional ductile-brittle fracture in a Charpy specimen. On the micro (CA) scale the model can predict the percentage of the brittle phase, the locations and shapes of the ductile and the brittle fracture regions (Figure 4.35) and the crack front throughout the simulation (Figure 4.34). The force – time data, Figure 4.30.a, and the total energy absorbed are obtained on the macro (FE) scale.

As was said earlier the major problem of the present CAFE model is the inability to simulate brittle cracks running across the finite element boundaries. Such is the limitation of the present realisation of a CAFE approach via the `VUMAT` user subroutine and the `Abaqus` code. Accordingly the brittle fracture

has to reinitialise in each finite element in the fracture propagation path. Thus the brittle zone in the simulated Charpy fracture surface consists of many small cracks rather than of a single large crack (Figure 4.35). On the macro-scale such model behaviour results in a gradual reduction of force as opposed to an instantaneous drop obtained experimentally (Figure 4.30).

Slow brittle fracture propagation can be also caused by a high misorientation threshold, θ_{F}. The value used in this example, $\theta_{\mathrm{F}} = 30°$, is only a rough guess based on very limited experimental data (Bhattacharjee and Davis, 2002).

This example also shows how the fracture stress distribution (Figure 4.28) is obtained from the grain size data (Figure 4.24). Although in this example the separation of the full grain size histogram into two parts probably was not necessary, because the cells with $\sigma_{\mathrm{F}} > 5000$ MPa did not take part in the fracture process, this is a useful technique that can be explored in future (section 5.1).

4.2 The simplified CAFE model

4.2.1 The Charpy test

In this example the simplified CAFE model is used to simulate the scatter usually obtained experimentally in the Charpy test at transitional temperatures.

The ability of the full CAFE model to predict transitional behaviour and scatter in terms of the percentage of the brittle phase was demonstrated for a single-FE model in section 4.1.2 (Figure 4.16). In this example the Charpy test model described in section 4.1.3 with the following parameters was used.

The initial void volume fraction for each ductile CA cell was taken a $f_0 = 1 \times 10^{-4}$.

The critical value of the damage variable, β_{F}, was distributed across the ductile CA arrays using the normal distribution with $\bar{\beta}_{\mathrm{F}} = 8$ and $\mathrm{STD}(\beta_{\mathrm{F}}) = 1.2$. The $\bar{\beta}_{\mathrm{F}}$ value is based on the best-fitted critical damage variable obtained in section 4.1.3. A typical β_{F} histogram is shown in Figure 4.36.

The other two Rousselier model parameters were tuned following the procedure described in section 4.1.3 and the best-fitted values were found to be $\sigma_1 = 517$ MPa and $D = 2.8$.

The best-fitted values for this parameters in the full CAFE model were

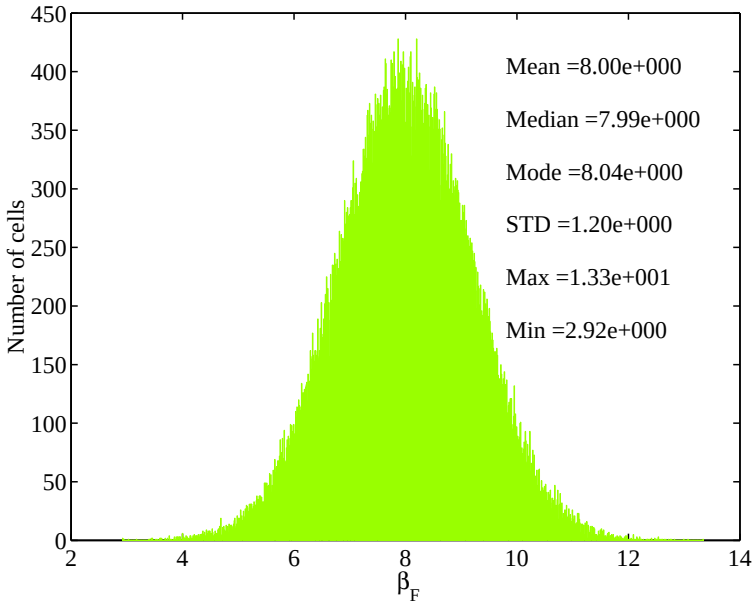

Figure 4.36: A typical histogram of β_{F}.

$\sigma_1 = 500$ MPa and $D = 3$. Thus the difference between the full and the simplified models is small in this respect.

A temperature-dependent misorientation threshold, θ_{F}, is used in this example. The following temperature dependence is used:

$$\theta_{\mathrm{F}} = \begin{cases} \theta_{max} & \text{if} \quad T \leq -80^{\circ}\mathrm{C} \\ a \times T + b & \text{if} \quad -80^{\circ}\mathrm{C} < T < -20^{\circ}\mathrm{C} \\ 0 & \text{if} \quad T \geq -20^{\circ}\mathrm{C} \end{cases} \tag{4.2}$$

where a and b are chosen to ensure continuity of $\theta_{\mathrm{F}}(T)$, as shown in Figure 4.37.

The value of the concentration factor for the brittle CA array was increased to $c_B = 11$ in this example in an attempt to promote faster brittle fracture propagation. The value $c_B = 3$ used in the previous example (section 4.1.3) probably was not high enough and as a consequence the brittle fracture propagation was too slow (Figure 4.30.a).

Also the fraction of brittle cells capable of initiating brittle fracture was increased two times compared to the full CAFE model, to $\eta = 0.01$. So the number of brittle *AliveC* cells was 9000 in the simplified CAFE model.

All other model parameters, which are not mentioned here, have exactly the

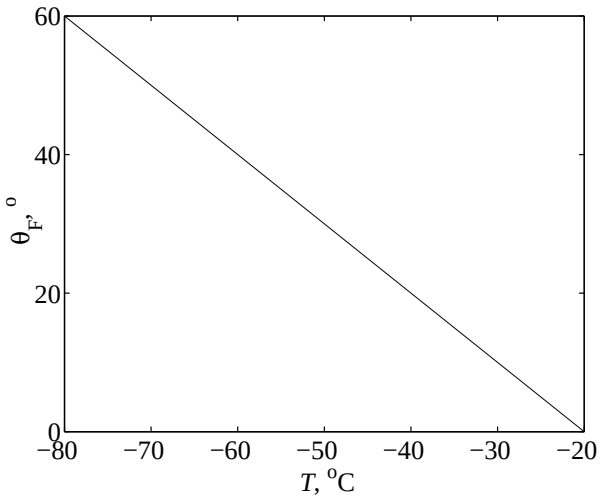

Figure 4.37: The misorientation threshold, $\theta_{\mathrm{F}}(T)$.

same values as in section 4.1.3.

In all simulations of this example variable mass scaling was applied to particularly small finite elements which form contact surfaces for the specimen – anvil interactions (Figure 4.19). A stable time increment thus was increased approximately ten times whereas the change in total energy of the whole model was less than 0.1%. Accordingly the total simulation times were cut by a factor of ten. No mass scaling was applied to the finite elements in the damage zone (Figure 4.21). The running time of each simulation in this example was approximately ten hours.

The simulations were performed at several temperatures from $T = -80°\mathrm{C}$ to $T = 0°\mathrm{C}$, three runs at each temperature.

The results are shown in Figures 4.38 – 4.43. Results on the macro (FE) scale are shown in Figures 4.38 – 4.40. Accordingly Figures 4.41 – 4.43 show results on the micro (CA) scale.

The value of 50% impact transition temperature (ITT) shown in Figure 4.38 is based on the fracture surface appearance. Data presented by Bhattacharjee et al. (2003) shows that for this TMCR steel 50% brittle phase is obtained in the Charpy tests at $T \leq -50°\mathrm{C}$.

The simulation results at $T = 0°\mathrm{C}$ and at $T \leq -75°\mathrm{C}$ agree very well with the experimental data. However, for other temperatures the model predicts a

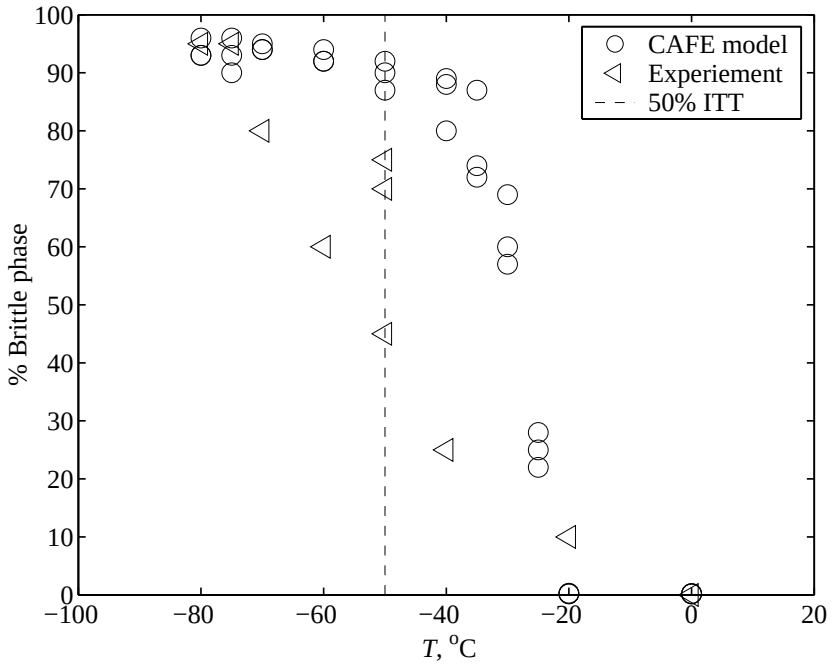

Figure 4.38: Charpy percentage of brittle phase. 50% ITT is taken from Bhattacharjee et al. (2003). Experimental data was provided by Corus UK Ltd.

more sharp transition compared with that obtained experimentally. The 50% ITT on the simulated data is around $T = -30°\text{C}$.

The scatter of the simulated brittle phase values is higher in the transitional region than at the upper and the lower shelf. At the upper shelf, at $T \geq -20°\text{C}$, the three values of the brittle phase obtained at each temperature are virtually identical. At the lower shelf, at $T \leq -60°\text{C}$, the maximum difference between the three values is approximately 3% at $T = -75°\text{C}$. However at transitional temperatures the simulated scatter is much higher. The maximum difference between the three simulated brittle phase values is about 21% at $T = -30°\text{C}$ and $T = -35°\text{C}$. The experimental scatter can only be assessed at $T = -50°\text{C}$ where the maximum and the minimum values differ by 67%.

The experimental transition temperature range is from $T = -75°\text{C}$ to $T = 0°\text{C}$, however, the upper bound value is arguable because there is no clear upper shelf. The simulated data suggests that the modelling transitional temperature range is less wide, approximately from $T = -60°\text{C}$ to $T = -20°\text{C}$.

Finally the simulated transition in Figure 4.38 towards the lower shelf is smoother than towards the upper shelf. This result is in contrast to that obtained in section 4.1.2 for the single-FE model, Figure 4.16. Moreover the lower shelf behaviour in Figure 4.16 is similar to the upper shelf behaviour in Figure 4.38 in that the scatter is very low in both cases. The limit values of the brittle phase (100% for the lower shelf in Figure 4.16 and 0% for the upper shelf in Figure 4.38) were achieved in both cases.

So the single-FE model predicts 100% brittle phase at the lower shelf temperatures, but does not predict 0% brittle phase at the upper shelf, Figure 4.16. In contrast the simplified model of the Charpy test does not predict 100% brittle phase at the lower shelf, but predicts 0% brittle phase at the upper shelf, Figure 4.38. The brittle phase prediction of the simplified model of the Charpy test is probably more physically based and it does agree very well with the experimental data at the lower and the upper shelf.

Such a difference of the CAFE model performances in these two examples is probably caused by different values of the CAFE model parameters and by the fact that fracture cannot cross the finite element boundary due to the limitations of the `Abaqus` code (section 5.1).

Figure 4.39 shows the experimental and the simulated values of the total energy absorbed in the Charpy test.

The model can predict the upper shelf energy values reasonably well, however the lower shelf and the transition temperature range are quite different from the experimental data. The simulated lower shelf is achieved at $T \leq -60^\circ$ and the lower shelf energies are about 60J. There is no clear lower shelf in the experimental data. However, it is reasonable to assume that it starts at $T \leq -80^\circ$ and the energies there are 20J – 40J.

The simulated transition temperature range according to the energy data is the same as the range obtained from the brittle phase results, from $T = -60^\circ$C to $T = -20^\circ$C. However, the experimental transition temperature range obtained from Figure 4.39 is from $T = -80^\circ$C to $T = -20^\circ$C, which is slightly lower than the range that can be perceived from Figure 4.38.

The simulated scatter in energy values at the transitional temperatures is higher than at the lower or at the upper shelf. The maximum difference between

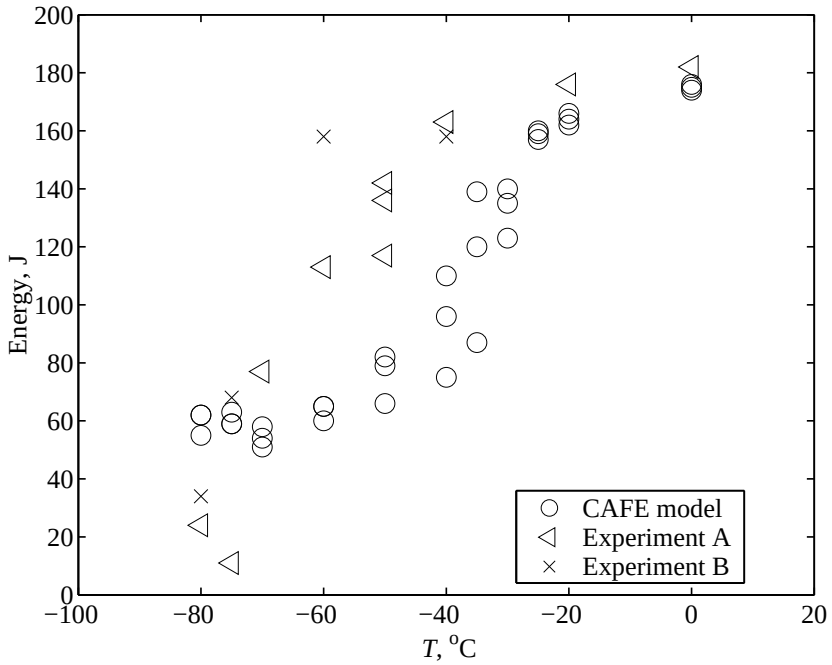

Figure 4.39: Charpy transition energy data. Experimental data A is reproduced from Bhattacharjee et al. (2003), and data B is courtesy of Davis (2003).

the three simulated energy values at the lower shelf is 14% at $T = -70°C$. At the upper shelf the maximum difference is only 1% at $T = -20°C$. However, at $T = -35°C$ the maximum difference is 60%.

The experimental data shows very high scatter at $T = -60°C$ (40% variation) and at $T = -75°C$ (more than 5 times). However, these experimental results must be compared with some caution as they were obtained at different times on different machines by different people, so there is a possibility that different experimental practices could have contributed to such a large scatter.

The energy values predicted by the simplified CAFE model at $T = -50°C$, 66J – 82J (Figure 4.39) are similar to that generated by the full CAFE model, 89J, section 4.1.3.

The lateral expansion measured on the deformed meshes and on the broken Charpy samples is presented in Figure 4.40.

On the whole the simulated lateral expansion data resembles the simulated energy, Figure 4.39. The transition temperature range in Figure 4.40 is from

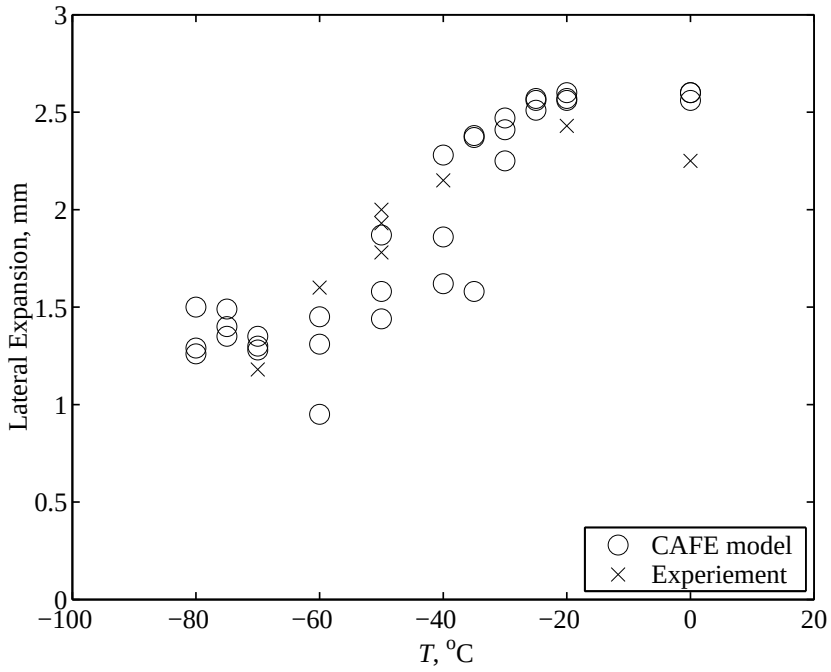

Figure 4.40: Simulated and experimental Charpy lateral expansion data.

$T = -60°\text{C}$ to $T = -20°\text{C}$. The scatter at the upper shelf is very low, less than 1%. The scatter at the lower shelf is higher, 19% at $T = -80°\text{C}$. However, the scatter is much higher at the transitional range, from $T = -60°\text{C}$ to $T = -35°\text{C}$. The maximum difference between the three simulated lateral expansion values is 51% at $T = -35°\text{C}$.

The simulated lateral expansion values agree well with those obtained from the broken Charpy samples using a digital calliper. However, the scatter in the experimental values is smaller than that predicted by the simplified CAFE model at $T = -50°\text{C}$.

Figure 4.41 shows four simulated fracture surfaces obtained at the lower shelf temperatures. Because of the very small level of scatter only one of three simulated surfaces is shown for each temperature. As in section 4.1.3 *deadD* cells are shown green and black cells are *deadB*.

The four fracture surfaces shown in Figure 4.41 differ very slightly. This is an additional evidence in support of the point that the lower shelf behaviour is achieved at $T \leq -60°\text{C}$. All four fracture surfaces show very little areas of

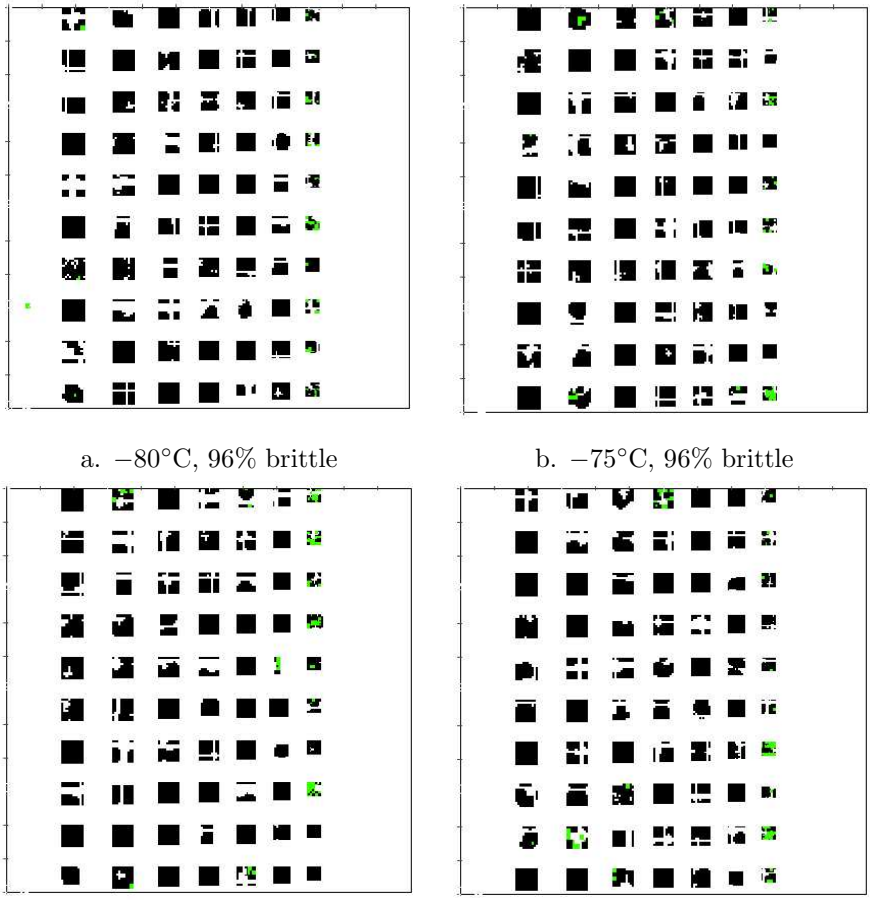

a. −80°C, 96% brittle

b. −75°C, 96% brittle

c. −70°C, 94% brittle

d. −60°C, 94% brittle

Figure 4.41: The simulated Charpy fracture surfaces at the lower shelf temperatures.

ductile fracture, most of them are located immediately below the root of the notch. However, some isolated islands of ductile fracture can be seen far from the notch root in all four surfaces.

Experimental Charpy fracture surfaces obtained at $T = -70°C$ (Figure 4.43.a) and at $T = -60°C$ (Figure 4.43.b) show lower values of the brittle phase, 80% and 60% accordingly. This is primarily due to significantly large ductile shear regions. As was said earlier the present CAFE model cannot simulate shear fracture because the Rousselier damage model can only account for volumetric void growth (section 5.1). Nevertheless there is a qualitative agreement between the simulated and the experimental fracture surfaces at the lower

shelf.

Two of the simulated fracture surfaces at the upper shelf are shown in Figure 4.42. Both show virtually 100% ductile fracture although very few isolated islands of brittle fracture can be seen.

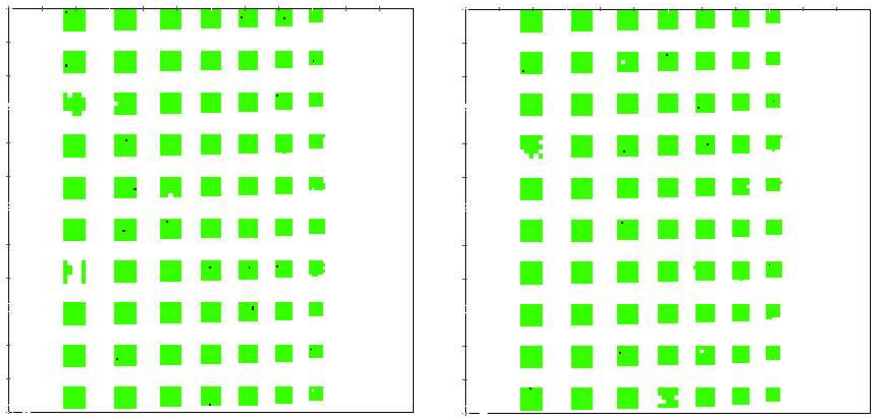

a. $-20°$C, 0% brittle b. $0°$C, 0% brittle

Figure 4.42: The simulated Charpy fracture surfaces at the upper shelf temperatures.

Experimental Charpy fracture surfaces obtained at $T = -20°$C (Figure 4.43.g) and at $T = 0°$C (Figure 4.43.h) have 10% and 0% brittle phase accordingly. These experimental fracture surfaces exhibit substantial delaminations which cannot be modelled at present.

Finally Figure 4.43 shows the simulated fracture surfaces at transitional temperatures. Three surfaces are shown for each temperature to illustrate significant variation from one simulation to another.

At $T = -50°$C and $T = -40°$C the dominant fracture mode predicted by the simplified CAFE model is still brittle, Figures 4.43.a – 4.43.f. However, there are more islands of ductile fracture compared with the surfaces shown in Figure 4.41. At the same time the locations and sizes of the ductile areas vary much more at $T = -50°$C and $T = -40°$C than at the lower shelf temperatures, Figure 4.41.

The simplified model predicted higher fraction of brittle phase at $T = -50°$C (Figures 4.43.a – 4.43.c) that that obtained with the full CAFE model at the same temperature, Figure 4.35. This is most probably due to different values of

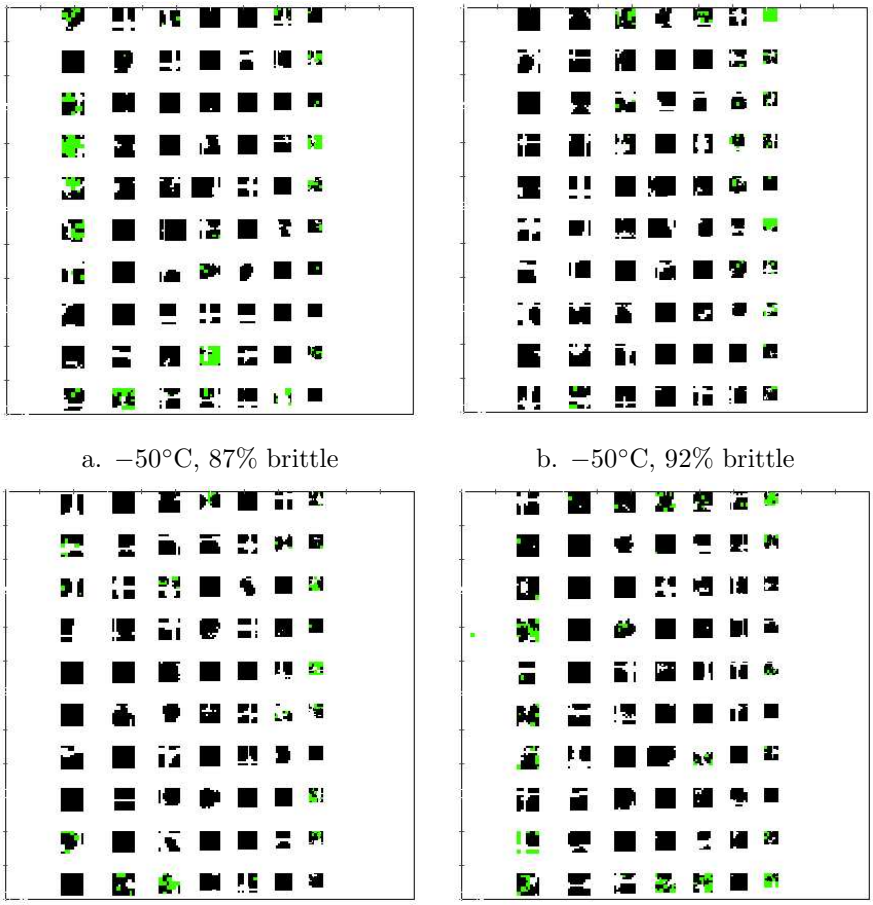

a. −50°C, 87% brittle

b. −50°C, 92% brittle

c. −50°C, 90% brittle

d. −40°C, 88% brittle

Figure 4.43: The simulated Charpy fracture surfaces at transitional temperatures. *(Continued on pages 105 – 106).*

modelling parameters, e.g. c_B, used in the full and the simplified CAFE models.

The simulated fracture surfaces at $T = -50$°C and $T = -40$°C are quite far from the experimental ones shown in Figures 4.43.c – 4.43.f. This is because the simulated percentage of brittle phase is substantially higher than that obtained experimentally.

At temperatures $T = -35$°C and $T = -30$°C, Figures 4.43.g – 4.43.l, the variation from one simulation to another is greater than at $T = -50$°C and $T = -40$°C.

For example at $T = -35$°C Figure 4.43.g shows more islands of ductile fracture towards the back side of the Charpy sample, whereas in Figure 4.43.h

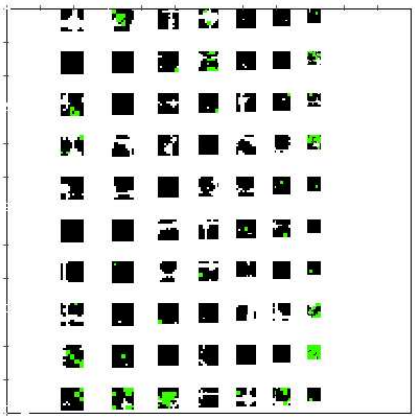

e. −40°C, 89% brittle

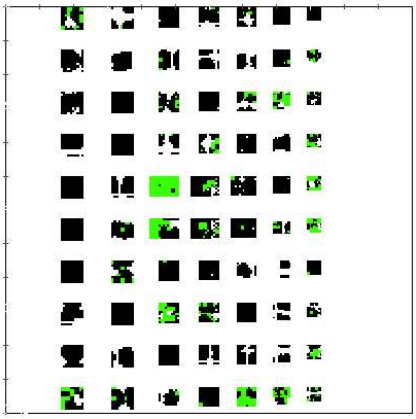

f. −40°C, 80% brittle

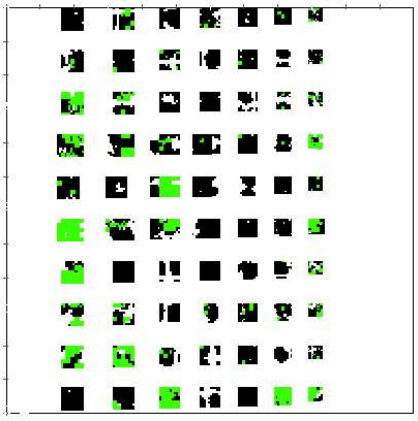

g. −35°C, 74% brittle

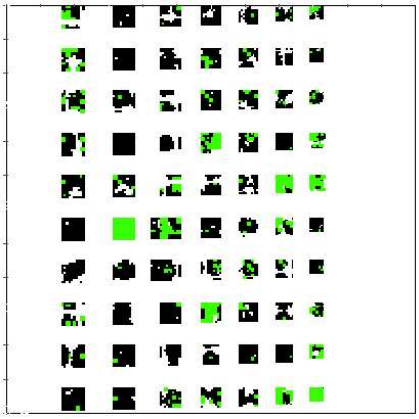

h. −35°C, 72% brittle

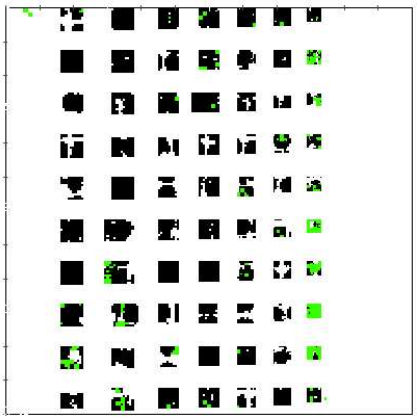

i. −35°C, 87% brittle

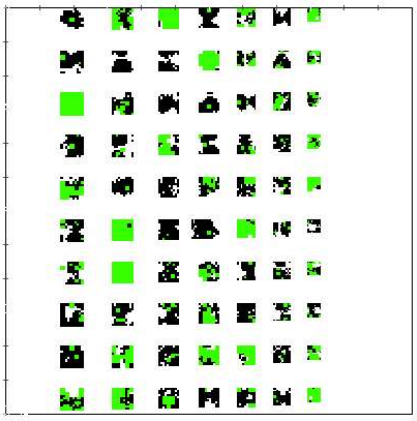

j. −30°C, 57% brittle

Figure 4.43: *Continued.*

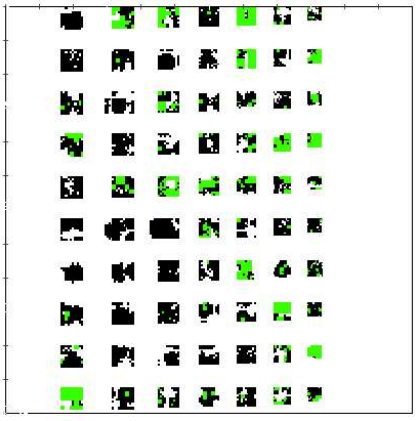

k. −30°C, 69% brittle

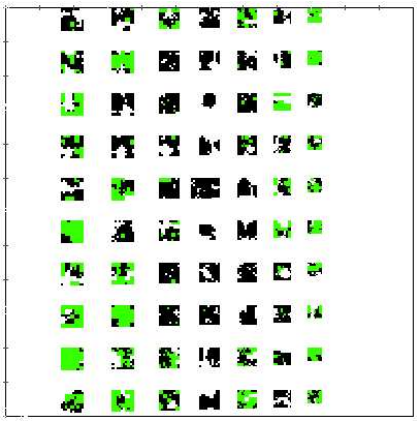

l. −30°C, 60% brittle

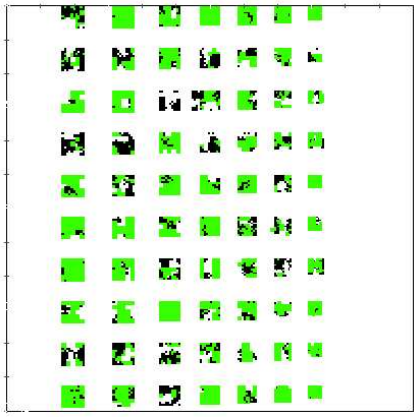

m. −25°C, 25% brittle

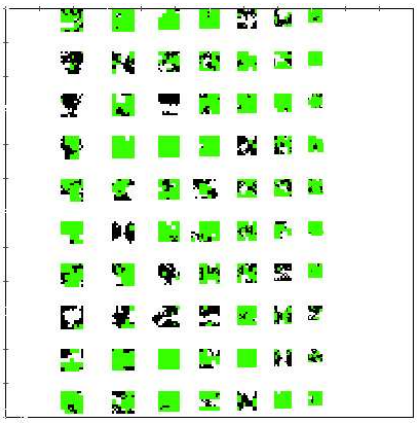

n. −25°C, 28% brittle

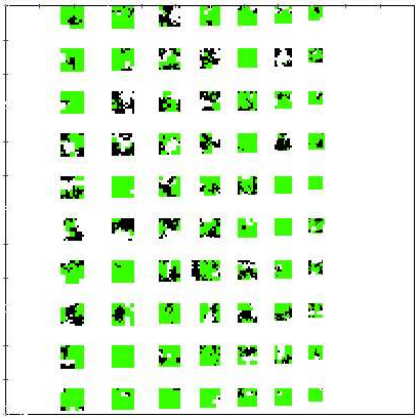

o. −25°C, 22% brittle

Figure 4.43: *Continued.*

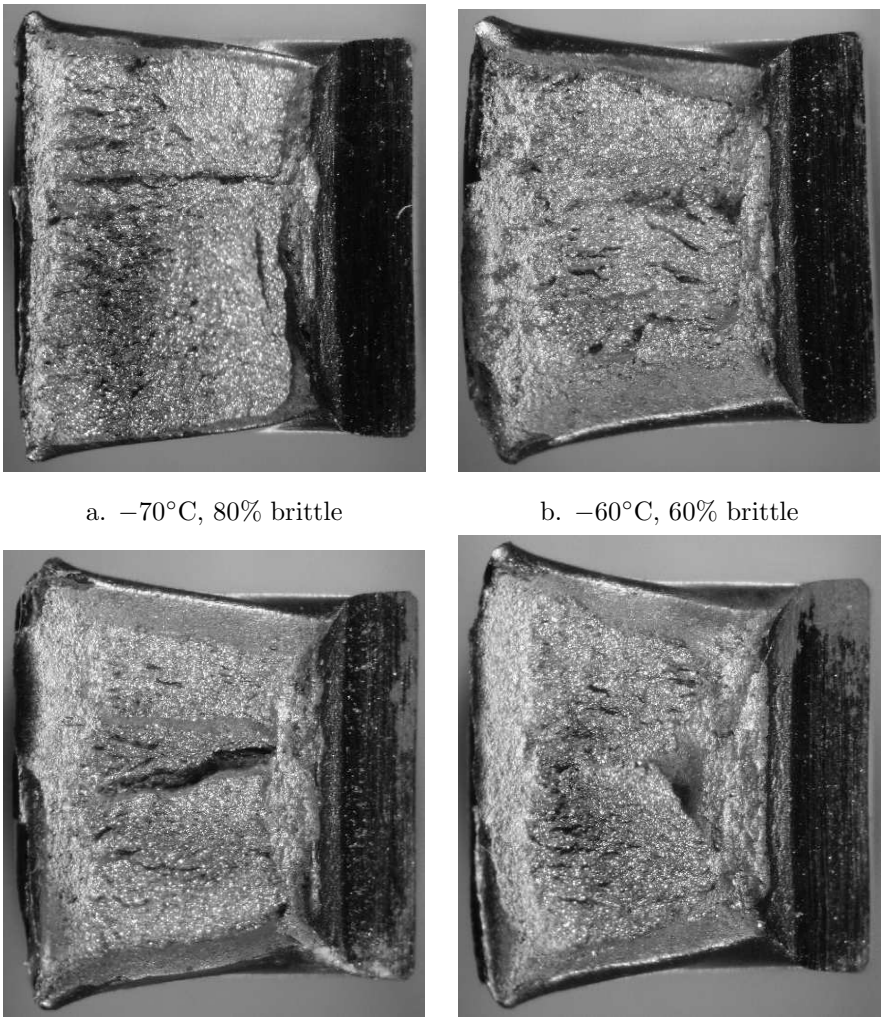

a. −70°C, 80% brittle

b. −60°C, 60% brittle

c. −50°C, 75% brittle

d. −50°C, 70% brittle

Figure 4.43: Fracture surfaces of the broken Charpy samples. The brittle phase values are courtesy of Corus UK Ltd. *(Continued on the next page).*

ductile fracture areas are located closer to the notch of the specimen. However, the final fractions of brittle phase for these two fracture surfaces are very similar, 74% and 72% respectively. The third fracture surface shown in Figure 4.43.i has significantly higher brittle phase, 87%, and accordingly the ductile fracture zones are mostly found next to the notch, although the is one ductile fracture island located in the last (counting from the notch) row of the finite elements.

Similar variations can be found among simulated fracture surfaces at $T =$

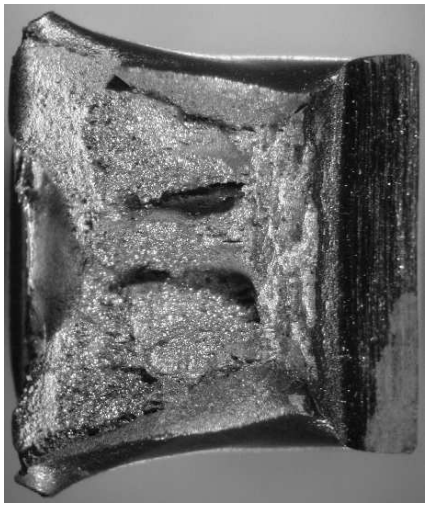

e. $-50°$C, 45% brittle

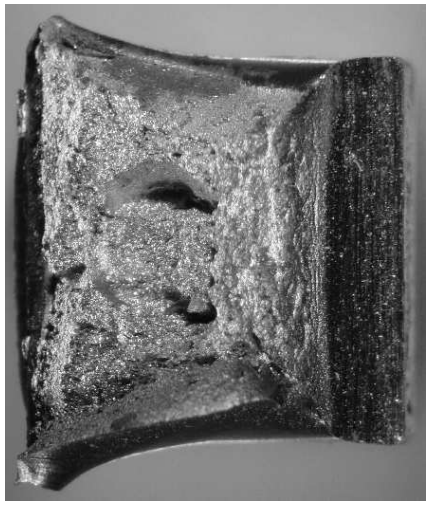

f. $-40°$C, 25% brittle

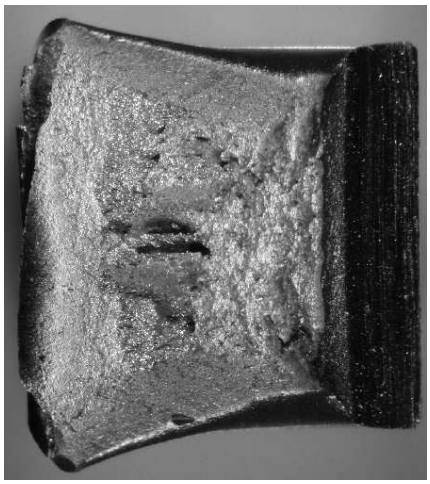

g. $-20°$C, 10% brittle

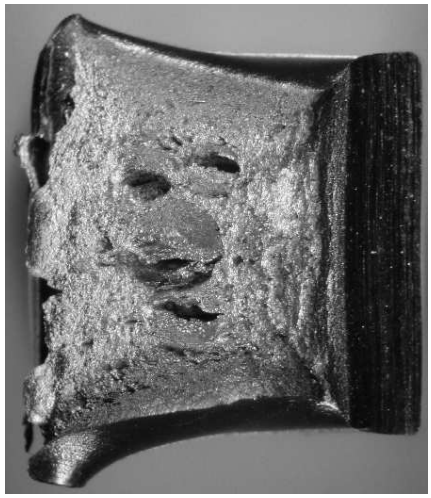

h. $0°$C, 0% brittle

Figure 4.43: *Continued.*

$-30°$C, Figures 4.43.j – 4.43.l. In Figure 4.43.l there is a large brittle region in the centre of the fracture surface surrounded by the areas of ductile fracture. This fracture surface is quite close qualitatively to that shown in Figure 4.35.

Finally at $T = -25°$C, Figures 4.43.m – 4.43.o, the variation from one simulation to another is smaller than at $T = -35°$C and $T = -30°$C. There is no pattern as to where the brittle fracture areas are located. No brittle crack running across the whole of a finite element can be found in any of the three fracture surfaces. This is caused by a relatively small value of the misorientation

threshold, $\theta_{\mathrm{F}} = 5^{\circ}$ at $T = -25^{\circ}$C, Figure 4.37.

Thus low θ_{F} at the upper-transition and the upper shelf temperatures inhibits or stops brittle fracture propagation which otherwise would run very fast across virtually any brittle cell due to very high value of the brittle concentration factor, $c_B = 11$. In contrast, at the lower shelf the brittle fracture can propagate with very few deviations because θ_{F} is so high that virtually all neighbouring cells m and l will have $|\alpha_m - \alpha_l| < \theta_{\mathrm{F}}$.

Thus it is probably true to say that in this example the simplified CAFE model was able to simulate transitional behaviour largely due to the chosen value of c_B and the chosen temperature dependence of θ_{F}, equation (4.2). If these two model parameters had other values then the whole transition curve would have looked differently, or maybe there would have been no transitional behaviour at all.

Chapter 5

Discussion

The results of the four examples of Chapter 4 show that both the full and the simplified CAFE models are suitable for the modelling of transitional ductile-brittle fracture in steels. The performance of the two models differs very slightly, however, the simplified model is much faster.

The ability of the full model to correctly address the strain reversal effects was demonstrated in section 4.1.1 (Figure 4.5). The simulation of strain reversal is a delicate task because many technical details must be taken into account (e.g. elastic unloading, anisotropy of the Rousselier damage model, accurate strain rate decomposition, etc.). Thus among other results this example demonstrates that the Rousselier damage model was coded correctly (Appendix B).

Both the full and the simplified models can predict realistic transitional behaviour, including the levels of scatter, in terms of the percentage of brittle phase (Figures 4.16, 4.34, 4.35, 4.38, 4.41, 4.42 and 4.43) or in terms of the total energy absorbed in the Charpy test (simulation results of section 4.1.3 and Figure 4.39).

It is interesting to note that some results indicate that transition towards the upper shelf is smoother than that towards the lower shelf, e.g. Figures 4.16, 4.38 (experimental data) and Figure 4.39 (both experimental and simulated data). Such a behaviour can be explained with the use of the diagram of Figure 4.18.

Different slopes of the transition curve towards the upper and the lower shelves, either in terms of the energy absorbed or in terms of the brittle phase,

could be caused by the fact that temperature dependence of the first yield stress, $\sigma_{Y0}(T)$, is such that

$$\frac{\partial^2 \sigma_{Y0}}{\partial T^2} > 0 \tag{5.1}$$

within the range of temperatures for which experimental data was available (Figure 4.18). Consequently

$$|\sigma_{Y0}(T + \Delta T) - \sigma_{Y0}(T)| < |\sigma_{Y0}(T - \Delta T) - \sigma_{Y0}(T)|. \tag{5.2}$$

Accordingly the fracture propagation behaviour will change more with decreasing than with increasing temperatures.

However, the simulated brittle phase data in Figure 4.38 exhibits the opposite trend, that the transition towards the lower shelf is smoother than that towards the upper shelf. Probably a temperature dependence of σ_{Y0} is only one of the factors resulting in transition behaviour, and perhaps not the major one.

The transitional behaviour was achieved in the single-FE CAFE model in section 4.1.2, Figure 4.16, solely due to the temperature dependence of σ_{Y0}. This, of course, is only a qualitative prediction because the single-FE model has the uniaxial stress state until the final failure. The model does not account for necking or the strain concentration associated with it. Such a deformation history (the uniaxial stress until failure) is virtually impossible to reproduce experimentally, hence the simulation results obtained on the single-FE model are only suitable for qualitative analysis of the performance of the full CAFE model.

However, the temperature dependence of σ_{Y0} was not enough to simulate a realistic transitional behaviour in the Charpy test. The difference between the first yield stresses at the upper and lower shelf temperatures is relatively small: $\sigma_{Y0}(-80°\text{C}) = 505$ MPa and $\sigma_{Y0}(0°\text{C}) = 453$ MPa (Figure 4.11.a) and the hardening exponent is virtually constant within this temperature range, Figure 4.11.b. Thus the temperature dependence of the misorientation threshold, θ_F, was introduced in equation (4.2), Figure 4.37. With this addition results obtained with the simplified CAFE model were much closer to the experimental data, Figures 4.38, 4.39 and 4.40.

There is little experimental evidence that θ_F is temperature-sensitive. One of the possible explanations for this is that usually misorientation analysis is

performed on fracture surfaces obtained at the lower shelf temperatures (Bhattacharjee and Davis, 2002; Bhattacharjee et al., 2003).

Other authors also had to introduce additional (apart from the temperature dependence of σ_{Y0}) temperature-dependent modelling parameters to make their models predict transitional behaviour. Of these, the most popular is temperature dependence of the scale parameter of Weibull distribution, σ_u, equation (2.28), page 29. Burstow (1998) and Burstow et al. (2003) reported the tuned values of σ_u from 1722.8 MPa at $T = -45°C$ to 2699.9 MPa at $T = 20°C$. The possibility of the temperature dependence of the shape parameter of the Weibull distribution, m, (equation (2.28), page 29) is discussed by Burstow (2003).

Probably a similar effect could have been achieved if the concentration factor for the brittle CA array, c_B, was made temperature-dependent. However such modification has no physical basis and, if introduced, will be just a modelling trick.

Useful information about the fracture progression and change of the percentage of brittle phase during crack propagation can be obtained from Figures 4.6.b, 4.7, 4.14 and 4.15. These outputs, if required, can be easily requested from any finite element in the damage zone of the Charpy model.

With the use of an appropriate visualisation technique many useful details of fracture propagation can be revealed by plotting the states of either the ductile or the brittle CA arrays. In this particular realisation of the CAFE model the brittle CA arrays were designed for visualisation (section 3.2.2). Figures 4.8, 4.9, 4.10, 4.17, 4.34, 4.35, 4.41, 4.42 and 4.43 provide information about the fracture propagation on the micro (CA) scale. The shape of the crack front, the speed of fracture propagation, locations and shapes of the areas of brittle and ductile fracture can be obtained from these Figures.

The ways in which material properties can be taken into account by both models were demonstrated in Chapter 4. Particular attention should be drawn towards the grain size distribution.

It was shown in section 4.1.3 how a duplex grain size distribution was simulated by the full CAFE model. The strategy of applying different random number generators to simulate different parts of the grain size histogram can be used to simulate a grain distribution data of a much greater complexity. Moreover,

additional data (e.g. the histogram of the second phase particle sizes), if available, can be easily included into the model through the fracture stress histogram following the technique used in section 4.1.3. The method used in section 4.1.3 is very simple. However, proper statistical methods are available if one wants to use them (Devroye, 1987; McLachlan and Basford, 1988; Scott, 1992). These methods, however, are significantly more complex and require some knowledge of probability and statistics.

TMCR steels were chosen to verify the CAFE model in Chapter 4 only because the author had an access to the data generated by a thorough study of one particular TMCR steel. However, the CAFE model described in Chapter 3 is designed to be able to simulate other widely used types of steels. Of particular importance for the fracture mechanics community are line pipe steels, ship steels, pressure vessel steels, nuclear reactor steels etc. Moreover the model can be applied to other materials, e.g. aluminium, provided that cell properties and state variables for the brittle and ductile CA arrays, $\Lambda_{m(D)}$, $\Lambda_{m(B)}$, $\Gamma_{m(D)}$ and $\Gamma_{m(B)}$, are chosen according to the knowledge of the micromechanics of fracture of this material.

As was said in section 3 the present CAFE model was built around `C3D8R`, a finite element with a single integration point. This is the only 8-noded finite element allowed in the `Abaqus\Explicit` program. However, if finite elements with several integration points are used (e.g. in another FEA program) then many additional modelling possibilities are open because the macro strain gradients can be supplied to the CA arrays. The algorithms for strain redistribution across CA cells (Step 3, page 49, Step 7, page 51) and for calculating the FE stress (Step 11, page 52) can be modified to take this into account. This will allow for better simulation of local strain and stress concentration ahead of a crack.

The present CAFE models were primarily designed to model fracture propagation. Accordingly the size of the smallest modelling entity (CA cell) is chosen equal to that of the fracture propagation step. However, the model formalism allows for much smaller entities to be used. This can be utilised e.g. for explicit simulation of crack initiation. In this case the smallest modelling entity has to be chosen on the basis of a crack initiation site size, typical of the simulated

material. For steels these are most usually carbides. Accordingly a much more thorough modelling of the fracture initiation can be achieved if the CAFE model has cells of a typical carbide size. This can be technically done in two ways.

The first way is to create all brittle CA cells with size equal to that of a typical carbide in a simulated steel. This approach was explored by Das et al. (2001); Das (2002); Das et al. (2003). The results presented by Das (2002) show very good correlation between the prediction of oxide cracking during hot rolling and the experimental observations of the quality of the slab surface after rolling.

The second approach is to create a third layer of CA only for *aliveC* brittle cells. This additional layer can be used for detailed modelling of stress fields at a grain boundary carbide. The second approach seems more favourable because the third level CA arrays are created only around the grain boundary carbides. So the highest level of detalisation in the CAFE model is used only where it is really required. Moreover, this approach allows for three CA arrays with independent cell sizes.

A detailed simulation of fracture initialisation according to the second approach described above is recommended for future work.

5.1 Unresolved problems and future work

1. Fracture cannot propagate across the finite element boundary at present.

The information given by the Abaqus solver to the `VUMAT` subroutine is limited. For instance no finite element number, either external, given by the user, or internal, used in the solver stiffness matrix, is given to `VUMAT`. This means that it is not possible to establish which finite elements are being processed in this call to the subroutine. Consequently it is not possible to find the neighbouring finite elements from `VUMAT`. Thus fracture must reinitiate in each finite element in the fracture propagation path. Fracture initiation requires more energy than propagation. Therefore this limitation is likely to result in over-estimated energy values.

One way of obtaining the numbers of neighbouring elements is to use material point coordinates which are given to `VUMAT`. However, this procedure is non-trivial and computationally expensive as the full deformation history must be

traced for each finite element in the damage zone. Work in this direction is recommended for the future.

2. Shear ductile fracture cannot be modelled at present. The Rousselier continuous ductile damage model, used in this work, can only account for volumetric void growth.

An additional criterion has to be applied to estimate the onset of shear instability of a ductile damage cell. There are a number of works addressing this issue (Rice, 1977; Rousselier and Barbier, 1997; Barbier et al., 1998). The possibility of including an appropriate shear localisation model into the present CAFE structure was not explored due to time constraints. However this is possible and is recommended for future work.

3. There are many model parameters which require proper tuning before good correlation with the experiment is achieved.

Parameters such as $X_{(D)}^{max}$, $X_{(B)}^{max}$, c_D, c_B strongly affect model performance. Yet, in this work the values for these parameters were based on a rough guess and on some data fitting. A more detailed understanding of the fracture process at the micro-scale might help to find metallurgically meaningful values.

It would be interesting to investigate in greater detail the influence of the CAFE model parameters on various simulation results, e.g. the effect of θ_{F} on the transition temperature range, the link between c_D and c_B and the upper and the lower Charpy energy values, the influence of the grain size distribution on the transition temperature range. It might be better to use a different idea of how $X_{(D)}^{max}$ and $X_{(B)}^{max}$ should be chosen.

This analysis was not performed as part of the present work because of significant demands for the computing power and time constraints.

5.2 Overall conclusions

The CAFE model proposed in this work is designed for fast three-dimensional multi-scale analysis. One typical application of such a model is a simulation of transitional ductile-brittle fracture in steels. This engineering problem is of high practical importance. However, so far it could not be solved successfully

by the pure finite element methods. The results presented in this work show how this problem can be solved with the CAFE model.

The author believes that the model can be useful in other areas of engineering. It might need to be modified, additional parameters might need to be included, but the basic structure can remain as described in Chapter 3.

Appendix A

The CA cell neighbourhood

Figure A.1 illustrates the 26-cell neighbourhood used in both the full and the simplified CAFE models. The neighbourhood is shown as three sections of a $3 \times 3 \times 3$ cell cube along direction k (or 3).

Each neighbourhood cell has three characteristics. These are:

1. Direction cosines, i.e. the cosines of angles that a line, connecting the centres of each cell with the central cell, makes with the basis axes (i, j, k),

2. Cell coordinates relative to the coordinates of the central cell,

3. The cell number.

These characteristics are written in three lines inside each neighbourhood cell in Figure A.1.

Because of the central symmetry only 13 out of 26 neighbouring cells have unique combination of direction cosines. These cells have unique numbers. Their symmetrical partner cells have the same number but with a bar on top, e.g. cell $\bar{6}$ is a symmtrical partner of cell 6.

Coordinates of each neighbourhood cell are, of course, unique.

↑ j, 2

$\frac{1}{\sqrt{3}}; -\frac{1}{\sqrt{3}}; \frac{1}{\sqrt{3}}$ i-1; j+1; k-1 $\bar{3}$	$0; \frac{1}{\sqrt{2}}; -\frac{1}{\sqrt{2}}$ i; j+1; k-1 $1\bar{0}$	$\frac{1}{\sqrt{3}}; \frac{1}{\sqrt{3}}; -\frac{1}{\sqrt{3}}$ i+1; j+1; k-1 7
$\frac{1}{\sqrt{2}}; 0; \frac{1}{\sqrt{2}}$ i-1; j; k-1 $\bar{6}$	$0; 0; 1$ i; j; k-1 $1\bar{1}$	$\frac{1}{\sqrt{2}}; 0; -\frac{1}{\sqrt{2}}$ i+1; j; k-1 4
$\frac{1}{\sqrt{3}}; \frac{1}{\sqrt{3}}; \frac{1}{\sqrt{3}}$ i-1; j-1; k-1 $\bar{9}$	$0; \frac{1}{\sqrt{2}}; \frac{1}{\sqrt{2}}$ i; j-1; k-1 $1\bar{3}$	$-\frac{1}{\sqrt{3}}; \frac{1}{\sqrt{3}}; \frac{1}{\sqrt{3}}$ i+1; j-1; k-1 1

→ i, 1

$-\frac{1}{\sqrt{2}}; \frac{1}{\sqrt{2}}; 0$ i-1; j+1; k $\bar{2}$	$0; 1; 0$ i; j+1; k 12	$\frac{1}{\sqrt{2}}; \frac{1}{\sqrt{2}}; 0$ i+1; j+1; k 8
$1; 0; 0$ i-1; j; k $\bar{5}$	i; j; k central cell	$1; 0; 0$ i+1; j; k 5
$\frac{1}{\sqrt{2}}; \frac{1}{\sqrt{2}}; 0$ i-1; j-1; k $\bar{8}$	$0; 1; 0$ i; j-1; k $1\bar{2}$	$-\frac{1}{\sqrt{2}}; \frac{1}{\sqrt{2}}; 0$ i+1; j-1; k 2

$-\frac{1}{\sqrt{3}}; \frac{1}{\sqrt{3}}; \frac{1}{\sqrt{3}}$ i-1; j+1; k+1 $\bar{1}$	$0; \frac{1}{\sqrt{2}}; \frac{1}{\sqrt{2}}$ i; j+1; k+1 13	$\frac{1}{\sqrt{3}}; \frac{1}{\sqrt{3}}; \frac{1}{\sqrt{3}}$ i+1; j+1; k+1 9
$\frac{1}{\sqrt{2}}; 0; -\frac{1}{\sqrt{2}}$ i-1; j; k+1 $\bar{4}$	$0; 0; 1$ i; j; k+1 11	$\frac{1}{\sqrt{2}}; 0; \frac{1}{\sqrt{2}}$ i+1; j; k+1 6
$\frac{1}{\sqrt{3}}; \frac{1}{\sqrt{3}}; -\frac{1}{\sqrt{3}}$ i-1; j-1; k+1 $\bar{7}$	$0; \frac{1}{\sqrt{2}}; -\frac{1}{\sqrt{2}}$ i; j-1; k+1 10	$\frac{1}{\sqrt{3}}; -\frac{1}{\sqrt{3}}; \frac{1}{\sqrt{3}}$ i+1; j-1; k+1 3

↙ k, 3

Figure A.1: Neighbouring cell numbering convention

Appendix B

Rousselier model integration

Integration of the Rousselier continuous material damage model (Rousselier et al. (1989), section 2.1.6) for a single integration point is shown below.

Where explicit time is not given, t_{i+1} is assumed.

If we substitute differentials by finite differences the complete set of equiations will have the form (Aravas, 1987; Rousselier et al., 1989; HKS, 2001):

$$\Delta\epsilon_m^p - \Delta\epsilon_{eq}^p \frac{B(\beta)}{3\sigma_1} Dexp\left(\frac{\sigma_m}{\rho\sigma_1}\right) = 0 \tag{B.1}$$

$$\frac{\sigma_{eq}}{\rho} - H\left(\epsilon_{eq}^p\right) + B(\beta)\, Dexp\left(\frac{\sigma_m}{\rho\sigma_1}\right) = 0 \tag{B.2}$$

$$\sigma_m = \sigma_m^e - 3K\Delta\epsilon_m^p \tag{B.3}$$

$$\sigma_{eq} = \sigma_{eq}^e - 3G\Delta\epsilon_{eq}^p \tag{B.4}$$

$$\Delta\beta = \Delta\epsilon_{eq}^p Dexp\left(\frac{\sigma_m}{\rho\sigma_1}\right) \tag{B.5}$$

$$\rho(\beta) = \frac{1}{1 - f_0 + f_0 exp\beta} \tag{B.6}$$

$$B(\beta) = \frac{\sigma_1 f_0 exp\beta}{1 - f_0 + f_0 exp\beta} \tag{B.7}$$

where $\sigma_m^e = \frac{1}{3}\sigma_{ii}^e$; $\sigma_{eq}^e = \sqrt{\frac{3}{2}S_{ij}^e S_{ij}^e}$; $S_{ij}^e = \sigma_{ij}^e - \sigma_m^e\delta_{ij}$; $\sigma_{ij}^e = E_{ijkl}\hat{\epsilon}_{kl}$ and

$$\hat{\epsilon}_{kl} = \epsilon_{ij}^e(t_i) + \Delta\epsilon_{ij} \tag{B.8}$$

$$\epsilon^p_{eq} = \epsilon^p_{eq}(t_i) + \Delta\epsilon^p_{eq} \tag{B.9}$$

$$\beta = \beta(t_i) + \Delta\beta \tag{B.10}$$

For the rest of the variables refer to the Nomenclature, page 10, and to section 2.1.6, page 23.

The equations (B.1) – (B.7) are solved by the Newton's method. The strain increments $\Delta\epsilon^p_m$ and $\Delta\epsilon^p_{eq}$ are primarily unknowns. We find them by solving the equations (B.1) and (B.2). If we write the equations (B.1) and (B.2) as:

$$\begin{cases} f\left(\Delta\epsilon^p_m, \Delta\epsilon^p_{eq}, \Delta\beta\right) = 0 \\ g\left(\Delta\epsilon^p_m, \Delta\epsilon^p_{eq}, \Delta\beta\right) = 0 \end{cases} \tag{B.11}$$

then the solution is found by the iterative process. Each cycle the following matrix equation is solved:

$$J \cdot c = A \tag{B.12}$$

where

$$J = \begin{pmatrix} \frac{\partial f}{\partial \Delta\epsilon^p_m} & \frac{\partial f}{\partial \Delta\epsilon^p_{eq}} \\ \frac{\partial g}{\partial \Delta\epsilon^p_m} & \frac{\partial g}{\partial \Delta\epsilon^p_{eq}} \end{pmatrix}, \quad c = \begin{pmatrix} c_m \\ c_{eq} \end{pmatrix}, \quad A = -\begin{pmatrix} f \\ g \end{pmatrix}.$$

Then the strain increments are updated:

$$\Delta\epsilon^p_m \Leftarrow \Delta\epsilon^p_m + c_m \tag{B.13}$$

$$\Delta\epsilon^p_{eq} \Leftarrow \Delta\epsilon^p_{eq} + c_{eq} \tag{B.14}$$

The steps (B.12), (B.13) and (B.14) are repeated until the correction values c_m amd c_{eq} are less that the specified tolerance.

Components of Jacobian

$$\frac{\partial f}{\partial \Delta\epsilon^p_m} = 1 - \frac{D\Delta\epsilon^p_{eq}}{3\sigma_1} \frac{\partial}{\partial \Delta\epsilon^p_m}\left[B\left(\beta\right) exp\left(\frac{\sigma_m}{\rho\sigma_1}\right)\right] \tag{B.15}$$

$$\frac{\partial f}{\partial \Delta\epsilon^p_{eq}} = -\frac{B\left(\beta\right)}{3\sigma_1} D exp\left(\frac{\sigma_m}{\rho\sigma_1}\right) - \frac{D\Delta\epsilon^p_{eq}}{3\sigma_1} \frac{\partial}{\partial \Delta\epsilon^p_{eq}}\left[B\left(\beta\right) exp\left(\frac{\sigma_m}{\rho\sigma_1}\right)\right] \tag{B.16}$$

$$\frac{\partial g}{\partial \Delta\epsilon^p_m} = \frac{\partial}{\partial \Delta\epsilon^p_m}\left(\frac{\sigma_{eq}}{\rho}\right) + D\frac{\partial}{\partial \Delta\epsilon^p_m}\left[B\left(\beta\right) exp\left(\frac{\sigma_m}{\rho\sigma_1}\right)\right] \tag{B.17}$$

$$\frac{\partial g}{\partial \Delta\epsilon^p_{eq}} = \frac{\partial}{\partial \Delta\epsilon^p_{eq}}\left(\frac{\sigma_{eq}}{\rho}\right) - \frac{\partial H\left(\epsilon^p_{eq}\right)}{\partial \Delta\epsilon^p_{eq}} + D\frac{\partial}{\partial \Delta\epsilon^p_{eq}}\left[B\left(\beta\right) exp\left(\frac{\sigma_m}{\rho\sigma_1}\right)\right] \tag{B.18}$$

further:

$$\frac{\partial}{\partial \Delta\epsilon_m^p}\left[B\left(\beta\right)exp\left(\frac{\sigma_m}{\rho\sigma_1}\right)\right] = \frac{\partial B\left(\beta\right)}{\partial\beta}\frac{\partial\beta}{\partial\Delta\epsilon_m^p}exp\left(\frac{\sigma_m}{\rho\sigma_1}\right) + B\left(\beta\right)exp\left(\frac{\sigma_m}{\rho\sigma_1}\right)\frac{1}{\sigma_1}\left(\frac{\partial\sigma_m}{\partial\Delta\epsilon_m^p}\frac{1}{\rho} + \sigma_m\frac{\partial\frac{1}{\rho}}{\partial\beta}\frac{\partial\beta}{\partial\Delta\epsilon_m^p}\right) \tag{B.19}$$

$$\frac{\partial}{\partial \Delta\epsilon_{eq}^p}\left[B\left(\beta\right)exp\left(\frac{\sigma_m}{\rho\sigma_1}\right)\right] = \frac{\partial B\left(\beta\right)}{\partial\beta}\frac{\partial\beta}{\partial\Delta\epsilon_{eq}^p}exp\left(\frac{\sigma_m}{\rho\sigma_1}\right) + B\left(\beta\right)exp\left(\frac{\sigma_m}{\rho\sigma_1}\right)\frac{1}{\sigma_1}\left(\frac{\partial\sigma_m}{\partial\Delta\ epsilon_{eq}^p}\frac{1}{\rho} + \sigma_m\frac{\partial\frac{1}{\rho}}{\partial\beta}\frac{\partial\beta}{\partial\Delta\epsilon_{eq}^p}\right) \tag{B.20}$$

$$\frac{\partial}{\partial \Delta\epsilon_m^p}\left(\frac{\sigma_{eq}}{\rho}\right) = \frac{\partial\sigma_{eq}}{\partial\Delta\epsilon_m^p}\frac{1}{\rho} + \sigma_{eq}\frac{\partial\frac{1}{\rho}}{\partial\beta}\frac{\partial\beta}{\partial\Delta\epsilon_m^p} \tag{B.21}$$

$$\frac{\partial}{\partial \Delta\epsilon_{eq}^p}\left(\frac{\sigma_{eq}}{\rho}\right) = \frac{\partial\sigma_{eq}}{\partial\Delta\ epsilon_{eq}^p}\frac{1}{\rho} + \sigma_{eq}\frac{\partial\frac{1}{\rho}}{\partial\beta}\frac{\partial\beta}{\partial\Delta\epsilon_{eq}^p} \tag{B.22}$$

From (B.7):

$$\frac{\partial B\left(\beta\right)}{\partial\beta} = \sigma_1 f_0\frac{exp\beta(1-f_0+f_0exp\beta) - f_0(exp\beta)^2}{\left(1-f_0+f_0exp\beta\right)^2} = \frac{\sigma_1 f_0 exp\beta(1-f_0)}{\left(1-f_0+f_0exp\beta\right)^2} \tag{B.23}$$

From (B.6):

$$\frac{\partial\frac{1}{\rho}}{\partial\beta} = f_0 exp\beta \tag{B.24}$$

From (B.3):

$$\frac{\partial\sigma_m}{\partial\Delta\epsilon_m^p} = -3K \tag{B.25}$$

$$\frac{\partial\sigma_m}{\partial\Delta\epsilon_{eq}^p} = 0 \tag{B.26}$$

From (B.4):

$$\frac{\partial\sigma_{eq}}{\partial\Delta\epsilon_m^p} = 0 \tag{B.27}$$

$$\frac{\partial\sigma_{eq}}{\partial\Delta\epsilon_{eq}^p} = -3G \tag{B.28}$$

Calculations of partial derivatives $\frac{\partial\beta}{\partial\Delta\epsilon_m^p}$ and $\frac{\partial\beta}{\partial\Delta\epsilon_{eq}^p}$ is slightly more complicated because dependence between the variables β, $\Delta\epsilon_m^p$ and $\Delta\epsilon_{eq}^p$ is described by an implicit function defined by equation (B.5).

If we regroup equation (B.5) to the following form

$$h\left(\Delta\beta, \Delta\epsilon_{eq}^p, \Delta\epsilon_m^p\right) = \Delta\beta - \Delta\epsilon_{eq}^p Dexp\left(\frac{\sigma_m}{\rho\sigma_1}\right) = 0 \tag{B.29}$$

we can get the sought partial derivatives using the formula for partial derivatives of the implicit function (e.g. Brand, 1955):

$$\frac{\partial \beta}{\partial \Delta \epsilon_m^p} = -\frac{\frac{\partial h}{\partial \Delta \epsilon_m^p}}{\frac{\partial h}{\partial \Delta \beta}} \tag{B.30}$$

$$\frac{\partial \beta}{\partial \Delta \epsilon_{eq}^p} = -\frac{\frac{\partial h}{\partial \Delta \epsilon_{eq}^p}}{\frac{\partial h}{\partial \Delta \beta}} \tag{B.31}$$

In the above we used the fact that $\beta = \beta_t + \Delta\beta$ that leads to $\frac{\partial \beta}{\partial \Delta \epsilon_m^p} = \frac{\partial \Delta \beta}{\partial \Delta \epsilon_m^p}$ and $\frac{\partial \beta}{\partial \Delta \epsilon_{eq}^p} = \frac{\partial \Delta \beta}{\partial \Delta \epsilon_{eq}^p}$.

Thus we can obtain from (B.29):

$$\frac{\partial h}{\partial \Delta \epsilon_m^p} = -\Delta \epsilon_{eq}^p D exp\left(\frac{\sigma_m}{\rho \sigma_1}\right) \frac{1}{\sigma_1 \rho} \frac{\partial \sigma_m}{\partial \Delta \epsilon_m^p} \tag{B.32}$$

$$\frac{\partial h}{\partial \Delta \epsilon_{eq}^p} = -D exp\left(\frac{\sigma_m}{\rho \sigma_1}\right) - \Delta \epsilon_{eq}^p D exp\left(\frac{\sigma_m}{\rho \sigma_1}\right) \frac{1}{\sigma_1 \rho} \frac{\partial \sigma_m}{\partial \Delta \epsilon_{eq}^p} \tag{B.33}$$

$$\frac{\partial h}{\partial \Delta \beta} = 1 - \Delta \epsilon_{eq}^p D exp\left(\frac{\sigma_m}{\rho \sigma_1}\right) \frac{\sigma_m}{\sigma_1} \frac{\partial \frac{1}{\rho}}{\partial \Delta \beta} \tag{B.34}$$

By sibstituting (B.32), (B.33) and (B.34) into (B.30) and (B.31), and taking into account that $\frac{\partial \sigma_m}{\partial \Delta \epsilon_{eq}^p} = 0$ and $\frac{\partial \frac{1}{\rho}}{\partial \Delta \beta} = \frac{\partial \frac{1}{\rho}}{\partial \beta}$, we get:

$$\frac{\partial \beta}{\partial \Delta \epsilon_m^p} = -\frac{-\Delta \epsilon_{eq}^p D exp\left(\frac{\sigma_m}{\rho \sigma_1}\right) \frac{1}{\sigma_1 \rho} \frac{\partial \sigma_m}{\partial \Delta \epsilon_m^p}}{1 - \Delta \epsilon_{eq}^p D exp\left(\frac{\sigma_m}{\rho \sigma_1}\right) \frac{\sigma_m}{\sigma_1} \frac{\partial \frac{1}{\rho}}{\partial \beta}} \tag{B.35}$$

$$\frac{\partial \beta}{\partial \Delta \epsilon_{eq}^p} = -\frac{-D exp\left(\frac{\sigma_m}{\rho \sigma_1}\right)}{1 - \Delta \epsilon_{eq}^p D exp\left(\frac{\sigma_m}{\rho \sigma_1}\right) \frac{\sigma_m}{\sigma_1} \frac{\partial \frac{1}{\rho}}{\partial \beta}} \tag{B.36}$$

By simlifying these equations we get:

$$\frac{\partial \beta}{\partial \Delta \epsilon_m^p} = \frac{\Delta \epsilon_{eq}^p D exp\left(\frac{\sigma_m}{\rho \sigma_1}\right) \frac{1}{\sigma_1 \rho} \frac{\partial \sigma_m}{\partial \Delta \epsilon_m^p}}{1 - \Delta \epsilon_{eq}^p D exp\left(\frac{\sigma_m}{\rho \sigma_1}\right) \frac{\sigma_m}{\sigma_1} \frac{\partial \frac{1}{\rho}}{\partial \beta}} \tag{B.37}$$

$$\frac{\partial \beta}{\partial \Delta \epsilon_{eq}^p} = \frac{D exp\left(\frac{\sigma_m}{\rho \sigma_1}\right)}{1 - \Delta \epsilon_{eq}^p D exp\left(\frac{\sigma_m}{\rho \sigma_1}\right) \frac{\sigma_m}{\sigma_1} \frac{\partial \frac{1}{\rho}}{\partial \beta}} \tag{B.38}$$

By substituting (B.24)-(B.28) into (B.19)-(B.22), (B.37) and (B.38) we get:

$$\frac{\partial}{\partial \Delta \epsilon_m^p}\left[B(\beta) exp\left(\frac{\sigma_m}{\rho \sigma_1}\right)\right] = exp\left(\frac{\sigma_m}{\rho \sigma_1}\right)\left[\frac{\partial B(\beta)}{\partial \beta}\frac{\partial \beta}{\partial \Delta \epsilon_m^p} + \frac{B(\beta)}{\sigma_1}\left(\frac{-3K}{\rho} + \sigma_m f_0 exp\beta \frac{\partial \beta}{\partial \Delta \epsilon_m^p}\right)\right] \tag{B.39}$$

$$\frac{\partial}{\partial \Delta\epsilon^p_{eq}}\left[B(\beta)\,exp\left(\frac{\sigma_m}{\rho\sigma_1}\right)\right] = exp\left(\frac{\sigma_m}{\rho\sigma_1}\right)\left(\frac{\partial B(\beta)}{\partial\beta}\frac{\partial\beta}{\partial\Delta\epsilon^p_{eq}} + \frac{B(\beta)}{\sigma_1}\sigma_m f_0 exp\beta\frac{\partial\beta}{\partial\Delta\epsilon^p_{eq}}\right) \tag{B.40}$$

$$\frac{\partial}{\partial\Delta\epsilon^p_m}\left(\frac{\sigma_{eq}}{\rho}\right) = \sigma_{eq} f_0 exp\beta\frac{\partial\beta}{\partial\Delta\epsilon^p_m} \tag{B.41}$$

$$\frac{\partial}{\partial\Delta\epsilon^p_{eq}}\left(\frac{\sigma_{eq}}{\rho}\right) = \frac{-3G}{\rho} + \sigma_{eq} f_0 exp\beta\frac{\partial\beta}{\partial\Delta\epsilon^p_{eq}} \tag{B.42}$$

$$\frac{\partial\beta}{\partial\Delta\epsilon^p_m} = \frac{-3K\Delta\epsilon^p_{eq} Dexp\left(\frac{\sigma_m}{\rho\sigma_1}\right)}{\rho\left(\sigma_1 - \Delta\epsilon^p_{eq} Dexp\left(\frac{\sigma_m}{\rho\sigma_1}\right)\sigma_m f_0 exp\beta\right)} \tag{B.43}$$

$$\frac{\partial\beta}{\partial\Delta\epsilon^p_{eq}} = \frac{Dexp\left(\frac{\sigma_m}{\rho\sigma_1}\right)}{1 - \Delta\epsilon^p_{eq} Dexp\left(\frac{\sigma_m}{\rho\sigma_1}\right)\frac{\sigma_m}{\sigma_1} f_0 exp\beta} \tag{B.44}$$

The components of Jacobian can be found as:

$$\frac{\partial f}{\partial\Delta\epsilon^p_m} = 1 - \frac{D\Delta\epsilon^p_{eq}}{3\sigma_1}\frac{\partial}{\partial\Delta\epsilon^p_m}\left[B(\beta)\,exp\left(\frac{\sigma_m}{\rho\sigma_1}\right)\right] \tag{B.45}$$

$$\frac{\partial f}{\partial\Delta\epsilon^p_{eq}} = -\frac{D}{3\sigma_1}\left\{B(\beta)\,exp\left(\frac{\sigma_m}{\rho\sigma_1}\right) + \Delta\epsilon^p_{eq}\frac{\partial}{\partial\Delta\epsilon^p_{eq}}\left[B(\beta)\,exp\left(\frac{\sigma_m}{\rho\sigma_1}\right)\right]\right\} \tag{B.46}$$

$$\frac{\partial g}{\partial\Delta\epsilon^p_m} = \sigma_{eq} f_0 exp\beta\frac{\partial\beta}{\partial\Delta\epsilon^p_m} + D\frac{\partial}{\partial\Delta\epsilon^p_m}\left[B(\beta)\,exp\left(\frac{\sigma_m}{\rho\sigma_1}\right)\right] \tag{B.47}$$

$$\frac{\partial g}{\partial\Delta\epsilon^p_{eq}} = \frac{-3G}{\rho} + \sigma_{eq} f_0 exp\beta\frac{\partial\beta}{\partial\Delta\epsilon^p_{eq}} - \frac{\partial H\left(\epsilon^p_{eq}\right)}{\partial\Delta\epsilon^p_{eq}} + D\frac{\partial}{\partial\Delta\epsilon^p_{eq}}\left[B(\beta)\,exp\left(\frac{\sigma_m}{\rho\sigma_1}\right)\right] \tag{B.48}$$

where

$$\frac{\partial}{\partial\Delta\epsilon^p_m}\left[B(\beta)\,exp\left(\frac{\sigma_m}{\rho\sigma_1}\right)\right] = exp\left(\frac{\sigma_m}{\rho\sigma_1}\right)\left[\frac{\partial B(\beta)}{\partial\beta}\frac{\partial\beta}{\partial\Delta\epsilon^p_m} + \frac{B(\beta)}{\sigma_1}\left(\frac{-3K}{\rho} + \sigma_m f_0 exp\beta\frac{\partial\beta}{\partial\Delta\epsilon^p_m}\right)\right] \tag{B.49}$$

$$\frac{\partial}{\partial\Delta\epsilon^p_{eq}}\left[B(\beta)\,exp\left(\frac{\sigma_m}{\rho\sigma_1}\right)\right] = exp\left(\frac{\sigma_m}{\rho\sigma_1}\right)\left(\frac{\partial B(\beta)}{\partial\beta}\frac{\partial\beta}{\partial\Delta\epsilon^p_{eq}} + \frac{B(\beta)}{\sigma_1}\sigma_m f_0 exp\beta\frac{\partial\beta}{\partial\Delta\epsilon^p_{eq}}\right) \tag{B.50}$$

$$\frac{\partial \beta}{\partial \Delta \epsilon_m^p} = \frac{-3K\Delta\epsilon_{eq}^p Dexp\left(\frac{\sigma_m}{\rho\sigma_1}\right)}{\rho\left(\sigma_1 - \Delta\epsilon_{eq}^p Dexp\left(\frac{\sigma_m}{\rho\sigma_1}\right)\sigma_m f_0 exp\beta\right)} \tag{B.51}$$

$$\frac{\partial \beta}{\partial \Delta \epsilon_{eq}^p} = \frac{Dexp\left(\frac{\sigma_m}{\rho\sigma_1}\right)}{1 - \Delta\epsilon_{eq}^p Dexp\left(\frac{\sigma_m}{\rho\sigma_1}\right)\frac{\sigma_m}{\sigma_1} f_0 exp\beta} \tag{B.52}$$

$$\frac{\partial B(\beta)}{\partial \beta} = \frac{\sigma_1 f_0 exp\beta(1-f_0)}{(1-f_0+f_0 exp\beta)^2} \tag{B.53}$$

Equations (B.1) – (B.14) and (B.45) – (B.53) are required to find $\Delta\epsilon_m^p$ and $\Delta\epsilon_{eq}^p$.

When $\Delta\epsilon_m^p$ and $\Delta\epsilon_{eq}^p$ are known then σ_m and σ_{eq} are found from equations (B.3) and (B.4), β from (B.10) and (B.5) and

$$\sigma_{ij} = \frac{\sigma_{eq}}{\sigma_{eq}^e} S_{ij}^e + \sigma_m \delta_{ij} \tag{B.54}$$

$$\Delta\epsilon_{ij}^p = \frac{3}{2}\frac{S_{ij}^e}{\sigma_{eq}^e}\Delta\epsilon_{eq}^p + \Delta\epsilon_m^p \delta_{ij}, \tag{B.55}$$

$$\epsilon_{ij}^e = \epsilon_{ij}^e(t_i) + \Delta\epsilon_{ij} - \Delta\epsilon_{ij}^p \tag{B.56}$$

As seen from equations (B.8) – (B.10) the elastic strain tensor, ϵ_{ij}^e, equivalent plastic strain, ϵ_{eq}^p, and the damage variable, β, have to be stored from one time increment to another throughout the analysis.

Bibliography

Andersson, H. (1977), 'Analysis of a model for void growth and coalescence ahead of a moving crack tip', *Journal of the Mechanics and Physics of Solids* **25**, 217–233.

Andrews, R. M., I. C. Howard, A. Shterenlikht and J. R. Yates (2002), The Effective Resistance of Pipeline Steels to Running Ductile Fractures; Modelling of Laboratory Test Data, *in* A.Neimitz, I. V.Rokach, D.Kocańda and K.Gołoś, eds, 'ECF14, Fracture Mechanics Beyond 2000', EMAS Publications, Sheffield, UK, pp. 65–72.

Aravas, N. (1987), 'On the numerical integration of a class of pressure-dependent plasticity models', *International journal for numerical methods in engineering* **24**, 1395–416.

Argon, A. S. and J. Im (1975), 'Separation of second phase particles in spheroidized 1045 steel, Cu - 0.6% Cr alloy, and maraging steel in plastic straining', *Metallurgical Transactions A* **6**, 839–51.

Argon, A. S., J. Im and R. Safoglu (1975), 'Cavity fomation from inclusions in ductile fracture', *Metallurgical Transactions A* **6**, 825–837.

Ashby, M. F., F. J. Blunt and M. Bannister (1989), 'Flow characteristics of highly constrained metal wires', *Acta Metallurgica* **37**(7), 1847–1857.

Averbach, B. L., D. K. Felbeck, G. T. Hahn and D. A. Thomas, eds (1959), *Fracture. Proceedings of an International Conference on the Atomic Mechanisms of Fracture held in Swampscott, Massachusetts, April 12–16, 1959*, The

Technology Press of Massachusetts Institute of Technology and John Wiley & Sons, New York.

Barbier, G., G. Rousselier, R. Lebrun and Y. Sun (1998), 'Analytical prediction of intrinsic length scales in strain localisation', *Journal de Physique IV* **8**(P8), 19–27.

Bates, R. C. (1984), Modelling of ductile fracture by microvoid coalescence for the prediction of fracture toughness, *in* J. M.Wells and J. D.Landes, eds, 'Fracture: Interactions of Microstructure, Mechanisms and Mechanics', The Metallurgical Society of AIME, pp. 117–155.

Batisse, R., M. Bethmont, G. Devesa and G. Rousselier (1987), 'Ductile fracture of a 508 Cl 3 steel in relation with inclusion content: the benefit of the local approach to fracture and continuum damage mechanics', *Nuclear Engineering and Design* **105**(1), 113–120.

Beachem, C. D. (1963), 'An electron fractography study of the influence of plastic strain conditions upon ductile rupture processes in metals', *Transactions of the ASM* **56**, 318–326.

Beachem, C. D. (1975), 'The effects of crack tip plastic flow directions upon microscopic dimple shapes', *Metallurgical Transactions A* **6**, 377–383.

Belytschko, T., W. K. Liu and B. Moran (2000), *Nonlinear Finite Elements for Continua and Structures*, John Wiley & Sons.

Beremin, F. M. (1983), 'A local criterion for cleavage fracture of a nuclear pressure vessel steel', *Metallurgical Transactions A* **14**, 2277–2287.

Berg, C. A. (1970), Plastic dilation and void interaction, *in* M. F.Kanninen, ed., 'Inelastic Behaviour of Solids', McGraw-Hill, pp. 171–209.

Beynon, J. H., S. Das, I. C. Howard, E. J. Palmiere and A. Chterenlikht (2002), The combination of Cellular Automata and Finite Elements for the Study of Fracture; the CAFE Model of Fracture, *in* A.Neimitz, I. V.Rokach, D.Kocańda and K.Gołoś, eds, 'ECF14, Fracture Mechanics Beyond 2000', EMAS Publications, Sheffield, UK, pp. 241–248.

Bhattacharjee, D. and C. L. Davis (2002), 'Influence of processing history on mesotexture and microstructure-toughness relationship in control-rolled and normalised steels', *Scripta Materialia* **47**(12), 825–831.

Bhattacharjee, D., C. L. Davis and J. F. Knott (2003), 'Predictability of charpy impact toughness in thermomechanically control rolled (TMCR) microalloyed steels', *Ironmaking and Steelmaking* **30**(3), 249–255.

Bilby, B. A., I. C. Howard, A. M. Othman, D. P. G. Lidbury and A. H. Sherry (1994), Prediction of spinning cylinder tests 2 and 3 using continuum damage mechanics, *in* H. S.Mehta, ed., 'Fracture Mechanics Applications, PVP-Vol.287/MD-Vol.47', The American Society of Mechanical Engineeers, pp. 3–10.

Bilby, B. A., I. C. Howard and Z. H. Li (1994), 'Mesh independent cell models for continuum damage theory', *Fatigue and Fracture of Engineering Materials and Structures* **17**(10), 1221–1233.

Bluhm, J. I. and R. J. Morrissey (1964), *Preliminary investigation of the frature mechanism in a tensile specimen*, US Army Materials Research Agency, Watertown, Massachusetts, USA.

Bluhm, J. I. and R. J. Morrissey (1966), Fracture in a tensile specimen, *in* 'Proceedings of First International Conference on Fracture, Vol. 3', Japanese Society for Strength and Fracture of Materials, Sendai, Japan, pp. 1739–1780.

Brand, L. (1955), *Advanced calculus*, John Wiley & Sons, New York.

Bridgman, P. W. (1952), *Studies in Large Plastic Flow and Fracture*, Metallurgy and Metallurgical Engineering Series, 1 edn, McGraw-Hill.

Brown, L. M. and J. D. Embury (1973), The initiation and growth of voids at second-phase particles, *in* 'Proceedings of the 3rd International Conference on Strength of Metals and Alloys', Institute of Metals, London, pp. 164–169.

BS EN 10045-1 (1990), British Standard. *Metallic materials – Charpy impact test – Part 1: Test method*, British Standards Institution.

Burstow, M. C. (1998), Local approach analysis of fracture in the transition region, Technical report, Department of Mechanical Engineering, The University of Sheffield.

Burstow, M. C. (2003), 'A re-assessment of parameters tuning for the beremin model using the toughness scaling technique', to be submitted.

Burstow, M. C., D. W. Beardsmore, I. C. Howard and D. P. G. Lidbury (2003), 'The prediction of constraint-dependent R6 failure assessment lines for a pressure vessel steel via micromechanical modelling of fracture', to be submitted.

CEI (2002), *EnSight User Manual, Version 7.4*, Computational Engineerig International, Inc., Apex, North Carolina, USA.

Compaq (1999), *Visual Fortran Version 6.1*, Digital Equipment Corporation, USA.

Cottrell, A. H. (1959), Theoretical aspects of fracture, *in* Averbach et al. (1959), pp. 20–53.

Cottrell, A. H. (1967), The nature of metals, *in* D.Flannagan, F.Bello and P.Morrison, eds, 'Meterials', W. H. Freeman and Company, San Francisco, pp. 39–55.

Cox, T. B. and J. R. Low, Jr (1974), 'An investigation of the plastic fracture of AISI 4340 and 18 Nickel 200 grade maraging steels', *Metallurgical Transactions* **5**, 1457–1470.

Curry, D. A. and J. F. Knott (1978), 'Effects of microstructure on cleavage fracture stress in steel', *Metal Science* **12**, 511–514.

Czochralski, J. (1924), *Moderne Metallkunde in Theorie und Praxis* (Modern metal science in theory and practice), Springer-Verlag, Berlin.

Das, S. (2002), The effect of boundary conditions and material data representation on the simulation of deformation during hot rolling, PhD thesis, Department of Engineering Materials, The University of Sheffield, UK.

Das, S., E. J. Palmiere and I. C. Howard (2001), CAFE: A new approach to the modelling of multipass hot rolling, *in* 'Proceedings of Modelling of Metal

Rolling Processes Symposium 11 - Through Process Modelling', The Institute of Materials, London, pp. 33–40.

Das, S., E. J. Palmire and I. C. Howard (2003), CAFE: a tool for modelling thermomechanical processes, *in* E. J.Palmire, M.Mahfouf and C.Pinna, eds, 'Thermomechanical Processing: Mechanics, Microstructure and Control, Proceeding of the International Conference, Sheffield, 23 - 26 June, 2002', IMMPETUS, BBR Solutions, Chesterfield, UK, pp. 296–301.

Davis, C. L. (2003), Private communication. Metallurgy and Materials, The University of Birmingham.

Devroye, L. (1987), *A Course in Density Estimation*, Vol. 14 of *Progress in Probability and Statistics*, Birkhäuser, Boston, USA.

Drucker, D. C. (1951), A more fundamental approach to stress-strain relations, *in* 'Proceedings of the First U.S. National Congress of Applied Mechanics', pp. 487–491.

Drucker, D. C. (1959), 'A definition of stable inelastic material', *Journal of Applied Mechanics* **26**, 101–106.

Eripret, C., D. P. G. Lidbury, A. Sherry and I. C. Howard (1996), 'Prediction of fracture in the transition regime: application to an A533B pressure vessel steel', *Journal de Physique IV* **6**(C6), 315–323.

Faleskog, J. and C. F. Shih (1997), 'Micromechanics of coalescence–I. Synergetic effects of elasticity, plastic yelding and multi-size-scale voids', *Journal of the Mechanics and Physics of Solids* **45**(1), 21–50.

Faleskog, J., X. Gao and C. F. Shih (1998), 'Cell model for nonlinear fracture analysis – I. micromechanics calibration', *International Journal of Fracture* **89**(4), 355–373.

Folch, L. C. A. (1997), Application of the local damage mechanics approach to transition temperature behaviour in steels, PhD thesis, University of Manchester Institute of Science and Technology, Department of Civil and Structural Engineering.

Folch, L. C. A. and F. M. Burdekin (1999), 'Application of coupled brittle-ductile model to study correlation between charpy energy and fracture toughness values', *Engineering Fracture Mechanics* **63**(1), 57–80.

Franklin, A. G. (1969), 'Comparison between a quantitative microscopic and chemical methods for assessment of non-metallic inclusions', *Journal of the Iron and Steel Institute* **207**, 181–186.

Gandin, C. A., J. L. Desbiolles, M. Rappaz and P. Thevoz (1999), 'A three-dimensional cellular automaton – finite element model for the prediction of solidification grain structures', *Metallurgical and Materials Transactions A* **30**(12), 3153–3165.

Gao, X., J. Faleskog and C. F. Shih (1998), 'Cell model for nonlinear fracture analysis – II. fracture process calibration and verification', *International Journal of Fracture* **89**(4), 375–398.

Gao, X., J. Faleskog and C. F. Shih (1999), 'Analysis of ductile to cleavage transition in part-through cracks using a cell model incorporating statistics', *Fatigue and Fracture of Engineering Materials and Structures* **22**(3), 239–250.

Germain, P., Q. S. Nguyen and P. Suquet (1983), 'Continuum thermodynamics', *Journal of Applied Mechanics* **50**(12), 1010–1020.

Gilman, J. J. (1969), *Micromechanics of Flow in Solids*, Materials Science and Engineering, McGraw-Hill, New York.

Gladman, T. (1997), *The Physical Metallurgy of Microalloyed Steels*, Iron and Steel Institute, London.

Gladman, T., B. Holmes and F. B. Pickering (1970), 'Work hardening of low-carbon steels', *Journal of the Iron and Steel Institute* **208**, 172–183.

Gladman, T., B. Holmes and I. D. McIvor (1971), *Effects of Second Phase Particles on the Mechanical Properties of Steels*, Iron and Steel Institute, London.

Gologanu, M., J. B. Leblond and J. Devaux (1993), 'Approximate models for ductile metals containing non-spherical voids – case of axisymmetric pro-

late ellipsiodal cavities', *Journal of the Mechanics and Physics of Solids* **41**(11), 1723–1754.

Gologanu, M., J. B. Leblond and J. Devaux (1994), 'Approximate models for ductile metals containing non-spherical voids – case of axisymmetric oblate ellipsiodal cavities', *Journal of Engineering Materials and Technology* **116**(3), 290–297.

Goods, S. H. and L. M. Brown (1979), 'The nucleation of cavities by plastic deformation', *Acta Metallurgica* **27**, 1–15.

Griffith, A. A. (1921), 'The phenomena of fracture and flow in solids', *Philosophical Transactions of the Royal Society of London, Series A* **221**, 163–98.

Griffith, A. A. (1924), The theory of rupture, *in* 'Proceedings of the first international congress for applied mechanics', Delft, pp. 55–63.

Gücer, D. E. and J. Gurland (1962), 'Comparison of the statistics of two fracture modes', *Journal of the Mechanics and Physics of Solids* **10**(4), 365–373.

Gurland, J. (1972), 'Observations of the fracture of cementite particles in a spheroidized 1.05%C steel deformed at room temperature', *Acta Metallurgica* **20**, 735–741.

Gurland, J. and J. Plateau (1963), 'The mechanism of ductile rupture of metals containing inclusions', *Transactions of the ASM* **56**, 443–454.

Gurson, A. L. (1977*a*), 'Continuum theory of ductile rupture by void nucleation and growth: Part I - yield criteia and flow rules for porous ductile media', *Journal of Engineering Materials and Technology* **99**, 2–15.

Gurson, A. L. (1977*b*), Porous rigid-plastic materials containing rigid inclusions - Yield function, plastic potential, and void nucleation, *in* D. M. R.Taplin, ed., 'Proceedings of the international conference on fracture, Vol. 2A', Pergamon Press, pp. 357–364.

Hahn, G. T. (1984), 'The influence of microstructure on brittle fracture toughness', *Metallurgical Transactions A* **15**(6), 947–959.

Hahn, G. T., B. L. Averbach, W. S. Owen and M. Cohen (1959), Initiation of cleavage microcracks in polycrystalline iron and steel, *in* Averbach et al. (1959), pp. 91–116.

Hayden, H. W. and S. Floreen (1969), 'Observations of localised deformation during ductile fracture', *Acta Metallurgica* **17**, 213–214.

Hertzberg, R. W. (1996), *Deformation and Fracture Mechanics of Engineering Materials*, 4 edn, John Wiley & Sons.

Hesselbarth, H. W. and I. R. Göbel (1991), 'Simulation of recrystallization by cellular automata', *Acta Metallurgica et Materialia* **39**(9), 2135–2143.

Hill, R. (1983), *The Mathematical Theory of Plasticity*, The Oxford Engineering Science Series, Oxford: Clarendon Press.

HKS (2001), *ABAQUS Theory Manual, Version 6.2*.

Howard, I. C., Z. H. Li and M. A. Sheikh (2000), Modeling the ductile to cleavage transition in steels and structures, *in* P. C.Paris and K. L.Jerina, eds, 'Fatigue and Fracture Mechanics: 30th Volume, ASTM STP 1360', American Society for Testing and Materials, West Conshohocken, PA, USA, pp. 152–168.

Howard, I. C., Z. H. Li, M. A. Sheikh, D. P. G. Lidbury and A. H. Sherry (1996), The simulation of the fourth spinning cylinder test using damage mechanics, *in* K.Yoon, ed., 'Fatigue and Fracture, vol. 2, Proc. ASME PVP Conference, Montreal, July 21-26.', The American Society of Mechanical Engineeers, New York, pp. 257–265.

Huang, Y., J. W. Hutchnison and V. Tvergaard (1991), 'Cavitation instabilities in elastic-plastic solids', *Journal of the Mechanics and Physics of Solids* **39**(2), 223–241.

Jang, J. I., B. W. Lee, J. B. Ju, D. Kwon and W. S. Kim (2003), 'Experimental analysis of the practical LBZ effects on the brittle fracture performance of cryogenic steel HAZs with respect to crack arrest toughness near fusion line', *Engineering Fracture Mechanics* **70**(10), 1245–1257.

Johnson, C. (1987), *Numerical Solution of Partial Differential Equations by the Finite Element Method*, Cambridge University Press.

Kachanov, L. M. (1971), *Foundations of the Theory of Plasticity*, North-Holland Publishing Company, Amsterdam, Netherlands.

Kelly, A. and G. W. Groves (1970), *Crystallography and Crystal Defects*, Longman, London, UK.

Khalili, A. and K. Kromp (1991), 'Statistical properties of Weibull estimators', *Journal of Materials Science* **26**(24), 6741–6752.

Khan, A. S. and S. Huang (1995), *Continuum Theory of Plasticity*, John Wiley & Sons, New York.

Knott, J. F. (1973), *Fundamentals of Fracture Mechanics*, Butterworth, London.

Kohout, J. (2001), Various regressional functions fitting transition curves, *in* D.François and A.Pineau, eds, 'Proceedings of the Charpy Centenary Conference, Poitiers, 2 – 5 October 2001.', ESIS, Société Française de Métallurgie et de Matériaux, France, pp. 81–88.

Koppenhoefer, C. and R. H. Dodds, Jr (1998), 'Ductile crack growth in precracked CVN specimens: numerical studies', *Nuclear Engineering and Design* **180**(3), 185–289.

Kroon, M. and J. Faleskog (2002), 'A probabilistic model for cleavage fracture with a length scale-influence of material parameters and constraints', *International Journal of Fracture* **118**(2), 99–118.

Lemaitre, J. (1985), 'A continuum damage mechanics model for ductile fracture', *Journal of Engineering Materials and Technology* **107**(1), 83–89.

Lemaitre, J. (1996), *A Course on Damage Mechanics*, 2 edn, Springer.

Lidbury, D. P. G., A. H. Sherry, B. A. Bilby, I. C. Howard, Z. H. Li and C. Eripret (1994), 'Prediction of the first spinning cylinder test using continuum damage mechanics', *Nuclear Engineering and Design* **152**(1-3), 1–10.

Lin, T., A. G. Evans and R. O. Ritchie (1987), 'Stochastic modeling of the independent roles of particle size and grain size in transgranular cleavage fracture', *Metallurgical Transactions A* **18**(4), 641–651.

Liu, C. T. and J. Gurland (1968), 'The fracture behaviour of spheroidized carbon steels', *Transactions of the ASM* **61**, 156–167.

Malik, L., L.N. Pussegoda, B.A. Graville and W.R. Tyson (1996), 'Crack arrest toughness of a heat-affected zone containing local brittle zones', *Journal of Offshore Mechanics and Arctic Engineering, Transactions of The ASME* **118**(4), 292–299.

McClintock, F. A. (1968), 'A criterion for ductile fracture by the growth of voids', *Journal of Applied Mechanics* **35**, 363–371.

McDowell, D. L., ed. (1997), *Applications of Continuum Damage Mechanics to Fatigue and Fracture*, American Society for Testing and Materials, STP 1315.

McLachlan, G. J. and K. E. Basford (1988), *Mixture Models: Inference and Applications to Clustering*, Vol. 84 of *Statistics: Textbooks ad Monographs*, Marcel Dekker, Inc., 270 Madison Avenue, New York, USA.

McMahon, Jr, C. J. and M. Cohen (1965), 'Initiation of cleavage in polycrystalline iron', *Acta Metallurgica* **13**, 591–604.

Nadai, A. (1950), *Theory of Flow and Fracture of Solids*, Engineering Societies Monographs, 2 edn, McGraw-Hill, New York.

Needleman, A. (1972), 'Void growth in an elastic-plastic medium', *Journal of Applied Mechanics* **39**, 964–970.

Nohava, J., P. Haušild, M. Karlík and P. Bompard (2002), 'Electron backscattering diffraction analysis of secondary cleavage cracks in a reactor pressure vessel steel', *Materials Characterization* **49**(3), 211–217.

Pardoen, T. and J. W. Hutchinson (2000), 'An extended model for void growth and coalescence', *Journal of the Mechanics and Physics of Solids* **48**(12), 2467–2512.

Prager, W. (1959), *An Introduction to Plasticity*, The Addison-Wesley series in the engineering sciences, Addison-Wesley, Reading, Massachusetts, USA.

Puttick, K. E. (1959), 'Ductile fracture in metals', *Philosophical Magazine, Series 8* **4**(44), 964–969.

Raabe, D. and R. C. Becker (2000), 'Coupling of a crystal plasticity finite-element model with a probabilistic cellular automaton for simulating primary static recrystallization in aluminium', *Modelling and Simulation in Materials Science and Engineering* **8**(4), 445–462.

Rabotnov, Yu. N. (1969), *Creep Problems in Structural Members.* Translated from Russian, originally entitled: *Polzuchest Elementov Konstruktsii*, Nauka, Moscow, 1966, North-Holland.

Rhines, W. J. (1961), Ductile fracture by the growth of pores, Master's thesis, MIT, Department of Mechanical Engineering.

Rice, J. R. (1977), The localization of plastic deformation, *in* W. T.Koiter, ed., 'Theoretical and applied mechanics', North-Holland, Amsterdam, pp. 207–220.

Rice, J. R. and D. M. Tracey (1969), 'On the ductile enlargement of voids in triaxial stress fields', *Journal of the Mechanics and Physics of Solids* **17**, 201–217.

Ritchie, R. O., J. F. Knott and J. R. Rice (1973), 'On the relationship between critical tensile stress and fracture toughness in mild steel', *Journal of the Mechanics and Physics of Solids* **21**, 395–410.

Rogers, H. C. (1960), 'Tensile fracture of ductile metals', *Transactions of the Metallurgical Society of AIME* **218**, 498–506.

Rousselier, G. (1981), Finite deformation constitutive relations including ductile fracture damage, *in* S.Nemat-Nasser, ed., 'Three Dimensional Constitutive Relations and Ductile Fracture', North-Holland, pp. 331–355.

Rousselier, G. (1987), 'Ductile fracture models and their potential in local approach to fracture', *Nuclear Engineering and Design* **105**(1), 97–111.

Rousselier, G. and G. Barbier (1997), Analytical modeling of the shear mode and opening mode of ductile fracture, *in* A. B.Geltmacher, P.Matic and K.Sadananda, eds, 'Recent Advances in Fracture. Proceedings of the TMS meeting, 10–13 February 1997, Orlando, Florida', The Minerals, Metals & Materials Society, USA, pp. 195–203.

Rousselier, G., J.-C. Devaux, G. Mottel and G. Devesa (1989), A methodology of ductile fracture analysis based on damage mechanics: an illustration of a local approach of fracture, *in* J. D.Landes, A.Saxena and J. G.Merkle, eds, 'Nonlinear fracture mechanics: Volume II - Elastic-Plastic Fracture, ASTM STP 995', Philadelphia, pp. 332–354.

Ruggieri, C. (1998), 'Probabilistic treatment of fracture using two failure models', *Probabilistic Engineering Mechanics* **13**(4), 309–319.

Ruggieri, C., F. Minami and M. Toyoda (1995), 'A statistical approach for fracture of brittle materials based on the chain-of-bundles model', *Journal of Applied Mechanics* **62**(2), 320–328.

Scott, D. W. (1992), *Multivariate Density Estimation: Theory, Practice, and Visualization*, Wiley Series in Probability and Mathematical Statistics, John Wiley & Sons.

Sherry, A. H., D. W. Beardsmore, D. P. G. Lidbury, M. A. Sheikh and I. C. Howard (1998), Remanent life assessment using the local approach – a prediction of the outcome of the NESC experiment, *in* 'Remanent Life Prediction – IMechE Seminar, London, 26 November 1997', Mechanical Engineering Publishing, Bury St Edmunds, UK, pp. 87–103.

Shterenlikht, A., S. H. Hashemi, J. R. Yates, I. C. Howard and R. M. Andrews (2003), 'Assessment of an instrumented charpy impact machine', Submitted to the International Journal of Fracture, August.

Smith, E. (1966*a*), 'The formation of a cleavage crack in a crystalline solid – I', *Acta Metallurgica* **14**, 985–989.

Smith, E. (1966*b*), 'The formation of a cleavage crack in a crystalline solid – II', *Acta Metallurgica* **14**, 991–996.

Smith, G. D. (1965), *Numerical Solution of Partial Differential Equations*, Oxford Mathematical Handbooks, Oxford University Press.

Szczepiński, W. (1982), On the mechanisms of ductile fracture of metals, *in* G. C.Sih and H.Zorski, eds, 'Defects and fracture. *Proceedings of First Inter-*

national Symposium on Defects and Fracture, held at Tuczno, Poland, October 13-17, 1980', Martinus Nijhoff Publishers, The Hague, pp. 155–163.

Thomason, P. F. (1968), 'A theory for ductile fracture by internal necking of cavities', *Journal of the Institute of Metals* **96**, 360–365.

Thomason, P. F. (1981), 'Ductile fracture and the stability of incompressible plasticity in the presence of microvoids', *Acta Metallurgica* **29**(5), 763–777.

Thomason, P. F. (1982), 'An assessment of plastic-stability models of ductile fracture', *Acta Metallurgica* **30**(1), 279–284.

Thomason, P. F. (1985*a*), 'A three-dimentional model for ductile fracture by the growth and coalescence of microvoids', *Acta Metallurgica* **33**(6), 1087–1095.

Thomason, P. F. (1985*b*), 'Three-dimentional models for the plastic limit-loads at incipient failure of the intervoid matrix in ductile porous solids', *Acta Metallurgica* **33**(6), 1079–1085.

Thomason, P. F. (1990), *Ductile Fracture of Metals*, Pergamon Press.

Thomason, P. F. (1993), 'Ductile fracture by the growth and coalescence of microvoids of non-uniform size and spacing', *Acta Metallurgica et Materialia* **41**(7), 2127–2134.

Thomason, P. F. (1998), 'A view on ductile-fracture modelling', *Fatigue and Fracture of Engineering Materials and Structures* **21**(9), 1105–1122.

Thompson, A. W. and J. F. Knott (1993), 'Micromechanics of brittle fracture', *Metallurgical Transactions A* **24**(3), 523–534.

Tipper, C. F. (1949), 'The fracture of metals', *Metallurgia* **39**, 133–137.

Tvergaard, V. (1981), 'Influence of voids on shear band instabilities under plain strain conditions', *International Journal of Fracture* **17**(4), 389–407.

Tvergaard, V. (1982*a*), 'Ductile fracture by cavity nucleation between larger voids', *Journal of the Mechanics and Physics of Solids* **30**(4), 265–286.

Tvergaard, V. (1982*b*), 'On localization in ductile materials containing spherical voids', *International Journal of Fracture* **18**(4), 237–252.

Tvergaard, V. (1990), 'Material failure by void growth to coalescence', *Advances in Applied Mechanics* **27**, 83–151.

Tvergaard, V. and A. Needleman (1984), 'Analysis of the cup-cone fracture in a round tensile bar', *Acta Metallurgica* **32**(1), 157–169.

Vandyoussefi, M. and A. L. Greer (2002), 'Application of cellular automaton-finite element model to the grain refinement of directionally solidified Al-4.15 wt% Mg alloys', *Acta Materialia* **50**(7), 1693–1705.

Von Neumann, J. (1966), *Theory of Self-Reproducing Automata*, Edited and completed by A. W. Burks, University of Illinois Press, Urbana, Illinois, USA.

Wallin, K. (1991), Statistical modelling of fracture in the ductile-to-brittle transition region, *in* J. G.Blauel and K. H.Schwalbe, eds, 'Defect Assessment in Components – Fundamentals and Applications, ESIS/EGF9', Mechanical Engineering Publications, London, pp. 415–445.

Weibull, W. (1951), 'A statistical distribution function of wide applicability', *Journal of Applied Mechanics* **18**, 293–297.

Wu, S. J. and C. L. Davis (2003), 'Effect of duplex ferrite grain size distribution on local fracture stresses of Nb-microalloyed steels', Presented at 13th International Conference on Strength of Materials, Hungary, 25 – 30th August. To be published in Journal of Materials Science and Engineering A.

Xia, L. and F. S. Shih (1996), 'Ductile crack growth – III. transition to cleavage fracture incorporating statistics', *Journal of the Mechanics and Physics of Solids* **44**(4), 603–639.

Xia, L. and L. Cheng (1997), 'Transition from ductile tering to cleavage fracture: A cell-model approach', *International Journal of Fracture* **87**(3), 289–306.

Yamamoto, H. (1978), 'Conditions for shear localization in the ductile fracture of void-containing materials', *International Journal of Fracture* **14**(4), 347–365.

Zhang, Z. L., C. Thaulow and J. Ødegård (2000), 'A complete Gurson model approach for ductile fracture', *Engineering Fracture Mechanics* **67**(2), 155–168.

Ziegler, H. (1977), *An Introduction to Thermomechanics*, Vol. 21 of *North-Holland series in Applied Mathematics and Mechanics*, North-Holland.

Zikry, M. A. and M. Kao (1996), 'Inelastic microstructural failure mechanisms in crystalline materials with high angle grain boundaries', *Journal of the Mechanics and Physics of Solids* **44**(11), 1765–1798.